COMPUTATIONAL MODELING OF DISLOCATION MICROSTRUCTURE PATTERNS AT SMALL STRAINS USING CONTINUUM DISLOCATION DYNAMICS

by

Vignesh Vivekanandan

A Dissertation

Submitted to the Faculty of Purdue University

In Partial Fulfillment of the Requirements for the degree of

Doctor of Philosophy

School of Materials Engineering

West Lafayette, Indiana

August 2023

THE PURDUE UNIVERSITY GRADUATE SCHOOL
STATEMENT OF COMMITTEE APPROVAL

Dr. Anter El-Azab, Chair
School of Materials Engineering

Dr. Xinghang Zhang
School of Materials Engineering

Dr. David Johnson
School of Materials Engineering

Dr. Janelle Wharry
School of Materials Engineering

Approved by:
Dr. Nikhilesh Chawla

Dedicated to my parents and friends

ACKNOWLEDGMENTS

I am deeply grateful to my advisor, Dr. Anter El-Azab, for providing me with the invaluable opportunity to pursue research in the field of dislocation dynamics. His unwavering pursuit of excellence and motivation to find optimal solutions played a pivotal role in the successful completion of my doctoral studies.

I would like to extend a special thank you to Dr. Peng Lin for generously making his continuum dislocation dynamics code available for my research. This invaluable resource significantly eased the challenges I faced and contributed immensely to the progress of my work.

I would also like to mention my sincere gratitude to the US Department of Energy and Naval Nuclear Laboratory for their generous funding and support throughout my research journey. Their financial assistance has been instrumental in the successful completion of my thesis.

I would like to express my heartfelt appreciation to all my colleagues at the Materials Theory group for their invaluable support and assistance throughout my doctoral studies. Their camaraderie and willingness to lend a helping hand have been instrumental in helping me navigate the trials and tribulations that I encountered along the way.

I would also like to express my sincere appreciation to my collaborators, Dr. Gustavo Castelluccio, Dr. David Mcdowell, Dr. Benjamin Anglin, and other members of the PRiSM program, for their invaluable feedback and insights provided during our biweekly meetings. Their encouragement and constructive comments made the journey of solving complex problems slightly more manageable. Additionally, I would like to acknowledge Dr. Grethe Winther and Dr. Bryan Miller for their valuable insights from an experimental perspective of the CDD results.

I am indebted to my committee members, Dr. Xinghang Zhang, Dr. David Johnson, and Dr. Janelle Wharry, for their diligent review of my progress throughout each year of my doctoral studies. Their guidance and oversight helped me stay focused and achieve my goals in a timely manner.

Lastly, I would like to express my deepest gratitude to my parents and sister for their unwavering support and belief in my abilities to succeed in my endeavors. Their constant encouragement has been a source of strength throughout my journey. I would also like to extend my appreciation to all my friends at Purdue University for creating a welcoming and supportive environment, allowing me to concentrate on my work without any distractions.

This thesis would not have been possible without the contributions and support of all those mentioned above, and I am truly grateful for their assistance on this meaningful endeavor.

TABLE OF CONTENTS

LIST OF TABLES

LIST OF FIGURES

ABSTRACT

Self-organized dislocation structures in deforming metals have a strong influence on the mechanical response of metals. However, accurate prediction of these patterns remains a challenge due to the complex dynamic and multiscale nature of the underlying process. This dissertation focuses on the development of a theoretical framework for continuum dislocation dynamics (CDD) models to predict dislocation microstructure formation at small strains, along with corresponding numerical simulation results. CDD models have the capability to incorporate plasticity physics spanning different time and length scales while capturing the dislocation motion explicitly within reasonable computational time. A typical model consists of two components: crystal mechanics, formulated as an eigenstrain problem, and dislocation dynamics, treated as a transport-reaction problem. In the first part of the thesis, a novel framework is introduced to solve the dislocation transport by decoupling the system of transport-reaction equations and enforcing the dislocation continuity constraint on individual slip systems. The results obtained from this framework demonstrate high accuracy and computational efficiency, significantly enhancing the predictive capabilities of the model. Building upon the framework, a statistical analysis of stress fluctuations in discrete dislocation dynamics (DDD) simulations is conducted to understand the relationship between coarse-grained average stress and local stress states. This analysis is motivated by the need to accurately capture dislocation reactions, such as cross-slip, which strongly depend on the local stress state, using the coarse-grained approach in CDD. The results revealed that the difference between the local and the coarse-grained states can be characterized using a Cauchy distribution. Consequently, a novel strategy is proposed to incorporate these statistical characteristics into the CDD model, yielding cross-slip rate predictions that align well with DDD results. In the final part of the study, the developed framework is applied to investigate the dislocation pattern formation during the early stages of cyclic loading. The simulation results successfully capture the formation of dislocation vein like structure and provide insights regarding the formation of labyrinth structure observed in experiments during cyclic loading at saturated state.

1. INTRODUCTION

Ever since experimentalists began to study the strength of metals, it became abundantly clear to them that there exists some defect that contributes to the difference between the theoretical and observed yield strength of the material. Three researchers (Orowan, 1934; Polanyi, 1934; Taylor, 1934) theorized the presence of defects around the same time named as dislocations, which were line defects that cause plastic distortion in metals. These dislocations interact in a complex manner when subjected to loading resulting in a non-uniform plastic deformation in the material. The collective behavior of dislocations especially in FCC materials which has little lattice resistance, exhibits formation of dislocation rich and dislocation poor zones in a well-defined manner and form distinct patterns like cells, walls, ladder and PSBs (Jin, 1989; Li et al., 2011; Mughrabi, 1983; Ungar et al., 1984). The formation of these patterns results in modified local behavior that significantly affects the mechanical response of the material. For instance, the formation of ladders and PSBs structures were found to be responsible for fatigue crack initiation (Basinski and Basinski, 1989) and cell structures were found to play a major role in the process of recrystallisation (Humphreys and Hatherly, 2012). Therefore, it becomes vitally important to understand the nature of these patterns and the condition under which they form to establish a relationship between microstructure and property of the material.

For almost half a century, attempts have been made to explain the formation of dislocation patterns using different frameworks ranging from energy minimization approaches to far from equilibrium nonlinear dynamics approaches (Aifantis, 1986; Kuhlmann-Wilsdorf, 2002). Kuhlmann-Wilsdorf (Hansen and Kuhlmann-Wilsdorf, 1986) proposed a framework termed as low-energy dislocation structure (LEDS) approach which focused on identifying stable dislocation configurations using energy minimization approach. The LEDS approach hypothesizes that the plastic deformation process is close to equilibrium and the dislocation patterns observed in experiments are stable configurations with the lowest possible total energy. It considers the energy associated with dislocation core structures, strain fields, and dislocation interactions, while performing energy minimization and seeks to find the configurations that represent the most favorable arrangements of dislocations. Based on this approach, the authors showed that the dislocation cell structure observed in experiments is the configuration with least possible energy for a given dislocation content (Kuhlmann-Wilsdorf and Comins, 1983). On the other hand,

Walgreaf and Aifantis proposed a reaction-diffusion model (Walgraef and Aifantis, 1985) represented by a set of partial differential equations that describe the evolution of dislocation densities and their spatial redistribution. It considered dislocations to be the reacting species and its evolution were captured using the reaction terms which modelled processes like dislocation annihilation and diffusion terms that captured the movement of dislocations throughout the crystal. The inspiration for this model originated from the success of capturing patterns observed during self-organization using the reaction-diffusion equation in biology, chemistry and other domains (Miura and Maini, 2004). This class of model was successful in capturing a labyrinth type structure (Pontes et al., 2006) from random initial condition comprising of dislocation patches or walls perpendicular to the slip direction.

Phenomenological models like those mentioned above have been instrumental in explaining certain dislocation patterns observed in experiments. However, these models lack the capability to fully capture the dynamic evolution of patterns and often rely on empirical expressions and parameter selection based on experimental evidence, limiting their predictive capabilities. To address these shortcomings, the field of discrete dislocation dynamics (A. Arsenlis et al., 2007; Devincre et al., 2001; Hussein et al., 2015; Kubin et al., 1992; Po et al., 2014; Stricker et al., 2018; Weygand et al., 2002) (DDD) emerged, explicitly capturing the motion of dislocations. Initially, one-dimensional dislocation pileups were studied using infinitely straight parallel edge dislocations (Amodeo and Ghoniem, 1988). Planar discrete dislocation models (Giessen and Needleman, 1995) were then developed to explore dislocation cell-like structures (Argaman et al., 2001), plastic zones ahead of dislocation-crack tips (Zacharopoulos et al., 2003), and dislocation jamming (Laurson et al., 2010). However, due to the three-dimensional nature of many dislocation microstructures, these models were insufficient to explore other experimentally observed features. To address this limitation, Kubin and co-workers (Devincre et al., 2011, 2001; Kubin et al., 1992) pioneered the development of the first 3D DDD simulation tool. In 3D DDD simulations, dislocations are represented as discrete line objects that move based on the Peach-Koehler force, resulting from interactions between dislocations, external loads, and other defects. Dislocation positions are updated using equations of motion, and topological rearrangements are performed to capture dislocation reaction processes such as cross-slip and annihilation (Bulatov and Cai, 2006; Kubin, 2013). Various DDD codes were subsequently developed with different discretization schemes, degrees of freedom, boundary conditions, time integration schemes, and long-range force

calculations. These models have provided valuable insights into the substructure development during cyclic loading (Déprés et al., 2006, 2005, 2004) and the formation of slip bands under high strain rate loading (Wang et al., 2007). However, they have struggled to fully capture the complexity of dislocation patterns observed in experiments. Additionally, the increase in computation time associated with a higher number of dislocation segments and stress calculations has limited the ability of DDD simulations to explore high-strain regimes effectively. Hence, an alternative model to DDD is required to adequately capture the dislocation patterns observed in experiments.

Due to the computational limitations of DDD, many researchers turned to density-based approaches to explicitly capture dislocation motion and model dislocation patterns. Building upon the classical works of Kroner (Kröner, 1959) and Nye (Nye, 1953), numerous continuum dislocation models have been developed, falling into three main categories: FDM models (Acharya, 2004; Acharya and Roy, 2006; Arora and Acharya, 2020), vector density-based CDD models (Lin and El-Azab, 2020; Vivekanandan et al., 2021; Xia and El-Azab, 2015) and hDCDD models (Hochrainer, 2015; Hochrainer et al., 2007; Monavari and Zaiser, 2018; Sandfeld et al., 2010). While variants of the FDM theory, demonstrated by Acharya, have shown the formation of dipolar dislocation walls and cell-like structures (Arora and Acharya, 2020), they lack the ability to represent slip system details necessary for accurately capturing the dependence of dislocation behavior on loading orientations and the influence of dislocation reactions on patterning. On the other hand, Sandfeld's exploration using the 2D version of hdCDD (Sandfeld and Zaiser, 2015) proposed by Hochrainer (Hochrainer et al., 2007) successfully demonstrated the formation of cell-like structures and considered slip system-level details. However, this approach relies on several approximations to model kinematic closure relations to make it computationally tractable.

Therefore, the focus of this thesis is to develop theoretical frameworks using the vector density based CDD model, aiming to predict dislocation patterns more effectively. The structure of the thesis is as follows: Section 2 introduces the theoretical background of vector based CDD models. In Section 3, a novel theoretical framework is proposed, which decouples the dislocation transport-reaction equations and enforces the dislocation continuity constraint on each slip system individually. Section 4 explores the significance of stress fluctuation statistics, defined as the difference between the coarse-grained stress used to drive dislocation dynamics in CDD and the local stress on the dislocation, by analyzing dislocation configurations from DDD simulations.

This analysis specifically focuses on dislocation processes such as cross-slip, where the local stress state plays a crucial role. Section 5 presents a new cross-slip framework for CDD, utilizing statistics from DDD, and investigates the impact of different cross-slip activation energy formulations on mechanical response and dislocation microstructure evolution. In Section 6, the capability of the CDD model to predict dislocation patterns observed during cyclic loading at small strains is highlighted. Finally, section 7 provides a comprehensive summary of the work conducted and the insights gained from CDD simulations.

2. CONTINUUM DISLOCATION DYNAMICS : BACKGROUND

In this section, a brief introduction on the technical background of continuum dislocation dynamics theory is provided. The origins of the continuum theory of dislocations can be traced back to the pioneering work by (Mura, 1963) who first introduced the concept of continuous representation of dislocation using a density tensor that contains the coarse-grained information regarding slip systems and Burgers vectors. The density tensor is usually referred to as the dislocation density tensor which can be interpreted as the physical quantity that contains the cumulative information regarding the average line dislocation density $\boldsymbol{\rho}$ and Burgers vector $\boldsymbol{b}$ of all slip systems as given below,

$$\boldsymbol{\alpha} = \sum_{i} \boldsymbol{\rho}^{i} \otimes \boldsymbol{b}^{i}. \tag{2.1}$$

The primary goal of the continuum theory of dislocations was to establish a relation between this coarse-grained density representation and deformed state. The deformed state is defined in terms of the total distortion tensor $\boldsymbol{\beta}$, which is defined as the gradient of displacement field, which typically comprises of two components- elastic distortion tensor $\boldsymbol{\beta}^{\mathrm{e}}$ and plastic distortion tensor $\boldsymbol{\beta}^{\mathrm{p}}$ as described in the equation below.

$$\boldsymbol{\beta} = \nabla \boldsymbol{u} = \boldsymbol{\beta}^{\mathrm{e}} + \boldsymbol{\beta}^{\mathrm{p}}. \tag{2.2}$$

The elastic distortion tensor accounts for the distortion due to elastic fields that induces strain and rotation in the crystal whereas the plastic distortion tensor accounts for the distortion due to the plastic slip of dislocations which distorts the shape of the crystal. The two distortion tensor fields represent very different physical quantities and are incompatible in nature. On the account of being related to the elastic strain fields, the elastic distortion tensor is related to the internal stress in the material in terms of the Hooke's law as described below,

$$\boldsymbol{\sigma} = \boldsymbol{C} : \boldsymbol{\beta}^{\mathrm{e}}, \tag{2.3}$$

where $\boldsymbol{C}$ is the fourth rank elasticity tensor and $\boldsymbol{\sigma}$ is the internal stress. Since the total distortion tensor is a compatible field, by using the curl free property of it, we get the relationship between the elastic and plastic distortion tensor which can be expressed as

$$\boldsymbol{\nabla} \times \boldsymbol{\beta}^{\mathrm{e}} = -\boldsymbol{\nabla} \times \boldsymbol{\beta}^{\mathrm{p}}. \tag{2.4}$$

Equation (2.4) shows that the measures of incompatibility of the above two quantities are equal and opposite. Mura (Mura, 1963) and Kosevich (Kosevich, 1965) defines this measure as dislocation density tensor $\boldsymbol{\alpha}$,

$$\boldsymbol{\alpha} = \boldsymbol{\nabla} \times \boldsymbol{\beta}^{\mathrm{e}} = -\boldsymbol{\nabla} \times \boldsymbol{\beta}^{\mathrm{p}}. \tag{2.5}$$

The dynamic evolution of the plastic distortion during deformation can then be captured by taking a time derivative of equation (2.5), which gives us,

$$\dot{\boldsymbol{\alpha}} + \boldsymbol{\nabla} \times \dot{\boldsymbol{\beta}}^{\mathrm{p}} = \dot{\boldsymbol{\alpha}} + \boldsymbol{\nabla} \times \boldsymbol{J} = \boldsymbol{0}, \tag{2.6}$$

where $\boldsymbol{J} = \dot{\boldsymbol{\beta}}^{\mathrm{p}}$, commonly referred to as the dislocation flux tensor. The set of equations defined above can be solved to estimate the displacement, elastic strain field and stress field provided the plastic distortion $\boldsymbol{\beta}^{\mathrm{p}}$ and dislocation flux tensor $\boldsymbol{J}$ are known. However, for the above system of equations to capture the evolution of dislocation configuration, an additional closure relation must be provided as the information contained in the dislocation density tensor is not sufficient to determine the dislocation flux tensor. The reason behind this is that the dislocation density tensor according to the classical theory only captures the geometrically necessary dislocations (GND) but the evolution of plastic distortion tensor in general depends on both GND and statistically stored dislocations (SSD) (El-Azab and Po, 2020).

Different approaches have been undertaken to achieve this closure depending upon the length scale in which the model operates (Acharya, 2004; Groma, 1997; Hochrainer et al., 2007; Kalaei et al., 2022; Xia and El-Azab, 2015). In this thesis, the vector density based approach (Lin and El-Azab, 2020; Vivekanandan et al., 2021; Xia and El-Azab, 2015) has been adopted to model the dislocation density evolution. The model represents dislocation content in terms of dislocation density vectors belonging to each individual slip system. It makes use of the line bundle approximation which allows dislocations belonging to every slip system to have a single line orientation at every point in the domain. This assumption is possible as the model operates on a fine enough length scale that is comparable to the dislocation annihilation distance. Consequently, the dislocation density tensor can be considered to contain only GNDs with line bundles of same orientation in each slip system. Based on the above arguments, the dislocation density in a slip system i can be represented as $\boldsymbol{\rho}^i = \rho^i \boldsymbol{\xi}^i$ where $\boldsymbol{\xi}$ is the unit line tangent of the dislocation bundle and ρ is the scalar dislocation density. It is worth mentioning that without the line bundle

approximation the statement in the previous sentence would not hold true. The evolution of dislocation density belonging to slip system can then be written as

$$\dot{\boldsymbol{\rho}}^i = \nabla \times \left(\boldsymbol{v}^i \times \boldsymbol{\rho}^i\right) + \dot{\boldsymbol{\rho}}^i_{\text{rxn}} \tag{2.7}$$

where the first term corresponds to the rate of change of dislocation density due to bow-out and the second term corresponds to the rate of change of dislocation density due to dislocation reaction processes like cross-slip and junction formation. The $\boldsymbol{v}^i$ in Eq. (2.7) corresponds to the velocity of the dislocation belonging to slip system i, which can be computed in terms of glide component of Peach-Koehler force based on a linear mobility law (Lin and El-Azab, 2020) as follows

$$\boldsymbol{v}^i = M|\boldsymbol{b}|\tau^i \boldsymbol{\xi}^i \times \boldsymbol{n}^i. \tag{2.8}$$

where τ^i is the resolved shear stress on slip system i and $\boldsymbol{n}^i$ is the slip plane normal of slip system i. Solving the dislocation dynamics equation, updates the dislocation configuration based on which the plastic distortion can then be updated using the Field dislocation Mechanics (FDM) approach (Lin et al., 2021; Roy and Acharya, 2006). The FDM approach splits the plastic distortion tensor into compatible ($\boldsymbol{\nabla z}$) and incompatible ($\boldsymbol{\chi}$) parts which can be written as

$$\boldsymbol{\beta}^{\text{p}} = \boldsymbol{\nabla z} - \boldsymbol{\chi} \tag{2.9}$$

These two parts can then be updated separately based on the following system of equations.

$$\begin{aligned} &\nabla \times \boldsymbol{\chi} = \textstyle\sum_k \boldsymbol{\rho}^k \otimes \boldsymbol{b}^k \text{ in } \Omega \\ &\nabla \cdot \boldsymbol{\chi} = \boldsymbol{0} \qquad \text{in } \Omega \\ &\boldsymbol{n} \cdot \boldsymbol{\chi} = \boldsymbol{0} \qquad \text{on } \partial\Omega \end{aligned} \tag{2.10}$$

and

$$\begin{aligned} &\nabla \cdot \nabla \dot{\boldsymbol{z}} = \nabla \cdot \textstyle\sum_k (-\boldsymbol{v}^k \times \boldsymbol{\rho}^k \otimes \boldsymbol{b}^k) \qquad \text{in } \Omega \\ &\boldsymbol{n} \cdot \nabla \dot{\boldsymbol{z}} = \boldsymbol{n} \cdot \textstyle\sum_k (-\boldsymbol{v}^k \times \boldsymbol{\rho}^k \otimes \boldsymbol{b}^k) \qquad \text{in } \Omega \end{aligned} \tag{2.11}$$

Together, these sets of equations provide the closure to the vector based CDD model, which now has sufficient information to model the dislocation density evolution based on the dislocation density tensor and plastic distortion tensor which can be used to estimate the stress field.

3. VIRTUAL DISLOCATION DENSITY FRAMEWORK

A portion of this chapter has been published in the Journal of Mechanics and Physics of Solids by Vignesh Vivekanandan, Peng Lin, Grethe Winter and Anter El-Azab as “On the implementation of dislocation reactions in continuum dislocation dynamics modeling of mesoscale plasticity”, 149, 104327. https://doi.org/10.1016/j.jmps.2021.104327.

3.1 Abstract

The continuum dislocation dynamics framework for mesoscale plasticity is intended to capture the dislocation density evolution and the deformation of crystals when subjected to mechanical loading. It does so by solving a set of transport equations for dislocations concurrently with crystal mechanics equations, with the latter being cast in the form of an eigenstrain problem. Incorporating dislocation reactions in the dislocation transport equations is essential for making such continuum dislocation dynamics predictive. A formulation is proposed to incorporate dislocation reactions in the transport equations of the vector density-based continuum dislocation dynamics. This formulation aims to rigorously enforce dislocation line continuity using the concept of virtual dislocations that close all dislocation loops involved in cross slip, annihilation, and glissile and sessile junction reactions. The addition of virtual dislocations enables us to accurately enforce the divergence free condition upon the numerical solution of the dislocation transport equations for all slip systems individually. A set of tests were performed to illustrate the accuracy of the formulation and the solution of the transport equations within the vector density-based continuum dislocation dynamics. Comparing the results from these tests with an earlier approach in which the divergence free constraint was enforced on the total dislocation density tensor or the sum of two densities when only cross slip is considered shows that the new approach yields highly accurate results. Bulk simulations were performed for a face centered cubic crystal based on the new formulation and the results were compared with discrete dislocation dynamics predictions of the same. The microstructural features obtained from continuum dislocation dynamics were also analyzed with reference to relevant experimental observations.

3.2 Introduction

It is currently well established that the phenomenological continuum plasticity theories are insufficient to capture the plastic behavior of crystals at the scale of the dislocation microstructure. This motivated the metal deformation community to develop plasticity models based upon the dislocation mechanics. The method of discrete dislocation dynamics (DDD) simulation was developed as a part of that effort, and, despite its computational limitations, the method has enabled many successful mesoscale plasticity investigations (Arsenlis et al., 2007; Groh and Zbib, 2009; Kubin et al., 1992; Po et al., 2014; Rhee et al., 1998; Weygand et al., 2002). Relevant to this current work is the use of DDD models in understanding the role of junctions in plastic deformation. Indeed, the success of these models inspired the study of the role of dislocation junctions in stage II strain hardening behavior (Franciosi et al., 1980; Kocks, 1966; Taylor, 1934). Dislocation junctions in face centered cubic (FCC) crystals are categorized into four categories: Hirth junctions, Lomer junctions, glissile junctions and collinear junctions. The role of such junctions in the strain hardening behavior of crystals was recently studied by many discrete dislocation dynamics simulations (Devincre et al., 2008; Devincre, 2013; Stricker and Weygand, 2015; Sills et al., 2018; Stricker et al., 2018; Mishra and Alankar, 2019)). It was found that glissile junctions have the highest contribution towards hardening (Sills et al., 2018). Apart from its contribution to hardening, glissile junctions were also found to be responsible for the dislocation multiplication mechanism (Stricker et al., 2018) in FCC metals, which play a significant role in influencing microstructure evolution. DDD simulations were also used to study cross slip, which is a thermally activated process that results in the change of the glide plane of the screw-orientated dislocations. Similar to glissile junctions, cross slip also contributes towards the dislocation multiplication mechanism playing a crucial role in the microstructure evolution (Hussein et al., 2015; Stricker et al., 2018). Although DDD simulations have demonstrated sufficient capability to study dislocation behavior under deformation, they suffer from scalability issues making them unsuitable for large-scale bulk simulations, and this is where continuum dislocation dynamics (CDD) is thought to fill an important gap.

Early attempts to relate plastic deformation and dislocations at a continuum level resulted in the now-called classical continuum theory of dislocations (Kröner, 1959; Nye, 1953). In these classical works, the incompatibility of the elastic and plastic distortion field was cast in the form of a continuous field called the dislocation density tensor. However, the lack of sufficient

information to determine the dislocation motion from the dislocation density tensor hindered further development of this theory toward being a plasticity framework (Kosevich, 1965; Mura, 1963). Inspired by Mura and Kosevich, Acharya and co-workers (Acharya and Roy, 2006; Roy and Acharya, 2006) developed a model called field dislocation mechanics, in which transport laws for the evolution of the dislocation density tensor along with a closure law for the speed of dislocation transport in terms of the local stress were used to build a plasticity framework based on a tensor representation of the dislocation field. Several other groups, however, used statistical approaches to reach continuum, density-based descriptions of dislocation dynamics in two-dimensions (2D) (Groma, 1997; Groma et al., 2003; Kooiman et al., 2014; Zaiser et al., 2001). These 2D models were later used to capture the evolution of the dislocation density in a crystal plasticity type setting by (Yefimov et al., 2004a, 2004b). Extension of the statistical approach to three dimensions (3D) was then accomplished by El-Azab and co-workers (El-Azab, 2000a, 2006; Deng and El-Azab, 2009), where the curved interconnected dislocation configurations were represented in a phase space following the classical statistical mechanics concepts. Other different approaches were pursued to capture the 3D dislocation microstructure. For example, Hochrainer and co-workers developed a class of models (Hochrainer et al., 2007; Sandfeld et al., 2010) that represent dislocations using a tensor in a higher dimensional phase space which carries the additional information about the local line orientation and curvature of the curved lines. A simplified version of the higher-order theory suitable for numerical implementation was developed later (Hochrainer, 2015; Hochrainer et al., 2014; Sandfeld et al., 2011; Sandfeld and Zaiser, 2015) based on the concept of dislocation alignment tensors (Hochrainer, 2015).

The first report of modeling of cross slip and dislocation reactions in CDD was due to El-Azab (El-Azab, 2000), where slip system-level consideration of dislocations along with their line directions enabled the introduction of rate terms representing such processes into the dislocation transport equations; see also (Deng and El-Azab, 2009). In (Deng and El-Azab, 2010), time series analysis was introduced to estimate the cross slip and junction reaction rates from DDD data. More recently, Monavari and Zaiser (Monavari and Zaiser, 2018) proposed a model that incorporates dislocation reactions like cross slip and glissile junctions as sources of dislocation multiplication. Their model associated dislocation reactions with a new field variable called curvature density, which described the volume density of dislocation loops in the system. Recently, Sudmanns and co-workers (Sudmanns et al., 2019) also developed a model along similar lines in which they

represented dislocation reactions based on the lessons learned from DDD simulations (Stricker et al., 2018). The dislocation density evolution on the active and inactive slip systems due to glissile junction reaction was captured successfully similar to the results obtained from DDD simulations. In this paper, a new formulation to incorporate dislocation cross slip and reactions in CDD is proposed and implemented within the framework previously developed in (Xia and El-Azab, 2015; Lin and El-Azab, 2020; and Starkey et al., 2020). In this framework, dislocations are represented by vector density fields on individual slip systems as a line bundle such that dislocations on each slip system have a single line direction at each point in space. The evolution of the dislocation density field is governed by a curl type dislocation transport equation with dislocation reaction terms. The current formulation aims to represent the change in the slip system density due to dislocation cross slip and reactions using a closure density called here the virtual dislocation density. Dislocation processes like cross slip and glissile junctions are modeled as dislocation source terms in the transport equations, to capture the dislocation multiplication mechanism. In addition to that, a new method of enforcing the divergence constraint on the dislocation density is introduced that takes virtual density into consideration, thus enabling the implementation of this important constraint to individual slip system densities. This significantly facilitates the computational solution of the dislocation transport system of equations in 3D and enables us to track the dislocation network effectively. The paper is organized as follows. Section 3.3 outlines the CDD formalism of mesoscale plasticity used here. Section 3.4 introduces the concept of virtual density and how it is integrated into the dislocation kinetics. Section 3.5 describes the numerical implementation of the dislocation kinetics equations. Section 3.6 discusses the simulation results obtained based on this formulation, followed by a short discussion and conclusions.

3.3 Continuum dislocation dynamics model

Continuum dislocation dynamics formulation of mesoscale plasticity comprises of two parts, namely the stress-equilibrium problem and dislocation kinetics problem. In this section, the method used to solve the stress equilibrium problem is outlined and the dislocation kinetics problem is discussed in detail.

3.3.1 Stress-equilibrium problem

For the case of small deformation, the distortion tensor, $\boldsymbol{\beta}$, can be expressed as the gradient of displacement, $\boldsymbol{\nabla u}$, which can be decomposed into two incompatible fields, the elastic distortion tensor, $\boldsymbol{\beta}^e$, and plastic distortion tensor, $\boldsymbol{\beta}^p$. These two tensors describe the deformation of the lattice and the shape change of the crystal, respectively. The displacement field due to the applied load and dislocations present in the crystal is obtained by solving the eigen distortion problem stated below:

$$\nabla \cdot \boldsymbol{\sigma} \;=\; \boldsymbol{\nabla} \cdot (\boldsymbol{C}\colon \boldsymbol{\beta}^{\mathrm{e}}) = \boldsymbol{\nabla} \cdot \left(\boldsymbol{C}\colon (\boldsymbol{\nabla u} - \boldsymbol{\beta}^{\mathrm{p}})\right) \;=\; \mathbf{0} \text{ in } \Omega \tag{3.1}$$

$$\boldsymbol{u} = \bar{\boldsymbol{u}} \text{ on } \partial\Omega_u$$

$$\boldsymbol{n} \cdot \boldsymbol{\sigma} \;=\; \bar{\boldsymbol{t}} \text{ on } \partial\Omega_t.$$

In the above, $\boldsymbol{\sigma}$ is Cauchy stress tensor, $\boldsymbol{C}$ the elastic tensor, Ω the domain of solution, $\partial\Omega_u$ and $\partial\Omega_t$, respectively, are the parts of the boundary on which the displacement $\boldsymbol{u} = \bar{\boldsymbol{u}}$ and the traction $\bar{\boldsymbol{t}}$ are prescribed. By solving the above boundary value problem, the displacement and stress fields are updated, and the latter is then used to determine the Peach-Koehler force and the dislocation velocity based on a mobility law. Together with the dislocation density, the dislocation velocity is used to find the rate of plastic distortion via Orowan's law. The latter is then used to update the plastic distortion using a direct time integration (Xia and El-Azab, 2015) or via the field dislocation mechanics scheme (Acharya and Roy, 2006; Roy and Acharya, 2005, Lin et al., 2020).

3.3.2 Dislocation kinetics

In continuum dislocation dynamics, dislocations are represented as continuous fields in terms of dislocation density tensor, $\boldsymbol{\alpha}$. In the current work, the tensor $\boldsymbol{\alpha}$ is defined following the formulation proposed by (Kröner, 1959) where it is quantified in terms of plastic distortion tensor $\boldsymbol{\beta}^{\mathrm{p}}$ as

$$\boldsymbol{\alpha} = -\nabla \times \boldsymbol{\beta}^{\mathrm{p}}, \tag{3.2}$$

The evolution of $\boldsymbol{\alpha}$ is obtained by differentiating eq. (3.2) with time, which yields us

$$\dot{\boldsymbol{\alpha}} = -\nabla \times \dot{\boldsymbol{\beta}}^{\mathrm{p}}. \tag{3.3}$$

In the case of single slip, and assuming that the dislocation field is characterized by a single line direction and hence a unique velocity field at every point in space, the rate of plastic distortion is obtained from Orowan's law:

$$\dot{\boldsymbol{\beta}}^{\mathrm{p}} = -\boldsymbol{v} \times \boldsymbol{\alpha}, \tag{3.4}$$

with $\boldsymbol{v}$ being the dislocation velocity. Substituting this in equation (3.3), we get

$$\dot{\boldsymbol{\alpha}} = \nabla \times (\boldsymbol{v} \times \boldsymbol{\alpha}). \tag{3.5}$$

The unique line and velocity of the dislocation field at every point in space is known as the dislocation bundle idealization, and it assumes that the spatial resolution is fine enough so that dislocations of a given Burgers vector and slip plane have the same line direction at ever point in the crystal. This allows us to define the vector dislocation density $\boldsymbol{\rho}$ at every point as

$$\boldsymbol{\rho} = \rho \boldsymbol{\xi}, \tag{3.6}$$

where ρ is the scalar dislocation density and $\boldsymbol{\xi}$ is the unit tangent of the dislocations. The dislocation density tensor can then be expressed in terms of dislocation density vector and Burgers vector,

$$\boldsymbol{\alpha} = \boldsymbol{\rho} \otimes \boldsymbol{b}. \tag{3.7}$$

Substituting equation (3.7) in equation (3.5), we get

$$\dot{\boldsymbol{\rho}} \otimes \boldsymbol{b} = \nabla \times \big(\boldsymbol{v} \times (\boldsymbol{\rho} \otimes \boldsymbol{b})\big). \tag{3.8}$$

The above equation can then be simplified to

$$\dot{\boldsymbol{\rho}} = \nabla \times (\boldsymbol{v} \times \boldsymbol{\rho}). \tag{3.9}$$

The dislocation velocity $\boldsymbol{v}$ is estimated based on a mobility law that scales linearly with the local resolved shear stress on that slip system whose details are explained in Section 3.5.4. Equation (3.9) is referred to as the dislocation transport equation, and it accounts for the increase in line length of the dislocations due to curvature. The above equation is incomplete since dislocation transport is not the only mechanism through which dislocation density evolves. Many DDD simulations have pointed out that dislocation reactions such cross slip and junctions are responsible for re-distributing dislocations amongst different slip systems (Arsenlis et al., 2007; (Hussein et al., 2015); Kubin et al., 2008; Sills et al., 2018; Stricker et al., 2018; Stricker and Weygand, 2015).

Hence, to complete the kinetic equations, a general formulation to incorporate dislocation reactions is proposed in the next section.

3.3.3 Dislocation reactions

In this current work we refer to cross slip, junction formation and annihilation processes as dislocation reactions. Since, the dislocations are represented as vector densities, the annihilation reaction on the same slip system is considered implicitly. Hence, in this section a method to incorporate cross slip and junction reactions into dislocation density evolution equation is described.

Cross slip is a thermally activated process through which a screw dislocation changes its glide plane to the cross-slip plane that shares the same Burgers vector. Junction is a process through which two dislocation segments from two different slip systems react with each other and form a third (product) segment which lies along the intersection of two planes of the reacting segments and has Burgers vector equaling to the sum of the Burgers vectors of two reacting segments. They can be classified into four types of junctions namely glissile, Lomer, Hirth, and collinear. Cross slip and glissile junction acts as dislocation sources since they introduce new dislocations into a given slip system. Unlike cross-slip and glissile junction, the other junctions do not introduce new dislocations to other slip systems, but they can be unzipped and reintroduced into their parent slip systems.

In CDD models, dislocation reactions are characterized as rate processes that captures the fraction of dislocation density that is consumed from or added to a given slip system density. In FCC crystals, dislocations in a slip system can be involved in at most two cross slip reaction and 11 junction reactions. The rates of these processes are expressed as follows:

$$\dot{\boldsymbol{\rho}}_{\mathrm{cs},i\to j} = \dot{r}_{i\to j}\boldsymbol{\rho}_{\mathrm{g}}^{i} \tag{3.10}$$

$$\dot{\boldsymbol{\rho}}_{\mathrm{G},ijk} = \dot{r}_{\mathrm{G},ijk}\left(\boldsymbol{\rho}_{\mathrm{g}}^{i}\cdot\boldsymbol{e}_{ij}\right)\left(\boldsymbol{\rho}_{\mathrm{g}}^{j}\cdot\boldsymbol{e}_{ij}\right)\boldsymbol{e}_{ij} \tag{3.11}$$

$$\dot{\boldsymbol{\rho}}_{\mathrm{L},ij} = \dot{r}_{\mathrm{L},ij}\left(\boldsymbol{\rho}_{\mathrm{g}}^{i}\cdot\boldsymbol{e}_{ij}\right)\left(\boldsymbol{\rho}_{\mathrm{g}}^{j}\cdot\boldsymbol{e}_{ij}\right)\boldsymbol{e}_{ij} \tag{3.12}$$

$$\dot{\boldsymbol{\rho}}_{\mathrm{H},ij} = \dot{r}_{\mathrm{H},ij}\left(\boldsymbol{\rho}_{\mathrm{g}}^{i}\cdot\boldsymbol{e}_{ij}\right)\left(\boldsymbol{\rho}_{\mathrm{g}}^{j}\cdot\boldsymbol{e}_{ij}\right)\boldsymbol{e}_{ij}, \tag{3.13}$$

where $\dot{\boldsymbol{\rho}}_{\mathrm{cs},i\to j}$, $\dot{\boldsymbol{\rho}}_{\mathrm{G},ijk}$, $\dot{\boldsymbol{\rho}}_{\mathrm{L},ij}$, $\dot{\boldsymbol{\rho}}_{\mathrm{H},ij}$ represent the rate of change of dislocation density due to cross slip and glissile, Lomer and Hirth junctions, respectively (Lin and El-Azab, 2020; Xia et al., 2016),

$\dot{r}_{i\to j}$, $\dot{r}_{\mathrm{G},ijk}$, $\dot{r}_{\mathrm{L},ij}$ and $\dot{r}_{\mathrm{H},ij}$ are the corresponding rate coefficients, $\boldsymbol{\rho}_{\mathrm{g}}^{i}$ denotes the glide dislocation density of slip system i, and $\boldsymbol{e}_{ij}$ is the unit vector along the line of intersection of the two slip planes i and j involved in the reaction. In the case of cross slip, the subscript $i \to j$ indicates that the cross slip event happens from slip system i to slip system j. In the case of glissile junctions, the indices i, j and k refer to the dislocations on slip system i and j reacting to form glissile junction on slip system k. In the case of Lomer and Hirth locks, the indices i, j refer to the dislocations on slip system i and j reacting to form Lomer and Hirth junctions. The rates coefficients for the different reactions are expressed in the form:

$$\dot{r}_{i\to j} = \iota_{\mathrm{s}}\dot{p}_{i\to j} \tag{3.14}$$

$$\dot{r}_{\mathrm{G},ijk} = \iota_{e_{ij}}\dot{p}_{\mathrm{G},ijk} \tag{3.15}$$

$$\dot{r}_{\mathrm{L},ij} = \iota_{e_{ij}}\dot{p}_{\mathrm{L},ij} \tag{3.16}$$

$$\dot{r}_{\mathrm{H},ij} = \iota_{e_{ij}}\dot{p}_{\mathrm{H},ij}, \tag{3.17}$$

where $\dot{p}_{i\to j}$, $\dot{p}_{\mathrm{G},ijk}$, $\dot{p}_{\mathrm{L},ij}$and $\dot{p}_{\mathrm{H},ij}$ are the probability rates of cross slip and glissile, Lomer and Hirth junctions, respectively, all computed from discrete dislocation line models. In equation (3.14), ι_{s} is a dislocation line orientation indicator function that is non-zero only when the line orientation satisfies a screw direction criterion. In equations. (3.15-3.17), $\iota_{e_{ij}}$ is an orientation indicator function that is non-zero only when the line orientations of the reacting segments satisfy the junction orientation criteria. The probability rates of cross-slip and junction reactions are estimated based on the procedure outlined by (Deng and El-Azab, 2010; Xia et al.,2016) where the statistics of these rate processes are obtained from DDD simulations in the form of time series and subsequently coarse grained before mapping to CDD model.

Based on the equations (3.10) through (3.13), equation (3.9) is closed by incorporating the source terms into the dislocation density evolution as follows

$$\dot{\boldsymbol{\rho}}_{\mathrm{g}}^{i} = \nabla\times\left(\boldsymbol{v}^{i}\times\boldsymbol{\rho}_{\mathrm{g}}^{i}\right) - \dot{\boldsymbol{\rho}}_{\mathrm{cs},i\to j} - \sum_{j,k}\dot{\boldsymbol{\rho}}_{\mathrm{G},ijk} - \sum_{j}\dot{\boldsymbol{\rho}}_{\mathrm{L},ij} - \sum_{j}\dot{\boldsymbol{\rho}}_{\mathrm{H},ij} + \dot{\boldsymbol{\rho}}_{\mathrm{cs},j\to i} + \sum_{j,k}\dot{\boldsymbol{\rho}}_{\mathrm{G},jki}. \tag{3.18}$$

The four terms following the curl term to the right-hand side of equation (3.18) correspond to the rate at which dislocation density is removed from the slip system i due to one cross slip reaction, four glissile junction reactions, two Lomer lock reactions and two Hirth lock reaction,

respectively. The summation over j inside this parenthesis refers to the different slip systems with which slip system i reacts to form glissile junctions and Lomer and Hirth locks. The last two terms in the same equation correspond to the rate at which the dislocation density is added to the slip system i due to one cross slip reaction and two glissile junction reactions, respectively. Similarly, the summation over j and k in this case refers to different slip systems that react to form glissile junction product on slip system i. Note that the summation for the glissile junction terms is performed over unique pairs of j and k to prevent counting the same type of reaction twice.

It is to be noted that in the current formulation, the unzipping of Lomer and Hirth locks in the evolution of dislocation densities in equation (3.18) is not specified. Ideally, two additional terms corresponding to unzipping of these locks based on the local stress state should also be considered to complete glide dislocation density evolution equation. Although different measures have been undertaken in both discrete and continuum dislocation dynamics models (Arsenlis et al., 2007; Weygand et al., 2002; Sudmanns et al., 2020) to capture the unzipping process, defining a model suitable for this framework remains elusive. Currently, work is underway to calibrate the rate of unzipping for the current framework and will be a subject of future publication.

Finally, to ensure that dislocations do not end inside the crystal a divergence-free condition is enforced on the dislocation density tensor $\boldsymbol{\alpha}$, which can be written as

$$\nabla \cdot \boldsymbol{\alpha} = \mathbf{0}. \tag{3.19}$$

In the case of a single slip system and in the absence of reactions, this condition reads: $\nabla \cdot \boldsymbol{\rho} = 0$. In such cases, the dislocation density evolution is obtained by solving equation (3.9) subject to the divergence constraint (3.19).

Following the algorithm mentioned in (Lin et al., 2020), our preliminary results showed that the solution contained spurious dislocation densities when the dislocation reactions are involved. Subsequent analysis revealed that the coupling of the slip systems by dislocation reactions induced significant numerical errors because of the divergence constraint imposed on total dislocation density tensor. Hence, to resolve this problem, an alternative method of enforcing the divergence constraint is introduced here based upon the concept of virtual dislocations.

3.4 Virtual dislocations

The concept of virtual dislocations was introduced previously in DDD simulations by (Stricker et al., 2018) and MODEL code (Po and Ghoniem, 2015). Virtual dislocations are a non-physical entity with zero Burgers vector that bounds the glide area of dislocations involved in reactions such as cross slip, junction formation, or annihilation. Borrowing this idea from the discrete setup, virtual density in CDD is defined as the non-physical density that quantifies the amount of physical dislocation density in CDD that is involved in the dislocation reaction. Since this density is non-physical, its contribution to plastic deformation of crystals is zero. Its contribution to the long-range stress in the crystal is also ensured to be zero by virtue of the fact the associated virtual dislocation density tensor at every point is zero.

For every slip system two vector densities are defined: a glide density $\boldsymbol{\rho}_{\mathrm{g}}$ and a virtual density $\boldsymbol{\rho}_{\mathrm{v}}$. The glide density is the physical dislocation density that distorts the crystal elastically and contributes to the plastic distortion. Correspondingly, two dislocation density tensors are defined: a glide dislocation density tensor $(\boldsymbol{\alpha}_{\mathrm{g}})$ and a virtual dislocation density tensor $(\boldsymbol{\alpha}_{\mathrm{v}})$. The virtual dislocation density tensor $\boldsymbol{\alpha}_{\mathrm{v}}$ is defined as follows.

$$\boldsymbol{\alpha}_{\mathrm{v}} = \sum_{i} \boldsymbol{\rho}_{\mathrm{v}}^{i} \otimes \boldsymbol{b}^{i} \,. \tag{3.20}$$

The definition of the virtual dislocation density is explained by considering the two dislocation reactions of interest, namely, cross slip and glissile junctions. Fig. 3.1(a) illustrates cross slip. In this process, a loop that originally belonged to slip system 1 is now spread onto both slip system 1 and 2. This configuration can be viewed as two loops, the first contained in slip system 1 and the second in 2, such that part of the two loops overlap at the intersection of the two cross slip planes. These parts are denoted by the dotted lines and they represent the virtual dislocation densities. The red dotted line in slip system 1 is the virtual density, $\boldsymbol{\rho}^{1}_{\mathrm{v_{cs},1\to2}}$, for slip system 1, and it corresponds to the closure of the glide density on slip system 1 corresponding to the part that has already cross slipped. The green dotted line in slip system 2 is the virtual density for slip system 2, $\boldsymbol{\rho}^{2}_{\mathrm{v_{cs},1\to2}}$ that closes the loop on slip system 2. The cross-slipped dislocation density from slip system 1 after bowing out is represented as $\boldsymbol{\rho}^{2}_{\mathrm{g}}$. The rate of change of virtual densities of slip system 1 and 2 for a cross-slip reaction is given by equation below.

$$\dot{\boldsymbol{\rho}}^{1}_{\mathrm{v_{cs},1\to2}} = -\dot{\boldsymbol{\rho}}^{2}_{\mathrm{v_{cs},1\to2}} = \dot{r}_{i\to j}\boldsymbol{\rho}^{1}_{\mathrm{g}} \tag{3.21}$$

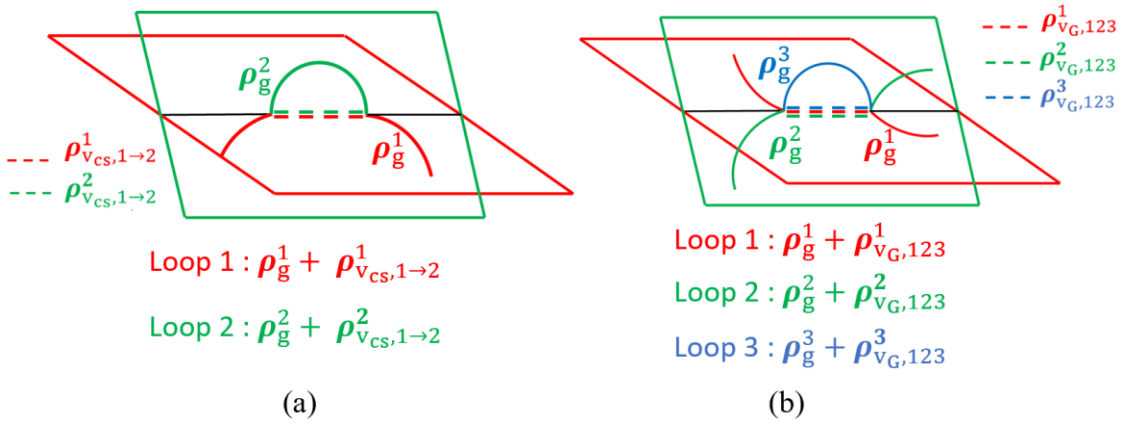

Fig. 3.1. Schematics showing the configuration of dislocations involved in (a) cross slip and (b) glissile junction reaction.

Since the rates of change of virtual dislocation densities of every pair of reacting slip systems are equal in magnitude but opposite in direction, their net contribution to the virtual dislocation density tensor amounts to zero. In mathematical terms, this is written in the form:

$$\boldsymbol{\alpha}_{v} = \boldsymbol{\rho}^{1}_{\mathrm{v_{cs},1\to2}} \otimes \boldsymbol{b}^{1} + \boldsymbol{\rho}^{2}_{\mathrm{v_{cs},1\to2}} \otimes \boldsymbol{b}^{2} = \left(\boldsymbol{\rho}^{1}_{\mathrm{v_{cs},1\to2}} - \boldsymbol{\rho}^{1}_{\mathrm{v_{cs},1\to2}}\right) \otimes \boldsymbol{b}^{1} = 0 \tag{3.22}$$

Similarly, consider the case of glissile junction in Fig. 3.1(b). The glissile junction configuration can be thought of as three dislocation loops contained in their respective slip system such that a portion of each loop overlaps which is represented by the dotted lines. In this case, the red and green dotted lines correspond to virtual density in slip system 1 and 2, $\boldsymbol{\rho}^{1}_{\mathrm{v_G,123}}$ and $\boldsymbol{\rho}^{2}_{\mathrm{v_G,123}}$ respectively, which represents the part of the dislocation loop on slip system 1 and 2 involved in the glissile junction reaction and is no longer available to glide. The blue dotted line is the virtual density for slip system 3, $\boldsymbol{\rho}^{3}_{\mathrm{v_G,123}}$ that closes the loop on slip system 3. In Fig. 3.1 (b), the dislocation bowing out after the glissile junction reaction between slip system 1 and 2 is represented as $\boldsymbol{\rho}^{3}_{\mathrm{g}}$. The rate of change of virtual densities of slip system 1,2 and 3 for a glissile junction reaction is given by the equation below.

$$\dot{\boldsymbol{\rho}}^{1}_{\mathrm{v_G,123}} = \dot{\boldsymbol{\rho}}^{2}_{\mathrm{v_G,123}} = -\dot{\boldsymbol{\rho}}^{3}_{\mathrm{v_G,123}} = \dot{r}_{\mathrm{G,123}}\left(\boldsymbol{\rho}^{1}_{\mathrm{g}} \cdot \boldsymbol{e}_{12}\right)\left(\boldsymbol{\rho}^{2}_{\mathrm{g}} \cdot \boldsymbol{e}_{12}\right)\boldsymbol{e}_{12} \tag{3.23}$$

The rate of change of virtual density on the third slip system $\dot{\boldsymbol{\rho}}^{3}_{\mathrm{v_G},123}$ is equal in magnitude to $\dot{\boldsymbol{\rho}}^{1}_{\mathrm{v_G},123}$, $\dot{\boldsymbol{\rho}}^{2}_{\mathrm{v_G},123}$ but opposite in direction. Hence, the net contribution of these virtual densities to virtual dislocation density tensor can be shown to be zero using Frank's rule as follows

$$\boldsymbol{\alpha}_{\mathrm{v}} = \boldsymbol{\rho}^{1}_{\mathrm{v_G},123}\otimes\boldsymbol{b}^{1} + \boldsymbol{\rho}^{2}_{\mathrm{v_G},123}\otimes\boldsymbol{b}^{2} + \boldsymbol{\rho}^{3}_{\mathrm{v_G},123}\otimes\boldsymbol{b}^{3} = \boldsymbol{\rho}^{1}_{\mathrm{v_G},123}(\boldsymbol{b}^{1} + \boldsymbol{b}^{2} - \boldsymbol{b}^{3}) = 0, \quad (3.24)$$

when the reaction occurs such that $\boldsymbol{b}^{1} + \boldsymbol{b}^{2} = \boldsymbol{b}^{3}$. Generalizing the two cases discussed above to all types of dislocation reactions and slip systems, the virtual dislocation density evolution equation can be written as:

$$\dot{\boldsymbol{\rho}}^{i}_{\mathrm{v}} = \dot{\boldsymbol{\rho}}^{i}_{\mathrm{v_{cs}},i\to j} + \sum_{j,k}\dot{\boldsymbol{\rho}}_{\mathrm{v_G},ijk} + \sum_{j}\dot{\boldsymbol{\rho}}_{\mathrm{v_L},ij} + \sum_{j}\dot{\boldsymbol{\rho}}_{\mathrm{v_H},ij} - \dot{\boldsymbol{\rho}}_{\mathrm{cs},j\to i} - \sum_{j,k}\dot{\boldsymbol{\rho}}_{\mathrm{v_G},jki}. \quad (3.25)$$

Based on the above definitions, the dislocation configuration can be envisioned as an ensemble of loops represented with continuous densities, each made up of glide and virtual dislocation densities entirely contained in the individual slip systems. The sum of both the glide and virtual dislocation densities from here on will be referred to as boundary vector density as it characterizes the boundary of the slipped area on any given slip system. The evolution of the boundary vector density is captured by equation (3.18) and equation (3.25) which yields us the curl-type dislocation transport term since the reaction terms in equation (3.18) and (3.25) cancel each other out as per their definitions. Since, divergence of curl is zero, the boundary vector density will always be divergence free provided the initial configuration is divergence free.

Hence, the dislocation closure can be ensured by enforcing the divergence-free condition on the boundary vector density on each slip system. That is,

$$\nabla\cdot\left(\boldsymbol{\rho}^{i}_{\mathrm{g}} + \boldsymbol{\rho}^{i}_{\mathrm{v}}\right) = 0. \quad (3.26)$$

The new form of the divergence constraint, equation (3.26), makes a significant enhancement in the accuracy of the numerical solution of the current CDD framework.

3.5 Numerical implementation

3.5.1 Time discretization

As mentioned in the earlier section, the CDD model consists of two parts: stress-equilibrium problem and the dislocation kinetic problem. The stress-equilibrium problem is solved

in the same way as in (Lin et al., 2020). As such, only the numerical scheme to solve the kinetic equations is discussed in detail in this section. The dislocation kinetic equation describes two different physics, the transport and reactions of dislocations. The dislocation transport term in the kinetics equation is a curl type convection term describing the movement of dislocations under the local stress, whereas the dislocation reactions term describes the creation and removal of dislocations for various slip systems. Typically, multi-physics problems are harder to solve since the time scale associated with each physics and the solution method required to get a stable solution may vastly be different. A common technique used to overcome this hurdle is to solve the transport-reaction equation using the operator splitting, wherein the transport and reaction physics are solved separately. In the current work, the dislocation transport part is solved first subjected to the divergence constraint to update the vector dislocation density. Then, the updated vector dislocation density is used to solve the dislocation reaction part. In doing so, the alteration of the densities due to the exchange between the glide and virtual densities does not influence the divergence-free condition (19) that is enforced during the transport solution step.

The numerical discretization for the transport part is written in the form:

$$\frac{\boldsymbol{\rho}_{\mathrm{g}}^{i,t+1} - \boldsymbol{\rho}_{\mathrm{g}}^{i,t}}{\Delta t} = \nabla \times \left(\boldsymbol{v}_{\mathrm{g}}^{i,t} \times \boldsymbol{\rho}_{\mathrm{g}}^{i,t+1}\right), \tag{3.27}$$

with $\boldsymbol{\rho}_{\mathrm{g}}^{i,t+1}$ and $\boldsymbol{\rho}_{\mathrm{g}}^{i,t}$ being the glide density at the beginning and end of the time step Δt. As indicated above, the velocity field $\boldsymbol{v}_{\mathrm{g}}^{i,t}$ is supplied from the previous step due to the staggered scheme of solving the crystal mechanics and transport subproblems. Aside from that, the transport equations themselves are solved using an implicit scheme, which ensures numerical stability of the solution. The transport equation (3.27) is solved subject to the divergence constraint, which is now applied at the slip system level with the help of the virtual density,

$$\nabla \cdot \left(\boldsymbol{\rho}_{\mathrm{g}}^{i,t+1} + \boldsymbol{\rho}_{\mathrm{v}}^{i,t}\right) = 0. \tag{3.28}$$

Upon updating the dislocation density due to dislocation transport, the dislocation reactions are used to update the glide and virtual densities due to reactions. The discretized forms of the corresponding rate terms are:

Glissile junction reactions:

$$\left.\frac{\boldsymbol{\rho}_{\mathrm{g}}^{i,t+1}-\boldsymbol{\rho}_{\mathrm{g}}^{i,t}}{\Delta t}\right|_{\mathrm{G}}=\sum_{j,k}\dot{r}_{\mathrm{G},jki}(\boldsymbol{\rho}_{\mathrm{g}}^{j,t+1}\cdot\boldsymbol{e}_{jk})(\boldsymbol{\rho}_{\mathrm{g}}^{k,t+1}\cdot\boldsymbol{e}_{jk})\,\boldsymbol{e}_{jk} \tag{3.29}$$

$$-\sum_{j,k}\dot{r}_{\mathrm{G},ijk}\left(\boldsymbol{\rho}_{\mathrm{g}}^{i,t+1}\cdot\boldsymbol{e}_{ij}\right)\left(\boldsymbol{\rho}_{\mathrm{g}}^{j,t+1}\cdot\boldsymbol{e}_{ij}\right)\boldsymbol{e}_{ij},$$

$$\left.\frac{\boldsymbol{\rho}_{\mathrm{v}}^{i,t+1}-\boldsymbol{\rho}_{\mathrm{v}}^{i,t}}{\Delta t}\right|_{\mathrm{G}}=\sum_{j,k}\dot{r}_{\mathrm{G},ijk}(\boldsymbol{\rho}_{\mathrm{g}}^{i,t+1}\cdot\boldsymbol{e}_{ij})(\boldsymbol{\rho}_{\mathrm{g}}^{j,t+1}\cdot\boldsymbol{e}_{ij})\boldsymbol{e}_{ij} \tag{3.30}$$

$$-\sum_{j,k}\dot{r}_{\mathrm{G},jki}\left(\boldsymbol{\rho}_{\mathrm{g}}^{j,t+1}\cdot\boldsymbol{e}_{jk}\right)\left(\boldsymbol{\rho}_{\mathrm{g}}^{k,t+1}\cdot\boldsymbol{e}_{jk}\right)\boldsymbol{e}_{jk}.$$

Lomer junction reactions:

$$\left.\frac{\boldsymbol{\rho}_{\mathrm{g}}^{i,t+1}-\boldsymbol{\rho}_{\mathrm{g}}^{i,t}}{\Delta t}\right|_{\mathrm{L}}=-\sum_{j}\dot{r}_{\mathrm{L},ij}\left(\boldsymbol{\rho}_{\mathrm{g}}^{i,t+1}\cdot\boldsymbol{e}_{ij}\right)\left(\boldsymbol{\rho}_{\mathrm{g}}^{j,t+1}\cdot\boldsymbol{e}_{ij}\right)\boldsymbol{e}_{ij}, \tag{3.31}$$

$$\left.\frac{\boldsymbol{\rho}_{\mathrm{v}}^{i,t+1}-\boldsymbol{\rho}_{\mathrm{v}}^{i,t}}{\Delta t}\right|_{\mathrm{L}}=\sum_{j}\dot{r}_{\mathrm{L},ij}(\boldsymbol{\rho}_{\mathrm{g}}^{i,t+1}\cdot\boldsymbol{e}_{ij})(\boldsymbol{\rho}_{\mathrm{g}}^{j,t+1}\cdot\boldsymbol{e}_{ij})\boldsymbol{e}_{ij} \tag{3.32}$$

Hirth junction reactions:

$$\left.\frac{\boldsymbol{\rho}_{\mathrm{g}}^{i,t+1}-\boldsymbol{\rho}_{\mathrm{g}}^{i,t}}{\Delta t}\right|_{\mathrm{H}}=-\sum_{j}\dot{r}_{\mathrm{H},ij}\left(\boldsymbol{\rho}_{\mathrm{g}}^{i,t+1}\cdot\boldsymbol{e}_{ij}\right)\left(\boldsymbol{\rho}_{\mathrm{g}}^{j,t+1}\cdot\boldsymbol{e}_{ij}\right)\boldsymbol{e}_{ij}, \tag{3.33}$$

$$\left.\frac{\boldsymbol{\rho}_{\mathrm{v}}^{i,t+1}-\boldsymbol{\rho}_{\mathrm{v}}^{i,t}}{\Delta t}\right|_{H}=\sum_{j}\dot{r}_{H,ij}(\boldsymbol{\rho}_{\mathrm{g}}^{i,t+1}\cdot\boldsymbol{e}_{ij})(\boldsymbol{\rho}_{\mathrm{g}}^{j,t+1}\cdot\boldsymbol{e}_{ij})\boldsymbol{e}_{ij} \tag{3.34}$$

Cross-slip:

$$\left.\frac{\boldsymbol{\rho}_{\mathrm{g}}^{i,t+1}-\boldsymbol{\rho}_{\mathrm{g}}^{i,t}}{\Delta t}\right|_{\mathrm{cs}}=\dot{r}_{j\to i}\boldsymbol{\rho}_{\mathrm{g}}^{j,t+1}-\dot{r}_{i\to j}\boldsymbol{\rho}_{\mathrm{g}}^{i,t+1}, \tag{3.35}$$

$$\left.\frac{\boldsymbol{\rho}_{\mathrm{v}}^{i,t+1}-\boldsymbol{\rho}_{\mathrm{v}}^{i,t}}{\Delta t}\right|_{\mathrm{cs}}=-\dot{r}_{j\to i}\boldsymbol{\rho}_{\mathrm{g}}^{j,t+1}+\dot{r}_{i\to j}\boldsymbol{\rho}_{\mathrm{g}}^{i,t+1}. \tag{3.36}$$

In the case of junction reactions, the discretized equations are non-linear, and are thus first linearized with the help of first order Taylor series expansion before using a linear solver. For example, consider the first term on the right side of equation (3.29). The term $\dot{r}_{\mathrm{G},jki}\left(\boldsymbol{\rho}_{\mathrm{g}}^{j,t+1}\cdot\boldsymbol{e}_{jk}\right)\left(\boldsymbol{\rho}_{\mathrm{g}}^{k,t+1}\cdot\boldsymbol{e}_{jk}\right)\boldsymbol{e}_{jk}$ is of the form $f(x^{t+1},y^{t+1})$ where x and y are the dislocation densities in slip system j and k. Based on first order multi-variable Taylor series expansion $f(x^{t+1},y^{t+1})=$

$f(x^t, y^t) + f_x(x^t, y^t)(y^{t+1} - y^t) + f_y(x^t, y^t)(x^{t+1} - x^t)$, the first term can then be linearized as follows:

$$\begin{aligned} \dot{r}_{\mathrm{G},jki}(\boldsymbol{\rho}_{\mathrm{g}}^{j,t+1} \cdot \boldsymbol{e}_{jk})(\boldsymbol{\rho}_{\mathrm{g}}^{k,t+1} \cdot \boldsymbol{e}_{jk})\boldsymbol{e}_{jk} \;=\; & \dot{r}_{\mathrm{G},jki}\big[(\boldsymbol{\rho}_{\mathrm{g}}^{j,t} \cdot \boldsymbol{e}_{jk})\boldsymbol{e}_{jk} \otimes \boldsymbol{e}_{jk} \cdot \boldsymbol{\rho}_{\mathrm{g}}^{k,t+1} \\ & + (\boldsymbol{\rho}_{\mathrm{g}}^{k,t} \cdot \boldsymbol{e}_{jk})\boldsymbol{e}_{jk} \otimes \boldsymbol{e}_{jk} \cdot \boldsymbol{\rho}_{\mathrm{g}}^{j,t+1} \\ & - (\boldsymbol{\rho}_{\mathrm{g}}^{j,t} \cdot \boldsymbol{e}_{jk})(\boldsymbol{\rho}_{\mathrm{g}}^{k,t} \cdot \boldsymbol{e}_{jk})\boldsymbol{e}_{jk}\big]. \end{aligned} \tag{3.37}$$

Other junction reaction equations are linearized in the same fashion.

3.5.2 Finite element discretization of the dislocation transport equations

In this formulation, the glide dislocation density of each slip system is expressed as a 2D vector with components ρ_{g1} and ρ_{g2} within a local coordinate system in which the right-handed coordinates x_1, x_2 and x_3 are, respectively, along the Burgers vector (screw dislocation orientation), the edge dislocation direction, and the slip plane normal. The dislocation transport equations are then assembled in terms of the glide dislocation density for slip system i as follows

$$\left[[A_t] + \Delta t * \left(-[A_0] - [A_1]\frac{\partial}{\partial x_1} - [A_2]\frac{\partial}{\partial x_2}\right)\right]\{\rho_{\mathrm{g}}^i\}^{t+1} = [A_t]\{\rho_{\mathrm{g}}^i\}^t. \tag{3.38}$$

Similarly, the divergence constraint can be assembled as

$$[A_{\mathrm{div}}]\,\{\rho_{\mathrm{g}}^i\}^{t+1} = -[A_{\mathrm{div}}]\,\{\rho_{\mathrm{v}}^i\}^t, \tag{3.39}$$

where $\{\rho_{\mathrm{g}}^i\}$=$\{\rho_{\mathrm{g1}}^i, \rho_{\mathrm{g2}}^i\}^T$ corresponds to the components of glide dislocation density of slip system i at time step t and $\{\rho_{\mathrm{v}}^i\} = \{\rho_{\mathrm{v1}}^i, \rho_{\mathrm{v2}}^i\}^T$ corresponds to the components of virtual dislocation density slip system i at time step t and $[A_t]$, $[A_0]$, $[A_1]$, $[A_2]$ are the coefficients matrices. For a single slip system, the coefficient matrices $[A_t]$, $[A_0]$, $[A_1]$, $[A_2]$ and $[A_{\mathrm{div}}]$ are defined as follows

$$[A_t] = \begin{bmatrix} 1 & 0 \\ 0 & 1 \end{bmatrix}, \qquad [A_0] = \begin{bmatrix} -\dfrac{\partial v_2}{\partial x_2} & \dfrac{\partial v_1}{\partial x_2} \\ \dfrac{\partial v_2}{\partial x_1} & -\dfrac{\partial v_1}{\partial x_1} \end{bmatrix}, \qquad [A_1] = \begin{bmatrix} 0 & 0 \\ -v_2 & v_1 \end{bmatrix}, \tag{3.40}$$

$$[A_2] = \begin{bmatrix} -v_2 & v_1 \\ 0 & 0 \end{bmatrix}, \qquad [A_{\mathrm{div}}] \;=\; \left[\frac{\partial}{\partial x_1}\ \frac{\partial}{\partial x_2}\right].$$

Within the finite element framework, the glide dislocation density of the ith slip system over an element with M nodes can be expressed in terms of shape functions and the nodal values of that element as follows:

$$\begin{Bmatrix}\rho_{g1}^{i}\\ \rho_{g2}^{i}\end{Bmatrix} = N\begin{Bmatrix}\rho_{g1}^{i,1}\\ \rho_{g2}^{i,1}\\ \rho_{g1}^{i,2}\\ \rho_{g2}^{i,2}\\ \vdots\\ \rho_{g1}^{i,M}\\ \rho_{g2}^{i,M}\end{Bmatrix}, \qquad \frac{\partial}{\partial x_1}\begin{Bmatrix}\rho_{g1}^{i}\\ \rho_{g2}^{i}\end{Bmatrix} = B_1\begin{Bmatrix}\rho_{g1}^{i,1}\\ \rho_{g2}^{i,1}\\ \rho_{g1}^{i,2}\\ \rho_{g2}^{i,2}\\ \vdots\\ \rho_{g1}^{i,M}\\ \rho_{g2}^{i,M}\end{Bmatrix}, \qquad \frac{\partial}{\partial x_2}\begin{Bmatrix}\rho_{g1}^{i}\\ \rho_{g2}^{i}\end{Bmatrix} = B_2\begin{Bmatrix}\rho_{g1}^{i,1}\\ \rho_{g2}^{i,1}\\ \rho_{g1}^{i,2}\\ \rho_{g2}^{i,2}\\ \vdots\\ \rho_{g1}^{i,M}\\ \rho_{g2}^{i,M}\end{Bmatrix}, \tag{3.41}$$

with $\rho_{g1}^{i,K}$ and $\rho_{g2}^{i,K}$, $K \in \{1, M\}$, being the value of glide dislocation density components at all nodes, and $[N]$, $[B_1]$ and $[B_2]$ are matrices containing the collection of elemental shape functions, $\{N\}$, and their derivative with respect to x_1 and x_2, respectively. These matrices are expressed in the form:

$$[N] = \begin{bmatrix} N_1 & 0 & N_2 & 0 & \cdots & N_M & 0 \\ 0 & N_1 & 0 & N_2 & \cdots & 0 & N_M \end{bmatrix} \tag{3.42}$$

$$[B_1] = \begin{bmatrix} \dfrac{\partial N_1}{\partial x_1} & 0 & \dfrac{\partial N_2}{\partial x_1} & \cdots & \dfrac{\partial N_M}{\partial x_1} & 0 \\ 0 & \dfrac{\partial N_1}{\partial x_1} & 0 & \cdots & 0 & \dfrac{\partial N_M}{\partial x_1} \end{bmatrix}; \tag{3.43}$$

$$[B_2] = \begin{bmatrix} \dfrac{\partial N_1}{\partial x_2} & 0 & \dfrac{\partial N_2}{\partial x_2} & \cdots & \dfrac{\partial N_M}{\partial x_2} & 0 \\ 0 & \dfrac{\partial N_1}{\partial x_2} & 0 & \cdots & 0 & \dfrac{\partial N_M}{\partial x_2} \end{bmatrix}.$$

With these expressions at hand, the dislocation transport equations (3.38) can be rewritten in terms of the nodal degrees of freedom in a more compact form,

$$[L]\{\rho_g^i\}^{t+1} = [W]\{\rho_g^i\}^t, \tag{3.44}$$

where the matrices $[L]$ and $[W]$ given by

$$[L] = [A_t][N] - \Delta t * ([A_0][N] + [A_1][B_1] + [A_2][B_2]), \tag{3.45}$$

$$[W] = [A_t][N]. \tag{3.46}$$

Likewise, the divergence constraint can be expressed in the form:

$$[B_{\text{div}}]\{\rho_{\text{g}}^{i}\}^{t+1} = -[B_{\text{div}}]\{\rho_{\text{v}}^{i}\}^{t}, \tag{3.47}$$

With

$$[B_{\text{div}}] = \left[\frac{\partial N_1}{\partial x_1} \quad \frac{\partial N_1}{\partial x_2} \quad \frac{\partial N_2}{\partial x_1} \quad \frac{\partial N_2}{\partial x_1} \ \ldots\ldots \ \frac{\partial N_M}{\partial x_1} \quad \frac{\partial N_M}{\partial x_2}\right]. \tag{3.48}$$

The above set of equations can be generalized to all slip systems and solved using Least Squares Finite Element Method (LSFEM) (Jiang, 2011; Xia and El-Azab, 2015; Lin et al., 2020). Skipping details, the global system of equations takes on the form:

$$[K]\{\rho_{\text{g}}\}^{t+1} = \{P\}, \tag{3.49}$$

with $[K]$ and $\{P\}$ given by

$$[K] = \int \left([L^T][L] + ch^2\left[B_{\text{d}}{}^T\right][B_{\text{d}}]\right)d\Omega \tag{3.50}$$

$$\{P\} = \int \left([L^T][W]\{\rho_{\text{g}}\}^{t} + ch^2\left[B_{\text{d}}{}^T\right][B_{\text{d}}]\{\rho_{\text{v}}\}^{t}\right)d\Omega.$$

In the above, the parameter c corresponds to the control parameter used to impose the divergence constraint and h is the mesh size.

Solving the system (3.49) will update the glide density due to dislocation transport on all slip systems in a decoupled fashion, meaning that equation (3.49) can be solved for one slip system at a time, thanks to the introduction of the virtual density. The dislocation reactions can then be used to update the glide and virtual densities.

3.6 Results

The significance of the virtual dislocation density is highlighted first by comparing the results for some test problems with and without consideration of the virtual density in the dislocation transport-reaction formulation in Section 3.6.1 - 3.6.3. Since the purpose of the test problems is to demonstrate the effectiveness of the new divergence constraint, the system dynamics is evolved by enforcing a constant velocity and the reaction rates for cross-slip and glissile junction are treated to be a constant. Following this, the results for full bulk simulations are then presented in Section 3.6.4. In all the simulations, a crystal volume of dimensions

5μm×5μm×5.303μm has been used, with periodic boundary conditions. The mesh used consists of tetrahedron and pyramid elements as proposed by (Xia and El-Azab, 2015). The mesh size is chosen such that it is on the order of the annihilation distance of opposite dislocations, thus conforming to the notion of the bundle representation of dislocations. The initial dislocation configuration is created in the form of loops with Gaussian distributed density over the cross section, with the center of the dislocation loop and the loop radius width as parameters. For the sake of brevity, from here onward, we will refer to the formulation without the virtual density as the *coupled formulation* and that with the virtual density as *decoupled formulation*. The reader is reminded again that, in the coupled formulation, the divergence constraint is enforced on all slip systems at once and therefore the scheme solves for all densities in a coupled fashion, versus enforcing the divergence constraint on individual slip systems thus solving for the slip system densities individually in the decoupled formulation.

3.6.1 Dislocation loop expansion under a prescribed velocity

In this test, a single dislocation loop in a FCC crystal on the slip system 1, $(111)[0\bar{1}1]$, was allowed to expand under a constant applied velocity of 0.03 μm/ns normal to its line tangent everywhere. The loop expansion problem was solved by using the dislocation transport equation (28) coupled with a divergence constraint. In the case of a single loop, there is no dislocation reaction involved and hence the divergence constraint can be applied to the slip system mentioned above in a straightforward fashion. However, in order to show the effect of coupling of slip system solutions through the divergence constraint, this problem was also solved by coupling slip system 1 with its cross-slip system 2, $(\bar{1}11)[0\bar{1}1]$, (coupled formulation), with the latter having no dislocations initially. Ideally, the latter slip system should continue to have no density during the evolution. Fig. 3.2 shows the results of both formulations; the decoupled solution is shown in part (a) while the coupled solution is shown in part (b). Although cross slip was not activated, the coupled formulation populates dislocations on slip system 2 due to numerical errors that grow with time. The fact that coupling introduces spurious densities serves as a motivation to use the decoupled formulation, which is made possible by introducing the virtual dislocation density. As the simulation progresses, these spurious densities increase in magnitude, which can be seen in Fig. 3.3.

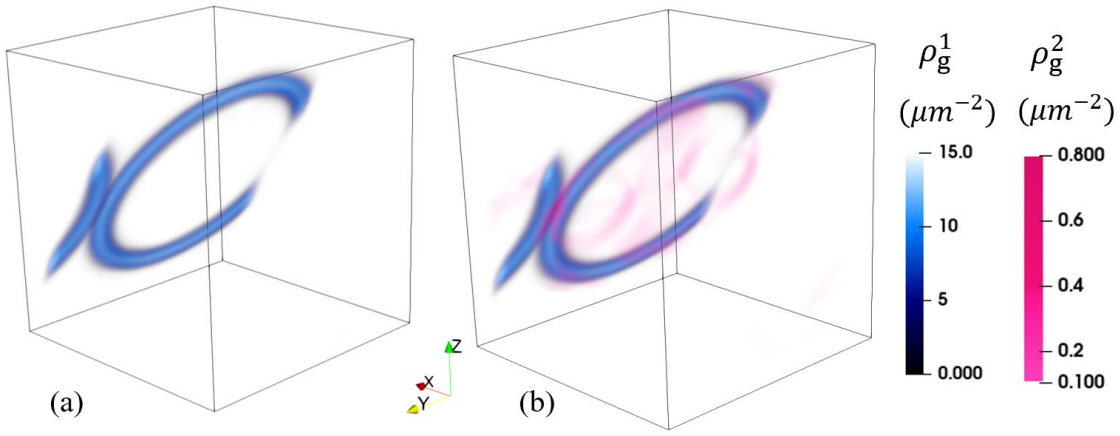

Fig. 3.2. Loop expansion test. A single loop was solved once using the decoupled formulation and another time using the coupled formulation. The results are shown in parts (a) and (b), respectively, after 30-time steps (28 ns).

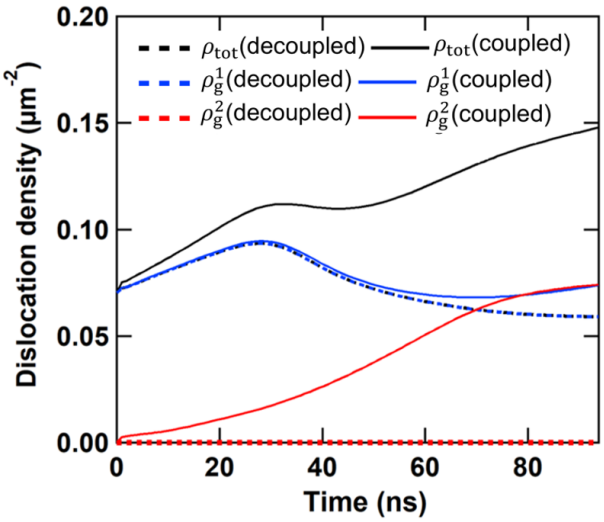

Fig. 3.3. Evolution of the average dislocation density in the dislocation loop expansion test. The dashed and solid lines correspond to decoupled and coupled formulations, respectively. The density ρ_{tot} is the sum of ρ_g^1 and ρ_g^2. In the case of the decoupled formulation, the total density coincides with ρ_g^1 as should be.

3.6.2 Cross slip test with a prescribed applied velocity

Cross slip is a thermally activated process through which a dislocation changes its glide plane to a cross slip plane while retaining the same Burgers vector. In this test case, a single loop on the slip system 1, $(111)[0\bar{1}1]$, was considered. The simulation was setup such that cross-slip

is allowed to happen for all dislocations with screw orientation. The velocity on the cross-slip plane was arbitrarily taken to be 0.1 μm/ns compared to 0.01 μm/ns on the original plane. This transport-reaction problem was solved using both coupled and decoupled formulations with a constant cross slip rate ($\dot{r}_{1\to 2} = 0.1$/ns). Fig. 3.4 (a) and (b) shows the results with the decoupled and coupled formulations, respectively after 30 time steps (8 ns). It is clearly shown that the coupled solution results in spurious density of dislocation on the cross-slip system. Such spurious densities result mainly through the divergence constraint. The effect of these spurious densities on the total density evolution in the domain of the simulation is shown in Fig. 3.5. While both solutions for the decoupled and coupled formulations on the main slip system are fairly close to each other, the solutions on the cross-slip plane for the two formulations differ significantly, thus resulting in a significant difference in the total density.

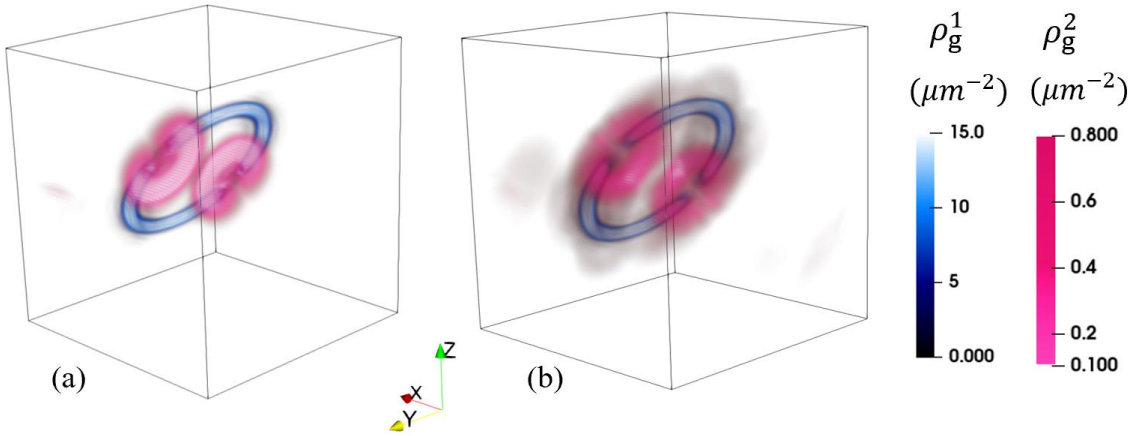

Fig. 3.4. Dislocation cross slip simulated using (a) the decoupled and (b) coupled formulations. In the case of decoupled formulation, the density on the cross-slip plane has no spurious values as it is the case in the coupled formulation.

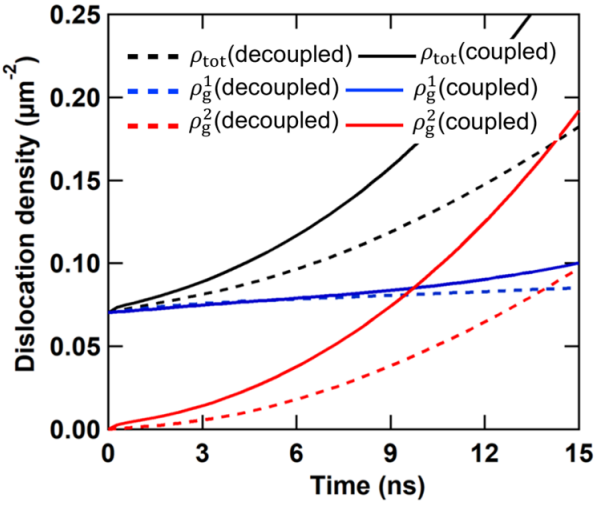

Fig. 3.5. Evolution of the average dislocation density for the cross-slip test with constant velocity on the glide plane and cross slip planes. The dashed and solid lines correspond to decoupled and coupled formulations, respectively. The density ρ_{tot} is the sum of ρ_g^1 and ρ_g^2.

3.6.3 Glissile junction reaction under constant applied velocity

Glissile junction reactions represent a major mechanism of dislocation multiplication in multi-slip problems (Stricker et al., 2015; Stricker et al., 2018). In this test case, this dislocation reaction was studied by placing two dislocation loops on two slip systems, $(111)[0\bar{1}1]$ and $(\bar{1}11)[101]$. The dislocation loops on both slip systems were allowed to expand by imposing a constant velocity of 0.03 μm/ns. The glissile junction reaction between the dislocations was allowed to occur if the orientation criteria proposed by (Madec et al., 2002; Lin and El-Azab, 2020) was satisfied. This transport-reaction problem was solved with a constant glissile junction rate ($\dot{r}_{G,123} = 0.5\ \mu m^2/ns$) using both coupled and decoupled formulations. The results after 30-time steps (28 ns) are shown in Fig. 3.6. From Fig. 3.6(b), it is evident that the coupled formulation populates slip system 3 with density at places where the glissile junction reaction is not happening. Such spurious density results from the coupling of the three slip systems through the divergence constraint. The effect of the spurious density is observed in the dislocation density evolution Fig. 3.7, where the total density ρ_{tot} in the coupled formulation case is always higher.

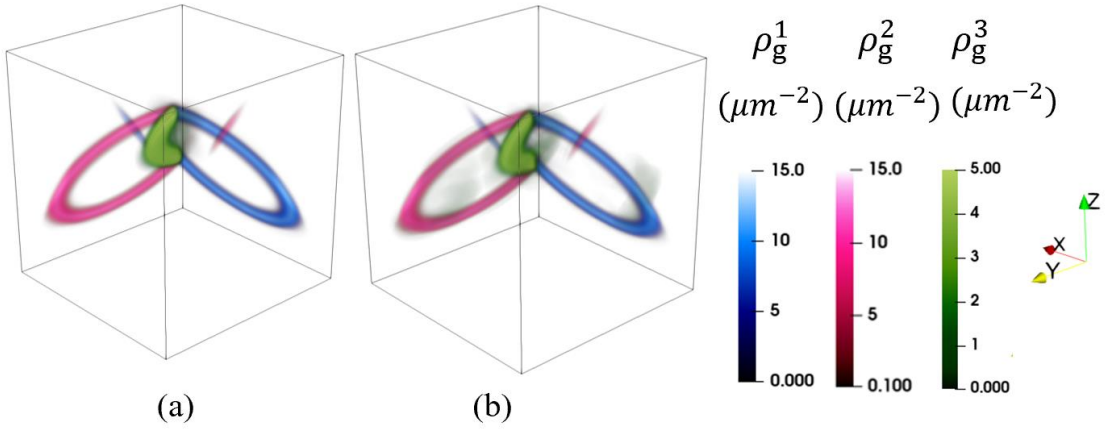

Fig. 3.6. The dislocation configuration for a glissile junction reaction from two loops simulated using the (a) decoupled and (b) coupled formulations. Again, spurious density was observed in the coupled formulation case. The pink and blue lines on the blue and pink loops in both (a) and (b) correspond to the portion of loops entering from the other side of the cube due to periodic boundary condition.

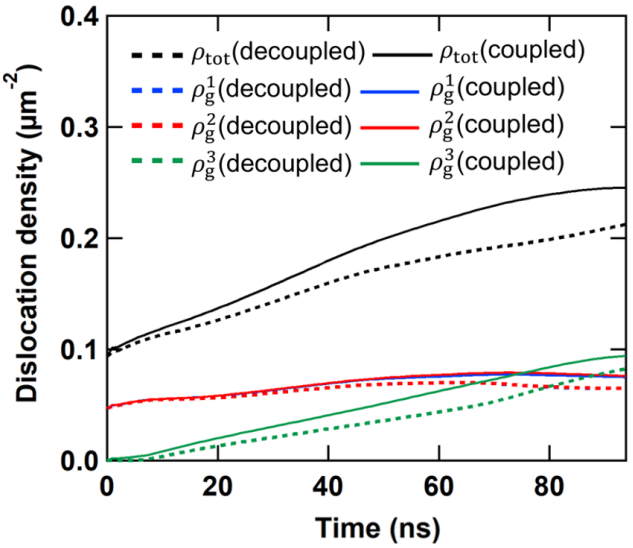

Fig. 3.7. Dislocation density evolution during a glissile junction reaction. Dashed and solid lines correspond to the decoupled and coupled formulations, respectively. The density ρ_{tot} is the sum of ρ_g^1, ρ_g^2 and ρ_g^3.

3.6.4 Bulk Simulation

In this section, a simulation of a bulk FCC crystal under uniaxial loading for the multi-slip condition based on the decoupled formulation with virtual density is discussed. Again, the

simulation domain used is a 5μm×5μm×5.303μm box which is discretized using tetrahedral and pyramid elements. The mesh size used is around 62.5nm. The material parameters used in this simulation are specified in Table 3.1. The system was subjected to a strain-rate controlled loading with an applied strain rate of 20/s along [001] direction. All 12 slip systems were populated with 10 circular dislocation loops (circular bundles) each. The radius of the dislocation loop was chosen randomly between 2 μm and 4 μm and their centers were placed randomly in the crystal.

The dislocation velocity for each slip system i is defined based on linear mobility law commonly used in literature (Zaiser et al., 2001; Yefimov et al., 2004; Lin and El-Azab, 2020) as follows

$$v^i = \frac{b}{B}\langle|\tau|^i - \left(\tau_0 + \tau_{\mathrm{p}}^i\right)\rangle sgn\left(\tau^i\right) \tag{3.51}$$

where b is the magnitude of the Burgers vector and B is the drag coefficient. The $\langle\cdot\rangle$ corresponds to the Macauley bracket and sgn function corresponds to the signature of the argument inside. τ^i is the resolved shear stress along slip system i and τ_0 is the lattice friction. τ_{p}^i is the Taylor hardening stress that accounts for short range interactions due to sessile junctions on slip system i which is defined as

$$\tau_{\mathrm{p}}^i = \alpha\mu b\sqrt{\sum_j a_{ij}\rho^j}\; f\left(\rho^i,\rho^f\right); \qquad f\left(\rho^i,\rho^f\right) = \frac{1}{1 + ae^{\left(b\frac{\rho^i}{\rho^f} - 1\right)}} \tag{3.52}$$

where a_{ij} is the average strength of an interaction between slip system i and j, and ρ^j is the dislocation density of the slip system j interacting with slip system i and $f\left(\rho^i,\rho^f\right)$ corresponds to a function that accounts for the dislocation pile up effect (Zhu et al., 2016).

Table 3.1. Bulk simulation parameters. The materials properties are those of copper.

Parameter	Value
Strain rate	$20s^{-1}$
Youngs Modulus	112.5GPa
Poisson's ratio	0.34
Initial dislocation density	$1.5\times10^{12}m^{-2}$
Burgers Vector	0.25525nm
Drag coefficient	5.5×10^{-5}Pas

It is to be noted that although the theoretical framework can incorporate all junction mechanisms, in this current numerical setup the sessile junction formation mechanisms are not considered explicitly. Only dislocation reactions like glissile junction and collinear annihilation were incorporated explicitly. Since these mechanisms are explicitly incorporated, their respective hardening coefficients were taken to be zero as they already contribute to hardening by consuming dislocations and thereby reducing the dislocations available for plastic slip. Hence, only the coefficients corresponding to Lomer and Hirth lock interactions are considered in the Taylor formula whose values were obtained from (Madec and Kubin, 2017). The function $f\left(\rho^i, \rho^f\right)$ was introduced to prevent the accumulation of dislocations due to the Taylor stress. Ideally, the explicit incorporation of formation and destruction of sessile junctions would prevent the accumulation of dislocations. The lack of such mechanism necessitates us to introduce this phenomenological function. The function $f\left(\rho^i, \rho^f\right)$ can take many different forms to capture the dislocation pileup effect. In our case, a function of the form

$$f\left(\rho^i, \rho^f\right) = \frac{1}{1 + ae^{\left(b\frac{\rho^i}{\rho^f} - 1\right)}} \tag{3.52}$$

is considered, with *a* and *b* being parameters that determine the shape and the rate at which the function decays, and ρ^f is the sum of the dislocation densities of the slip systems that react with slip system *i*. The purpose of this function, called in the sequel the decay function, is to not let the Taylor term increase the flow strength indefinitely but decay upon reaching certain values, which is motivated by the work in (Zhu et al., 2016). Two simulations with two different decay function parameters were used to compare the impact of this function on the results. The corresponding simulations are named here CDD1 and CDD2. For CDD1, the values of *a* and *b* in the decay function are 0.00015 and 5, respectively. For CDD2, the values of *a* and *b* are 0.000008 and 13, respectively. A DDD simulation using the microMegas model (Devincre et al., 2011) was performed with the same initial conditions to establish a reference point for the CDD results.

The stress-strain curve and dislocation density curves of the CDD and the DDD simulations are shown in Figs. 3.8 and 3.9, respectively. The stress-strain curve of the CDD1 and CDD2 simulations follow a similar trend with a small difference in yield point as can be seen from Fig. 3.8(a). The difference in the decay function parameters affects the flow stress, which consequently affects the yield point and dislocation density evolution as observed in Fig. 3.8(a) and (b). The

hardening rate of the CDD simulations varies in tandem with the dislocation density curve, which is evident by comparing Fig. 3.8(a) and (b), with the hardening rates being smaller than the DDD result in this case. It is to be noted that the microMegas model (Devincre et al., 2011) does not include glissile junction reactions, the presence of which is known to soften the material response at least initially. Fig. 3.9(a) and (b) shows the dislocation density evolution for all slip systems for both the CDD and DDD simulations, respectively. The dislocation densities on the eight active slip systems increase faster than those of the four inactive slip systems in both cases. However, the increase of dislocation density in the inactive slip systems is more pronounced in the case of CDD due to glissile junction formation, which couple the active and inactive slip systems and promote dislocation storage on the inactive slip systems. In the case of DDD simulation, the increase in density of slip system 8 is much higher compared to other active slip systems. This behavior resulted from the initial configuration setup and material parameters.

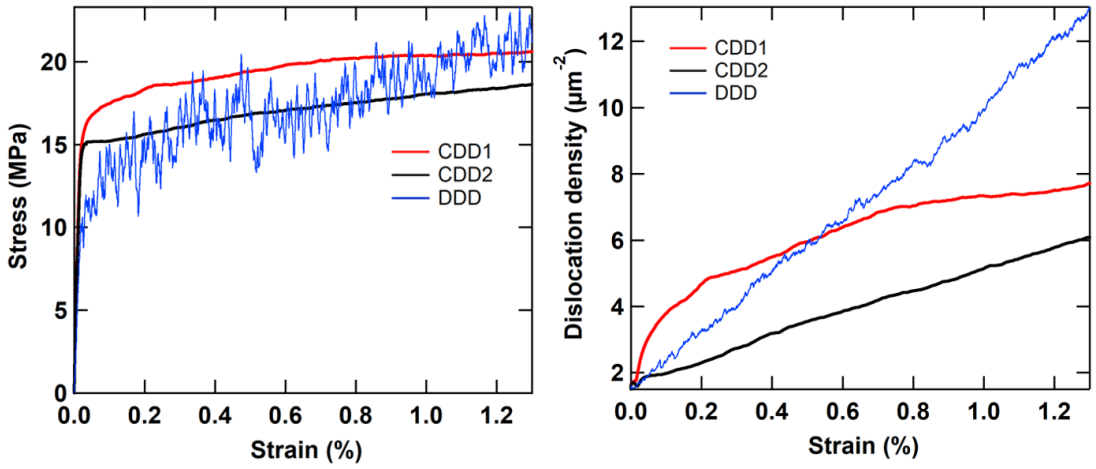

(a) (b)

Fig. 3.8. Comparison of CDD1, CDD2 and DDD simulation results. (a) Stress-strain curves. (b) Dislocation density evolution.

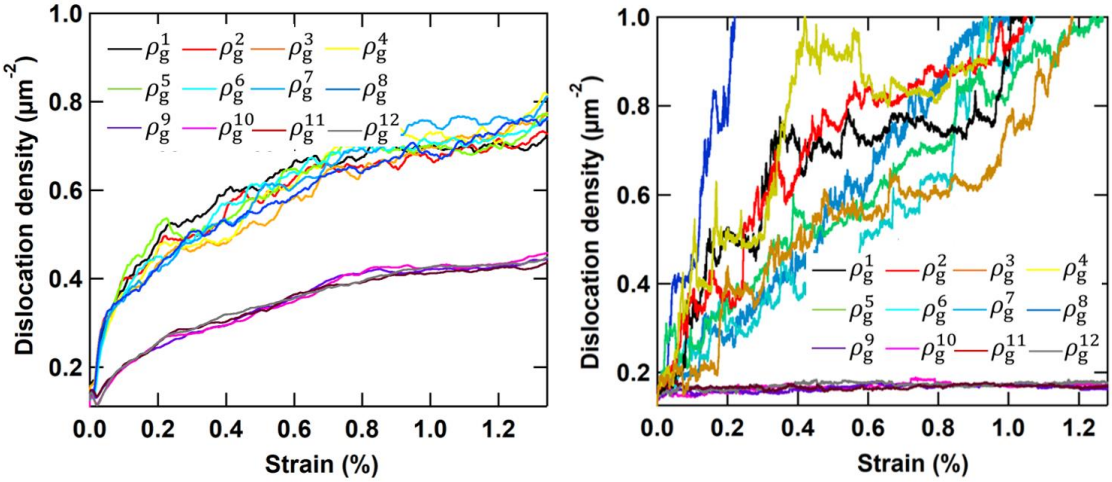

Fig. 3.9. Evolution of the slip system dislocation densities for (a) CDD1 and (b) DDD simulations. The four nominally inactive slip systems for the [001] loading store more dislocations in the case of CDD1 due to glissile junction reactions.

Dislocation microstructure

The dislocation microstructure is visualized by plotting the scalar dislocation density field in the simulation domain. This density field is obtained by summing the magnitude of the vector dislocation densities of all slip systems,

$$\rho_{\text{scalar}} = \sum_{i=1}^{12} \left\| \boldsymbol{\rho}_{\text{g}}^{i} \right\| . \tag{3.53}$$

Fig. 3.10(a) shows the dislocation distribution (pattern) over the simulation domain from the CDD1 simulation at 0.6% strain. The pattern shows features along $< 110 >$ type directions, which lie along the intersections of the FCC slip planes and are Burgers vectors directions. Accumulation of dislocations along these directions is consistent with the fact that the Taylor hardening mechanism operates mostly at the interactions of different slip planes. Glissile junctions also form along those directions. Fig. 3.10(b) shows the virtual dislocation density at a strain of 0.6%, which is determined by summing the magnitude of virtual dislocation densities of all slip systems,

$$\rho_{\text{virtual}} = \sum_{i=1}^{12} \left\| \boldsymbol{\rho}_{\text{v}}^{i} \right\| . \tag{3.54}$$

The pattern in Fig. 3.10(b) also shows clear features along $< 110 >$ type directions. Since, the virtual dislocations serve as a mark of the crystal spots where dislocation reactions and cross slip took place, it is reasonable to assume that they also can demarcate density features along $< 110 >$ type directions. Typically, the dislocations that cross-slipped or resulted from junctions, the glissile in particular, depart from the spots where such events take place via glide. Nevertheless, the dislocations involved in the most recent junction reactions and cross slip may still be close to where these events took place and thus close to where the virtual dislocations accumulate which can be observed at certain locations by comparing Fig. 3.10(a) and (b).

Fig. 3.11. shows the dislocation microstructure over the $(\bar{1}11)$, (111), (010) and (100) planes at a strain value of 0.6%. The corresponding virtual density patterns over the same planes and the same strain are shown in Fig. 3.12. In all these planes, it is noticed again that both the dislocation pattern and virtual dislocation pattern show higher density along the $< 110 >$ type directions. The areas of high dislocation density correlate with the high virtual density areas at certain locations similar to Fig. 3.10. This indicates that the dislocation pattern at any moment during the evolution of the system, although primarily caused by Taylor hardening mechanism, also depends on dislocation cross slip and junction reactions.

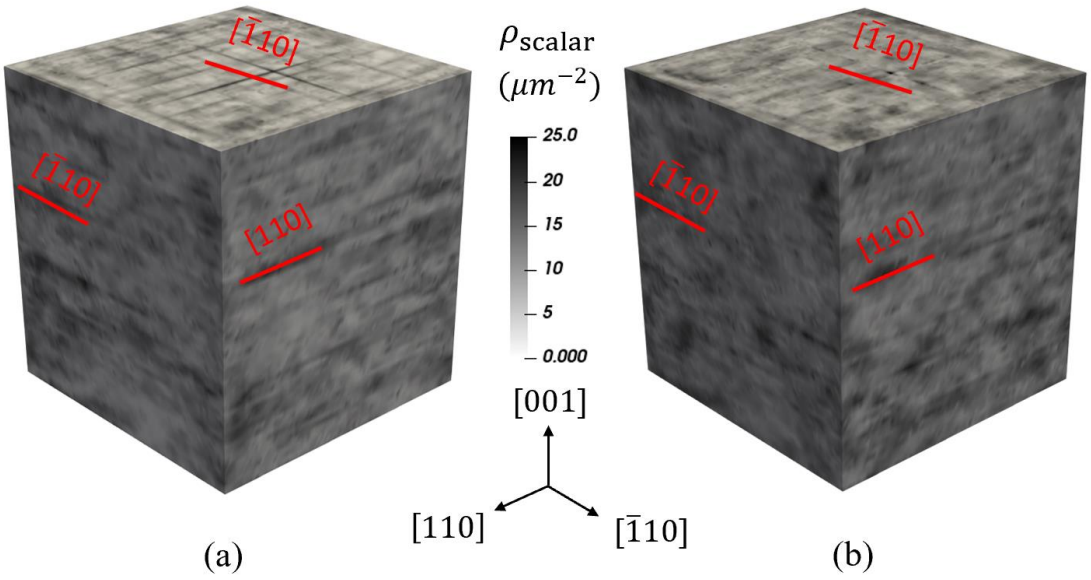

Fig. 3.10. Dislocation microstructure from the CDD1 simulation at 0.6% strain. (a) Scalar dislocation density. (b) The virtual dislocation density.

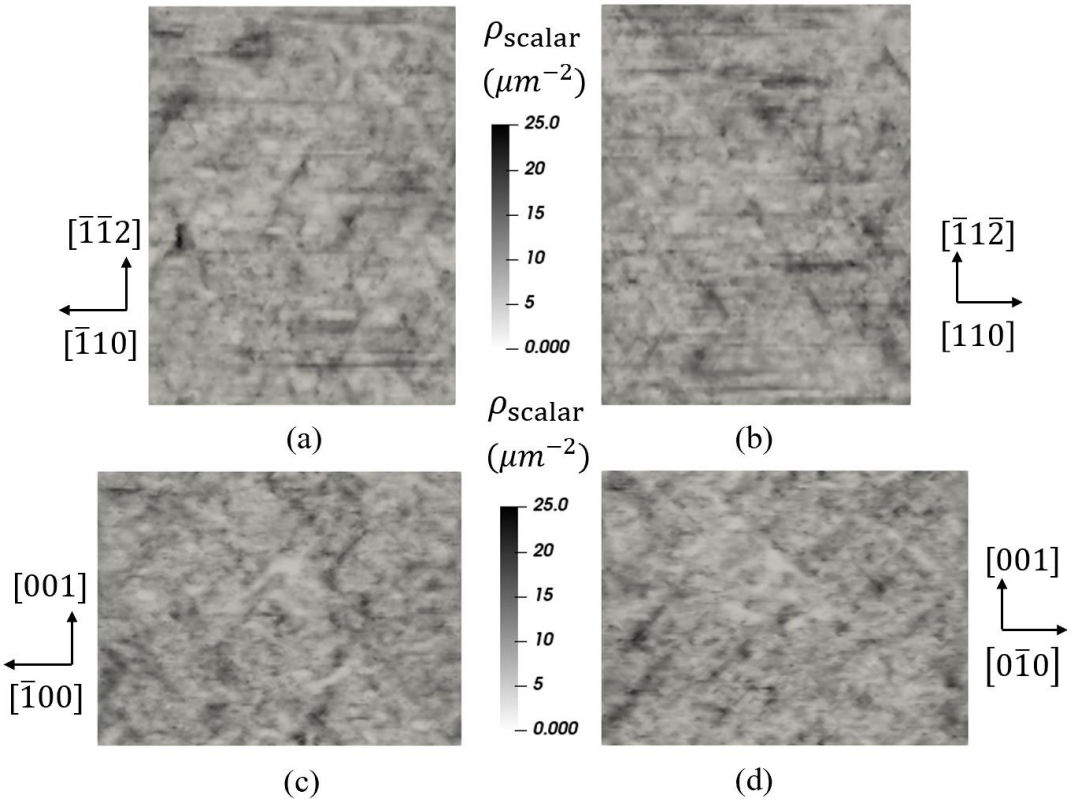

Fig. 3.11. Dislocation microstructure from the CDD1 simulation at 0.6% strain viewed on the (111), $(\bar{1}11)$, (010), and (100) planes in (a) through (d), respectively.

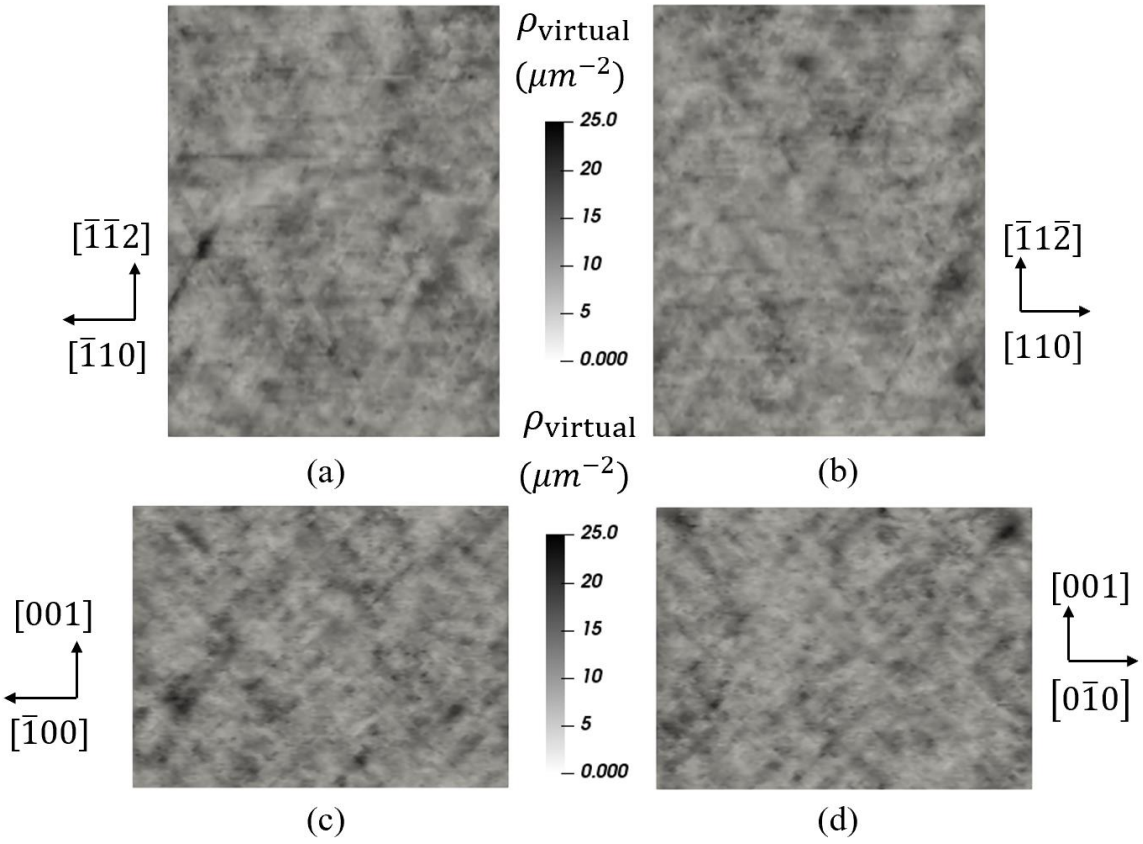

Fig. 3.12. Virtual dislocation pattern from the simulation CDD1 at 0.6% strain viewed on the (111), $(\bar{1}11)$, (010), and (100) planes in (a) through (d), respectively.

Geometrically necessary dislocation density

The dislocation microstructure can also be characterized based on the pattern formed by geometrically necessary dislocations (GNDs). GNDs are represented as tensors which are calculated based on equation (3.7). The trace norm of the GND tensor ($\|\alpha_{total}\|$) is used as a measure to visualize the pattern formed by GNDs. Fig. 3.13 shows the GND pattern formed over different planes, with data coming from CDD1 simulation at 0.6% strain. The patterns on all planes show a strong feature along the $< 110 >$ type directions, which is consistent with the results shown in Figs. 3.11 for the scalar dislocation density. The GND distribution carries the net Burgers vector distribution within the deformed grains and is thus important in fixing both the lattice rotation and the elastic strain fields, both of which are the subject of modern 3D synchrotron X-ray microscopy (Larson et al., 2002; Levine et al., 2016; Poulsen et al., 2003). These fields are also essential in understanding a phenomenon like recrystallization.

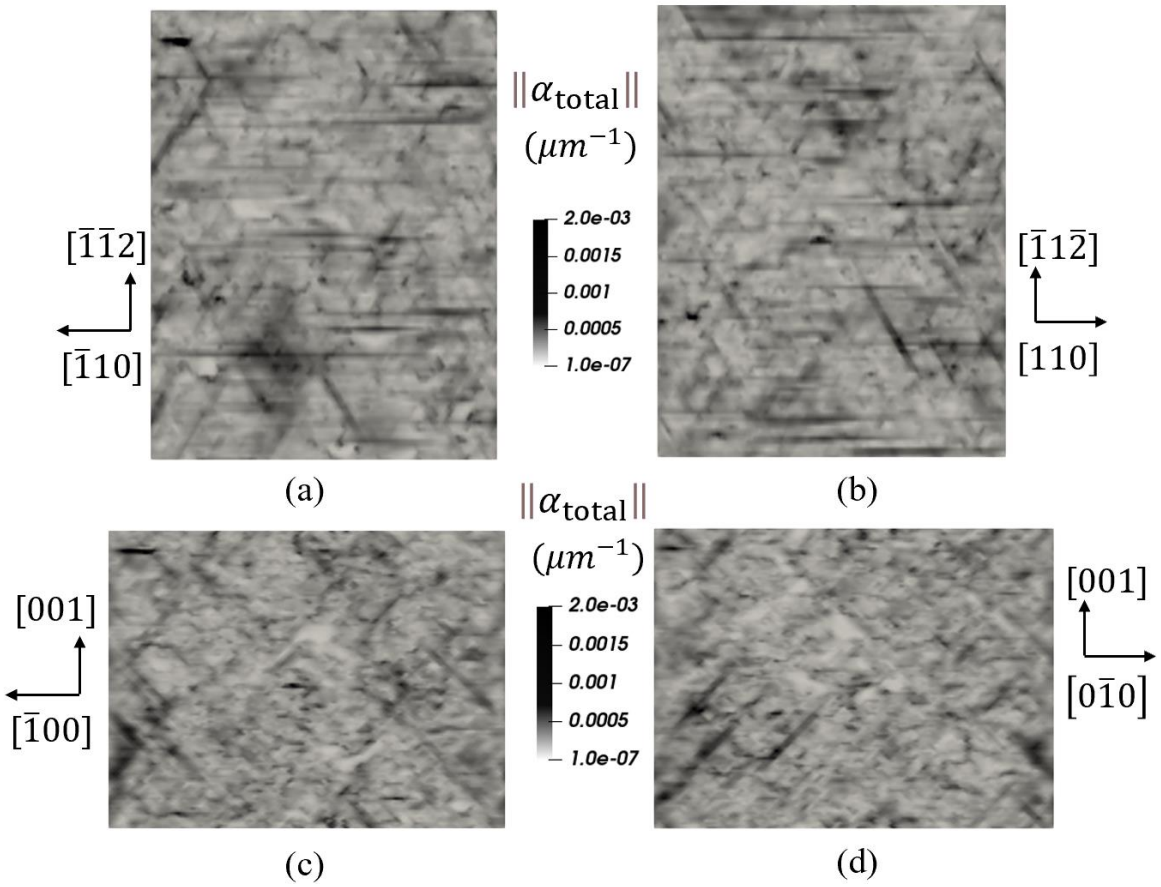

Fig. 3.13. GND pattern from the simulation CDD1 computed as the trace norm of the dislocation density tensor at 0.6% strain, and viewed on the (111), ($\bar{1}$11), (010), and (100) planes in (a) through (d), respectively.

Lattice rotation

The lattice rotation vector, Ω_k, is expressed in terms the rotation tensor, ω_{ij},

$$\Omega_k = \frac{1}{2}\,\varepsilon_{ijk}\omega_{ij} \tag{3.55}$$

The lattice rotation tensor itself is the anti-symmetric part of the elastic distortion tensor. Fig. 3.14 shows the lattice rotation vector represented as an RGB plot wherein the purely red, green and blue colors correspond to the x, y and z component of the lattice rotation vector. The RGB plot is obtained by normalizing the lattice rotation vector and mapping the scalar value of each component to RGB values. This field provides information about the abrupt lattice direction change (misorientation) across space, which demarcates the subgrain structure in deformed metals. It can

provide the so-called geometrically necessary boundaries (GNBs) and incidental dislocation boundaries (IDBs) observed in TEM experiments (Godfrey and Hughes, 1999; Hughes et al., 1997, 2003). This subgrain structure is also directly measured in 3D using synchrotron X-ray microscopy (Larson et al., 2002; Levine et al., 2016; Poulsen et al., 2003). The subgrain structure and the associated GND fields are both important in the context of recrystallization (Humphreys and Hatherly, 2012).

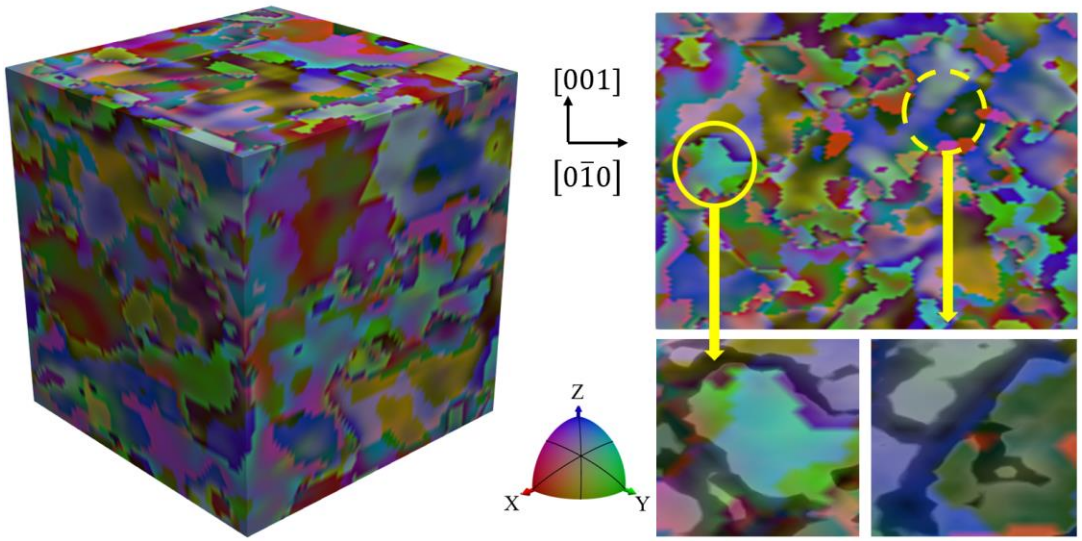

Fig. 3.14. Lattice rotation shown as RGB plot where red, green and blue corresponds to the lattice rotation components Ω_1, Ω_2 and Ω_3 while the rest of the colors represent the intermediate components of the lattice rotation vector at 0.6% strain. (a) Bulk (b) slice along (100) plane. Two regions were enlarged to show the GND density distribution (translucent black lines) superimposed on the lattice rotation fields.

Regions with no discernible change in orientation, mild change in orientation and drastic change in orientation can be observed in Fig. 3.14. These features can be used to distinguish the dislocation density distribution surrounding these regions. The uniform lattice orientation in a region corresponds to a lack of plastic strain gradient within that region, which, indicates that the region is free of dislocations. This type of profile can be observed in the region marked by the solid yellow circle where the lattice rotation is predominantly oriented along the direction

corresponding the color light blue in the RGB plot. On the other hand, drastic change in the lattice orientation corresponds to the presence of high strain gradient, which in turn indicates geometrically necessary dislocation density accumulation in that region. This type of profile can be observed in the region marked by the dashed yellow circle where the lattice rotation changes from dark green, which corresponds to a direction close to y, to blue and bluish green which corresponds to a direction close to z direction. This can be verified by overlaying the GND density distribution on the lattice rotation distribution for the regions discussed. The snippets of the zoomed in regions show the GND density superimposed on the lattice rotation fields. As expected inside the solid yellow circle region, there is no GND density in the regions with uniform lattice rotation field. Also, in the dashed yellow circle region, there is a translucent black line separating the green and bluish region indicating the dislocation accumulation on the boundary. This shows that lattice rotation is inter-related with the GND density distribution.

While Fig. 3.14 shows the salient features of the lattice rotation field in 3D, these features can be collectively understood by looking at their statistics. Fig. 3.15 shows the probability distribution function of each individual component of lattice rotation field, fit to a Gaussian curve. The Gaussian curves are fit to the raw data based on the maximum likelihood method (MLE) using MATLAB software. As expected from the data, the distribution of Ω_3 has a sharp peak and narrow width compared to the other two components. All the three components are distributed nearly symmetrically about the mean with a minor skewness which is similar to the trend observed in DDD simulations (Mohamed et al., 2015). Such a near-symmetrical feature of the distribution is characteristic of statistically homogeneous bulk plastic deformation. The mean values of the three lattice rotation components Ω_1, Ω_2, and Ω_3 are -3.7934×10^{-6o}, -5.1345×10^{-6o} and -5.697×10^{-6o}, respectively, which are all 0^o for practical purposes, and their standard deviations are 0.0035^o, 0.0036^o and 0.0014^o, respectively. The average lattice rotation for all three components is thus considered zero. The standard deviation of the two lattice rotation components Ω_1 and Ω_2 is more than twice that of the lattice rotation component Ω_3. The full width at half maximum (FWHM) for the three components is 0.0082^o, 0.0085^o and 0.0033^o, respectively. These statistics indicate that the lattice rotation components Ω_1, Ω_2, and Ω_3 are in general different, and such differences might depend upon the initial dislocation density and its evolution, but definitely upon loading direction.

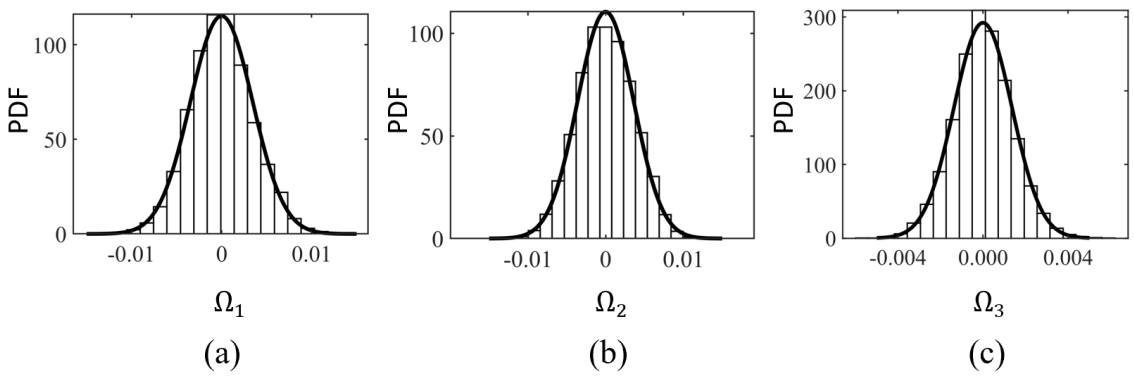

Fig. 3.15. Probability distribution function of the three lattice rotation components in (°) at 0.6% strain. The panels (a), (b) and (c) display the probability distribution functions of Ω_1, Ω_2 and Ω_3, respectively. Gaussian curves (red) are fit onto the raw data of the individual lattice rotation component distributions based on maximum likelihood estimation (MLE) using MATLAB software.

3.7 Discussion

The results discussed in the previous sections have showcased the significance of the concept of virtual dislocation density; namely that, the introduction of the virtual density enabled us to solve the dislocation density evolution equation on each slip system individually as opposed to solving them in a coupled fashion. Achieving decoupling of the density evolution equations during the numerical solution was also enabled by the use of the operator splitting scheme in solving the transport and the reaction parts, while treating the virtual density in the divergence constraint in a semi-implicit fashion. It is important to note that solving the density evolution equation numerically in the decoupled formulation offers three advantages. The first is lowering the computational cost to solve the linear system of equations for slip system activity individually in comparison to solving all slip systems together. The second is the control of the accuracy of the solution and suppressing the spurious errors arising from the coupled divergence constraint. The third is that keeping track of the density of the dislocations involved in reactions via the virtual density on every slip system makes it possible to model processes like unzipping of sessile dislocation junctions, a possible future extension of the current work.

The reader must be alerted to the fact that the current work is but a step toward completing the CDD framework. Until that point is reached, the comparison of CDD results with DDD results for the same simulation conditions will always show some differences. As far as bulk simulations are concerned, such differences in results can be explained in terms of the physics built into the

two types of models. One major difference between the two sets of simulations is the lack of glissile junction mechanism in the simulations based upon the microMegas DDD model used here (Devincre et al., 2011). The incorporation of glissile junction reactions to CDD equations couples the density evolution of multiple slip systems together. Consequently, the dislocation density increase in a slip system no longer solely depends only on the plastic slip happening in the slip system but rather on the activity of the reacting systems as well. It is evident from Fig. 3.9(a) that dislocation density increase within inactive slip systems is due to glissile junction reactions – a mechanism that contradicts the classical interpretation of dislocation storage during plastic deformation, which suggests that the dislocation storage on a given slip system is mainly due to the slip activity within that slip system. The dislocation density in active slip systems increases with the applied strain thus increasing the possibility of glissile junction reactions with dislocations within the inactive systems. This results in the steady increase in dislocation density of inactive slip systems as observed in Fig. 3.9(a). On the other hand, due to the lack of glissile junction mechanism, there is no increase in the density of inactive slip systems in the DDD simulation as can be seen from Fig. 3.9(b). Although the cross-slip mechanism also aids in transferring slip activity and hence dislocations between slip systems, there is still no net increase in the dislocation density on the inactive slip systems in the DDD simulation conducted here because cross slip to the inactive slip systems is not operative.

Fig. 3.8(a) shows the stress-strain curves of CDD and DDD simulation. The CDD stress-strain curves have a slightly higher yield point and lower hardening rate compared to the DDD simulation. The yield point is sensitive to the initial dislocation configuration, and the CDD and DDD yield points can be calibrated to coincide with one another. However, the difference in the hardening rate can be attributed to the absence of an explicit representation of sessile junction formation mechanism in the current CDD simulations. The incorporation of sessile junctions will reduce the gliding dislocation density and therefore increase the hardening rate. Sessile junctions were not implemented in the current simulations due to the lack of a procedure for unzipping such junctions. Another possibility for the lower hardening rate obtained in the CDD simulation is the use of the decay function $f\left(\rho^i, \rho^f\right)$ in the Taylor hardening formula (see equations (3.51) and (3.52)). As discussed earlier, this function was used to emulate the destruction of sessile junctions and prevent indefinite accumulation of dislocations against each other in regions of high dislocation density, by choosing it to be a smoothly decaying step function in the density. Currently,

there is no quantitative basis at this point to calibrate such function. Instead, its impact on the results was checked by varying the parameters a and b used in that function to correspond to the CDD1 and CDD2 simulations. The results in Fig. 3.8(a) show that the simulation with slower rate of decay (CDD1) has higher yield point compared to the simulation with faster rate of decay (CDD2). Consequently, the difference in flow stress also affects the dislocation density evolution between the two sets of simulations as can be seen from Fig. 3.8(b). In all cases, the breakaway of dislocations upon reaching the decay threshold is of course expected to lead to rapid dislocation motion and possible over-annihilation. This is perhaps the reason the dislocation density in the CDD case rises at a slower rate than in the DDD counterpart, and hence the lower hardening rate in the case of CDD.

Ideally speaking, the Taylor hardening term should be replaced with a proper implementation of the correlation stress in 3D, and the hard junctions should be explicitly implemented. Two-dimensional CDD models showed that the correlation leads to multiple resistive stresses, some of which are Taylor-like (Groma et al., 2016; Wu et al., 2018). Preliminary results on the dislocation-dislocation correlation in 3D have been recently obtained (Anderson and El-Azab, 2020) and its implementation in CDD is underway.

3.8 Summary and conclusions

A novel formulation to incorporate dislocation reactions into vector density-based CDD models was proposed using the concept of virtual dislocation density. The latter was introduced to keep track of the dislocations involved in dislocation networks among various slip systems via cross-slip and junction reactions. Using the virtual density on each slip system as a complement to the glide density, it was easily possible to decouple the numerical solution of the transport-reaction equations of the dislocation density on all slip systems, thus expediting the solution and controlling the numerical errors associated with the enforcement of the divergence constraint. This new formulation was implemented based on the operator splitting approach, where the dislocation transport equation was solved first using the least-squares approach, with the divergence constraint implemented in a semi-implicit fashion.

The effectiveness of the new formulation was studied using a number of test cases. The results showed that the new formulation was able to enforce the dislocation continuity rigorously by preventing the accumulation of spurious dislocation densities observed in the coupled

formulation. The significance of this was further emphasized by showing how the numerical errors snowballed as the simulation progresses through the dislocation density evolution graphs. The new formulation was then used to study the behavior of FCC crystals under monotonic loading. The stress-strain curves obtained from the simulations exhibited similar behavior as those obtained by DDD simulations, with some differences explained in terms of the different physics contained in the CDD and DDD simulations. As expected, the microstructural features obtained from the simulation results showed high density features along the $< 110 >$ type directions. Analysis of the virtual dislocation density microstructure revealed that the dislocation reactions played an important role in the generation of these microstructural features. Lattice rotation results revealed clearly the subgrain structure associated with the dislocation patterns obtained from the solution. The probability distribution functions of the lattice rotation components were also shown to agree with the DDD simulations results reported in (Mohamed et al., 2015).

This virtual density approach can be considered as a step forward in enabling the CDD approach to accurately capture the dislocation microstructure. Further improvements of this approach by explicitly incorporating sessile junction formation and removing the phenomenological Taylor hardening part of the model is in progress. In this case, the density information captured by the virtual dislocation density can be used to account for the unzipping of sessile junctions based on the local stress state. Furthermore, incorporating the information about dislocation correlations can help in improving the accuracy of the dislocation density transfer during the dislocation reaction process.

4. STATISTICAL ANALYSIS OF INTERNAL STRESS FLUCTUATIONS

A portion of this chapter has been published in Modelling and Simulation in Materials Science and Engineering by Vignesh Vivekanandan, Joseph Pierre Anderson, Yash Pachaury, Mamdouh S Mohamed and Anter El-Azab as "Statistics of internal stress fluctuations in dislocated crystals and relevance to density-based dislocation dynamics models", 30, 045007. https://doi.org/10.1088/1361-651X/ac5dcf

4.1 Abstract

A statistical analysis of internal stress fluctuations, defined as the difference between the local mean stress and stress on dislocations, is presented for deforming crystals with 3D discrete dislocation systems. Dislocation realizations are generated using dislocation dynamics simulations and the associated stress field is computed as a superposition of a regularized stress field of dislocation lines within the domain of the solution and a complementary stress field computed via a finite-element boundary value problem. The internal stress fluctuations of interest are defined by an ensemble of the difference between the stress on dislocation lines and the local mean field stress in the crystal. The latter is established in a piecewise fashion over small voxels in the crystal thus allowing the difference between the local average stress and stress on segments to be easily estimated. The results show that the Schmid stress (resolved shear stress) and Escaig stress fluctuations on various slip systems sampled over a random set of points follow a Cauchy (Lorentz) distribution at all strain levels, with the amplitude and width of the distribution being dependent on the strain. The implications of the Schmid and Escaig internal stress fluctuations are discussed from the points of view of dislocation cross-slip and the dislocation motion in continuum dislocation dynamics.

4.2 Introduction

Dislocations in deforming crystals are known to form self-organized structures that emerge due to complex interactions between dislocations. At the length scales relevant to these structures, the statistical nature of the internal crystal stress plays an important role in pattern emergence (Mughrabi, 1983; Ungar et al., 1984). Over the years, many dislocation-based models were developed to understand the self-organization of dislocation in deformed crystals, including both

discrete and density-based (continuum) dislocation dynamics models. In discrete dislocation dynamics simulations, the motion and interactions of individual dislocations are explicitly considered (Arsenlis et al., 2007; Devincre et al., 2001; Po et al., 2014; Stricker et al., 2018; Weygand et al., 2002). Preserving the details about individual dislocations at a fine scale enables these models to deterministically describe the heterogeneous nature of the internal stress field in a crystal. Continuum dislocation dynamics models on the other hand do not consider the individual dislocations explicitly; they rather capture the dynamics of the dislocation system through coarse-grained representations of dislocation lines (Acharya, 2001; Hochrainer et al., 2007; (Lin et al., 2021); Lin and El-Azab, 2020; Vivekanandan et al., 2021; Xia and El-Azab, 2015). The main advantage of the latter models is that they can be used to simulate the deformation of larger volumes up to higher strain levels. However, since the continuum models inherently lack the spatial information of the individual dislocation segments and networks, care must be taken to recapture the information lost as much as possible into these models, especially those pertaining to the statistical nature of the internal stress. The purpose of the current work is to shed some light on the statistical character of stress of three-dimensional (3D) dislocation systems and provide an insight as to how the information lost in the coarse-graining process might be recovered and used in continuum dislocation dynamics.

Some early dislocation-based models (Mughrabi, 2001, 1987; Mughrabi et al., 1986) set out to capture the distribution of internal stress within the dislocation wall structure of persistent slip bands using a phenomenological treatment, where it was assumed that the dislocation structure consists of dislocation rich and dislocation poor regions. Models based on reaction-diffusion type equations were also developed with the aim to capture the inhomogeneous distribution of dislocations (Aifantis, 1986; Walgraef and Aifantis, 1985). Efforts to incorporate the fluctuation of internal stresses and strains explicitly in the governing equation of the overall dislocation density were undertaken in the stochastic model proposed in (Hähner, 1996a, 1996b). The latter models clearly showed the effect of stress fluctuation on the dislocation cell formation. The models mentioned above while having some merit in connection with their intended applications, are not suitable to capture the evolution of dislocation density in 3D.

The classes of continuum dislocation models developed in a field-theoretic fashion are of relevance in the context of the current work. Earlier attempts to develop such models originate in the classical works of Nye (Nye, 1953) and Kröner(Kröner, 1959) , where a continuum dislocation

representation is given in terms of the plastic distortion gradients in crystals. In these works, the incompatibility of the plastic distortion fields in the crystal were captured in terms of dislocation density tensor using which the internal stress can be found. Benefiting from these works and those of Mura (Mura, 1963) and Kosevich (Kosevich, 1965), a framework known as phenomenological mesoscopic field dislocation mechanics (PMFDM) (Acharya and Roy, 2006; Roy and Acharya, 2006) was developed by space-time averaging the equations of field dislocation mechanics (Acharya, 2003, 2001), which captured the dislocation motion in terms of dislocation density tensor along with phenomenological closure equations. To retain the information about underlying distribution of dislocations, another class of continuum models known as the higher-dimensional dislocation continuum dislocation (hdCDD) were developed in which the dislocation density distribution is defined in a composite real plus line-orientation space (Hochrainer et al., 2007; Sandfeld et al., 2010). Describing the density in this higher dimensional space provided sufficient information to determine the plastic strain rate evolution and kinematic closure without using phenomenological arguments. The hdCDD theory was simplified to incorporate only spatial densities using the concept of alignment tensors (Hochrainer, 2015). A fourth class of models based upon a vector density representation of dislocations (Lin et al., 2021); Lin and El-Azab, 2020; Vivekanandan et al., 2021; Xia et al., 2016; Xia and El-Azab, 2015) was also developed. The resolution at which this model operates is such that the physical cancellation of oppositely oriented dislocations of the same Burgers vector coincides with the geometric cancellation inherent in the use of the vector representation of the density. The model is thus based on the premise that, for a given slip system, the vector density is defined such that it has a single line direction at every point in space, an approximation known as the line bundle approximation. Its important advantage is that it helps to establish a one to one correspondence with the underlying discrete dislocation system, and to account for processes like cross slip and junction reactions in a natural fashion (Lin and El-Azab, 2020; Vivekanandan et al., 2021). The dislocation density evolution equation is closed by determining the velocity in terms of local Peach-Kohler force fixed by a single line direction at each point in space. Typical results from that model can be found in (Lin et al., 2021); Lin and El-Azab, 2020; Vivekanandan et al., 2021; Xia et al., 2016; Xia and El-Azab, 2015). Although this model preserves the information about heterogeneous nature of dislocation system better compared to other continuum models, it still lacks the statistical information regarding the internal stress fluctuations. The self-consistent stress obtained by solving the associated eigenstrain

problem (Vivekanandan et al., 2021) does not capture such fluctuations since the dislocation system is coarse-grained. In passing, it is important to mention some additional statistical continuum dislocation dynamics models that proposed to restore the lost internal stress fluctuations by using the dislocation correlation (Groma, 1997; El-Azab, 2000a; Zaiser et al., 2001; Groma et al., 2003; Yefimov et al., 2004; Deng and El-Azab, 2007, 2009). However, this was only done in simple 2D edge-on dislocation configurations (Groma et al., 2003; Zaiser et al., 2001).

The works reported in (Csikor and Groma, 2004; Groma and Bakó, 1998; Ispánovity and Groma, 2008) are of direct relevance to the current work for they include an analysis of the internal shear stresses of straight parallel dislocation arrangements in terms of probability density functions (PDF). Under zero external stress, it was shown that the asymptotic behavior of the PDF of stress is only dependent on the local dislocation density, and it decays with the inverse third power of the stress (Groma and Bakó, 1998). It was also shown that the central part of the PDF is Gaussian and Cauchy for homogeneous and uncorrelated systems of straight infinite edge dislocations and dipolar configurations, respectively (Csikor and Groma, 2004). Both the central and asymptotic parts of stress distribution are shown to be affected by the external shear stress (Ispánovity and Groma, 2008); the central part becomes asymmetric and shifted by an amount proportional to the applied stress, and the asymptotic part becomes dependent on an extra term that decays with inverse forth power of stress. In a related work, an analytical expression of pair correlation of internal stress was proposed in (Zaiser and Seeger, 2002) in which the stress fluctuation is directly connected to the dislocation density fluctuation. The above results are attractive not only since they can speed up the dislocation dynamics simulation, as was demonstrated in (Bakó and Groma, 1999), but also because they represent an important part of any statistical dislocation dynamics models (Groma et al., 2003; Zaiser et al., 2001). However, the analytical PDF forms developed in (Csikor and Groma, 2004; Groma and Bakó, 1998; Ispánovity and Groma, 2008) are based on dislocation systems consisting of parallel straight dislocations with 2D stress fields. Recently, an attempt was made to characterize the dislocation correlation in 3D dislocation systems (Anderson and El-Azab, 2021). It was shown that the self-correlation functions weakly depend on plastic strain and are dependent on the length-scale used to treat the continuum density field.

The outline of the present work is as follows. First, a framework for considering deviations from the local mean-field stress, as well as a Monte-Carlo approach for evaluating probability distributions for local stress deviations is outlined. Subsequently, the solution of the discrete

dislocation mechanics used to evaluate the stress fields arising from discrete dislocation configurations is discussed. The resulting probability distributions are presented for deviations in local resolved shear stress and Escaig stress, and their dependence on system state is shown. Lastly, the implications of these stress fluctuations with respect to vector continuum dislocation dynamics models, especially the implementation of cross slip, is discussed.

4.3 Statistical characterization of internal stress fluctuations

To begin to discuss stress fluctuations, we must first have a firm grasp on the definition of the system at the lowest level of description, namely that of the underlying dislocations. Let us begin with some 3D crystal space $\mathcal{M}$ in which there are embedded 12 line objects (1-manifolds) $\mathcal{L}^{[\alpha]}$. These line objects represent all dislocations in the system of a given species, the distinguishing feature of which is their slip system represented by $\alpha = 1,2,\dots,12$; with 12 being the number of primary slip system in a face-centered cubic (FCC) crystal, which we adopt in this work. These line manifolds are equivalent to two natural measures of sets in the crystal. The first is the traditional volume measure which is defined in some region of the crystal $\Omega \subseteq \mathcal{M}$ as

$$|\Omega| = \int_{\Omega} d^3\boldsymbol{r}. \tag{4.1}$$

More nuanced volume averages could be conceived, but for the purposes of this work, this trivial volume average will suffice. Additionally, the same region is now also associated with a line measure for each species of line in the system

$$\left|\mathcal{L}^{[\alpha]} \cap \Omega\right| = \int_{\mathcal{L}^{[\alpha]}\cap\Omega} dl, \tag{4.2}$$

where dl is the scalar length element along the dislocation lines contained in Ω. An alternative formulation as a volume integral gives us a definition of the line integral as the integration against a discrete density field, $\varrho^{[\alpha]}$, as given below

$$\left|\mathcal{L}^{[\alpha]} \cap \Omega\right| = \int_{\Omega} \varrho^{[\alpha]}(\boldsymbol{r})\, d^3\boldsymbol{r}\,. \tag{4.3}$$

Any field in the crystal has two averages which correspond to the above measures. First the volume average of a field $f(\boldsymbol{r})$, which we will denote by square brackets:

$$[f(\boldsymbol{r})]_{\Omega} = \frac{1}{|\Omega|}\int_{\Omega} f(\boldsymbol{r}) d^3\boldsymbol{r}. \tag{4.4}$$

A second is the average value that the field takes on the dislocation lines of a given slip system in each volume, which we will denote by angle brackets:

$$\langle f(\boldsymbol{r})\rangle_{\Omega,\alpha} = \frac{1}{|\mathcal{L}^{[\alpha]} \cap \Omega|}\int_{\Omega} f(\boldsymbol{r})\, \varrho^{[\alpha]}(\boldsymbol{r})\, d^3\boldsymbol{r}. \tag{4.5}$$

Why might we care about these two averages? They each become interesting when one considers classes of volumes associated with a given spatial point. For our present purposes, we will consider the following field of volumes:

$$\Omega_{\boldsymbol{r}}^{(d)} = \left\{\boldsymbol{r}' \in \mathcal{M} : r_i' - r_i \in [0, d) \text{ for } i = 1,2,3\right\} \tag{4.6}$$

In this case, for some field $f(\boldsymbol{r})$ which is a functional of the dislocation configuration, i.e., which can be expressed as a line integral of the form $f(\boldsymbol{r}) = \int_{\mathcal{L}^{[\alpha]}} \hat{f}(\boldsymbol{r} - \boldsymbol{r}')dl$, the volume average of this field with respect to our collection $[f(\boldsymbol{r}')]_{\Omega_{\boldsymbol{r}}^{(d)}}$ will itself be a functional of the volume average of the dislocation configuration $\left[\varrho^{[\alpha]}(\boldsymbol{r}')\right]_{\Omega_{\boldsymbol{r}}^{(d)}}$. That is, if we wanted to describe our system with some coarse description of the underlying dislocation state, e.g., with a smoothly varying density field with bounded variation such as $\left[\varrho^{[\alpha]}(\boldsymbol{r}')\right]_{\Omega_{\boldsymbol{r}}^{(d)}}$, we would only be able to express the volume average of the field $f(\boldsymbol{r})$.

This coarse description of $f(\boldsymbol{r})$ would be useful if the behavior of the dislocations depended on the average behavior of a field in some region around the dislocations, but alas, this is not the case. The behavior of the dislocations is dependent on the values which fields take *on the dislocation line*. As a result, if some relationship (even a stochastic relationship) between the volume average of a field and the field value on the dislocation line exists, the behavior of the dislocation system can be recaptured from only the coarse description of the dislocation field.

The above considerations would be valid for many of the internal mechanical fields in dislocated crystals, e.g., the displacement, displacement gradient, strain, or stress fields. However, in the case of the present work, we are interested especially in the analysis of the stress field, as the stress field provides the driving force for glide transport as well as the energy barrier for dislocation cross slip. For the remainder of the work, we will analyze the difference in the stress on the dislocation line and the volume average stress, which we will refer to as the fluctuation stress or stress fluctuations:

$$\tilde{\sigma}_{ij}(\boldsymbol{r}) \coloneqq \sigma_{ij}(\boldsymbol{r}) - \left[\sigma_{ij}(\boldsymbol{r}')\right]_{\Omega_{\boldsymbol{r}}^{(d)}}. \tag{4.7}$$

Rather than consider the full stress tensor, we only consider the components that are relevant to the dislocation glide and cross slip kinetics, namely the Schmid and Escaig components. Specifically, Schmid stress $\sigma_{\boldsymbol{s}}^{[\boldsymbol{\alpha}]}$ is relevant to dislocation motion and cross slip while Escaig stress $\sigma_{\mathrm{e}}^{[\alpha]}$ is relevant to cross slip. Let the Burgers vector of a given slip system be $b\widehat{\boldsymbol{b}}^{[\alpha]}$, with b being its magnitude, the slip plane normal be $\widehat{\boldsymbol{n}}^{[\alpha]}$, and the direction of glide vector be $\widehat{\boldsymbol{d}}^{[\alpha]} = \widehat{\boldsymbol{n}}^{[\alpha]} \times \widehat{\boldsymbol{b}}^{[\alpha]}$. The Schmid and Escaig components are, respectively, expressed in the forms:

$$\sigma_{\mathrm{s}}^{[\alpha]} = \left(\left(\boldsymbol{\sigma}^{[\alpha]} \cdot \widehat{\boldsymbol{b}}^{[\alpha]}\right) \times \widehat{\boldsymbol{b}}^{[\alpha]}\right) \cdot \widehat{\boldsymbol{d}}^{[\alpha]} \tag{4.8}$$

$$\sigma_{\mathrm{e}}^{[\alpha]} = -\left(\left(\boldsymbol{\sigma}^{[\alpha]} \cdot \widehat{\boldsymbol{d}}^{[\alpha]}\right) \times \widehat{\boldsymbol{b}}^{[\alpha]}\right) \cdot \widehat{\boldsymbol{d}}^{[\alpha]} \tag{4.9}$$

Thus, the fluctuation stress corresponding to these stress components can be defined as

$$\tilde{\sigma}_{\mathrm{s}}^{[\alpha]}(\boldsymbol{r}) \coloneqq \sigma_{\mathrm{s}}^{[\alpha]}(\boldsymbol{r}) - \left[\sigma_{\mathrm{s}}^{[\alpha]}(\boldsymbol{r}')\right]_{\Omega_{\boldsymbol{r}}^{(d)}}, \tag{4.10}$$

$$\tilde{\sigma}_{\mathrm{e}}^{[\alpha]}(\boldsymbol{r}) \coloneqq \sigma_{\mathrm{e}}^{[\alpha]}(\boldsymbol{r}) - \left[\sigma_{\mathrm{e}}^{[\alpha]}(\boldsymbol{r}')\right]_{\Omega_{\boldsymbol{r}}^{(d)}}. \tag{4.11}$$

Again, the quantities in brackets are local average over the volume $\Omega_{\boldsymbol{r}}^{(d)}$ centered about $\boldsymbol{r}$. This spatial fields may depend on the spatial coordinate. However, for the present preliminary investigation, we consider only the statistical properties of this field across the entire crystal domain, considering $\tilde{\sigma}$ to be a random process with respect to the spatial coordinate. As a result, we will consider the PDF of the fluctuation stress over the crystal domain. In terms of our averaging process, the PDF is expressed rigorously by the spatial average of the following Dirac delta distribution:

$$p(s) \coloneqq \left[\delta\left(s - \tilde{\sigma}(\boldsymbol{r})\right)\right]_{\mathcal{M}} \tag{4.12}$$

In practice, it is expressed by the average of small window functions with unit norm. One possible interpretation of the PDF above is that if a point $\boldsymbol{r} \in \mathcal{M}$ is picked at random, the PDF represents the likelihood that the fluctuation stress at that point, $\tilde{\sigma}(\boldsymbol{r})$, falls in a small range around s.

4.4 A Monte Carlo scheme for evaluating stress fluctuations

Because the quantities considered are averages, they naturally lend themselves to Monte Carlo integration. That is, for a given volume Ω, we may pick N points from the volume, $\boldsymbol{r}_k \in \Omega$, and find that the empirical average of a given field $\boldsymbol{\sigma}(\boldsymbol{r}_k \in \Omega)$ approaches the volume average:

$$\lim_{N\to\infty} \frac{1}{N} \sum_{k=1}^{N} \boldsymbol{\sigma}(\boldsymbol{r}_k \in \Omega) \; = [\boldsymbol{\sigma}(\boldsymbol{r})]_{\Omega} \tag{4.13}$$

The evaluation scheme which we will use is as follows: begin with a collection $S = \{\boldsymbol{r}_k\}_{k=1}^{N_S}$ of sample points in the crystal and collections $\Lambda^{[\alpha]} = \{\boldsymbol{r}_k\}_{k=1}^{N_\alpha}$ of sample points on the dislocation lines of species α. Next, form a coarse partition of the crystal space by creating a cubic lattice of spacing d

$$K^{(d)} = \{\boldsymbol{R} \in \mathcal{M} : \boldsymbol{R} = d(h\,\boldsymbol{e_1} + k\,\boldsymbol{e_2} + l\,\boldsymbol{e_3}) \text{ for some } h, k, l \in \mathbb{Z}\}, \tag{4.14}$$

where $\boldsymbol{e}_i$ form an orthonormal basis. This partitions the crystal into voxels (volumes) given by $\Omega_{\boldsymbol{R}}^{(d)}$ for $\boldsymbol{R} \in K^{(d)}$ (for the definition of $\Omega_{\boldsymbol{R}}^{(d)}$ refer to equation (4.6)). For simplicity of notation, we will denote averages over these sets as:

$$[\boldsymbol{\sigma}(\boldsymbol{r})]_{\boldsymbol{R}} = \frac{1}{\left|S \cap \Omega_{\boldsymbol{R}}^{(d)}\right|} \sum_{S\cap\Omega_{\boldsymbol{R}}^{(d)}} \boldsymbol{\sigma}(\boldsymbol{r}_k) \tag{4.15}$$

Because we used a partition of the system, each discrete sample point $\boldsymbol{r}_k$ corresponds to only one lattice point $\boldsymbol{R}$. Let us represent this correspondence by $\boldsymbol{R} = \lfloor \boldsymbol{r}_k \rfloor$. For the rest of the work, the statistics sampled at crystal points and dislocation points will be represented by superscripts c and d respectively. Therefore, we can examine the statistics of the spread of crystal stresses and the stresses on dislocation line with respect to the crystal stress within each voxel $\Omega_{\boldsymbol{R}}^{(d)}$ as follows:

$$\tilde{\boldsymbol{\sigma}}^{\mathrm{c}}(\boldsymbol{r}_k) = \boldsymbol{\sigma}^{\mathrm{c}}(\boldsymbol{r}_k) - [\boldsymbol{\sigma}^{\mathrm{c}}]_{\lfloor \boldsymbol{r}_k \rfloor} \text{ for } \boldsymbol{r}_k \in S \tag{4.16}$$

$$\tilde{\boldsymbol{\sigma}}^{\mathrm{d}}(\boldsymbol{r}'_k) = \boldsymbol{\sigma}^{\mathrm{d}}(\boldsymbol{r}'_k) - [\boldsymbol{\sigma}^{\mathrm{c}}]_{\lfloor \boldsymbol{r}_k \rfloor} \text{ for } \boldsymbol{r}'_k \in \Lambda \text{ and } \boldsymbol{r}_k \in S \tag{4.17}$$

Examination of these deviations will allow an understanding of the typical spread of stress within one voxel in terms of crystal stress which is the quantity that is captured in the coarse-grained theories. As of now, current CDD models do not consider time coarse graining formally. However,

when time coarse graining is built into such models the fluctuations statistics collected in this work must also be coarse-grained in time.

It is important to note that the statistics of the stress fluctuation, $\tilde{\boldsymbol{\sigma}}^{\mathbf{c}}$, defined in this section is inherently different from the statistics of the stress $\boldsymbol{\sigma}^{\mathbf{c}}$ itself discussed in the works of (Csikor and Groma, 2004; Groma and Bakó, 1998; Ispánovity and Groma, 2008). Furthermore, establishing a relationship between the two is not straightforward since the mean stress in the voxel, $[\boldsymbol{\sigma}^{\mathbf{c}}]$, varies from one voxel to another. Further discussions on the difference between these two statistics can be found in appendix A.

4.5 The stress field of dislocations in a periodic domain

We note that the internal stress of dislocations is the sum of the singular dislocation stress and the image stresses, with the latter accounting for the contribution of dislocations outside the domain of calculations, considered here to be a representative volume element (RVE). The discrete dislocation dynamics schemes in the literature, e.g., in (A. Arsenlis et al., 2007; Devincre et al., 2001; Weygand et al., 2002), implement periodic boundary conditions with multipole or other schemes to compute the image stress. These approximate schemes are not suited for implementation in the current analysis. Hence, we present a formal statement of the elastic boundary value problem (BVP) of many-dislocation systems in bounded crystals for the periodic boundary case and solve it with finite element method (FEM) (Zienkiewicz et al., 2005).

Within the crystal RVE, the singular stress is computed as the sum of stress contributions by the set of segments representing the dislocation configuration using a regularized stress expression given in (Cai et al., 2006), with a core spreading radius of $5b$, where b is the magnitude of Burgers vector. This stress is denoted here by σ_{ij}^{∞}. As for the image stress, σ_{ij}^{I}, we use the conditions of statistical homogeneity (El-Azab, 2000b) to derive the corresponding BVP. Consider a bounded crystal RVE Ω with boundary $\partial\Omega$ embedded into an infinite crystal that contains a statistically homogeneous dislocation distribution and denote the (total) internal stress field in Ω by σ_{ij}. This stress can be expressed in the form

$$\sigma_{ij}(\boldsymbol{r}) = \sigma_{ij}^{\infty}(\boldsymbol{r}) + \sigma_{ij}^{\mathrm{I}}(\boldsymbol{r}) \quad \boldsymbol{r} \in \Omega. \tag{4.18}$$

As stated in an earlier work (Deng et al., 2008), the image stress field can be computed by solving the BVP stated below,

$$\begin{aligned} &\partial_j \sigma_{ij}^I + F_i = 0, \;\; F_i = \partial_k \sigma_{ik}^\infty \;\; \text{in } \Omega, \\ &n_j \sigma_{ij}^I = T_i, \qquad T_i = -n_k \sigma_{ik}^\infty \text{ on } \partial\Omega, \end{aligned} \tag{4.19}$$

where σ_{ik}^∞ is the infinite-domain stress of dislocations inside the RVE Ω, n_j is the normal to its boundary, and F_i and T_i are the body forces within Ω and the traction on $\partial\Omega$, respectively.

4.6 Simulations

An approach similar to that outlined in (Deng et al., 2008) for solving the BVP (19) is applied here to compute the image stress field of the dislocation configurations. The discrete dislocation dynamics simulation code microMegas (Devincre et al., 2001) was used to obtain dislocation configuration for internal stress calculations in a Cu crystal RVE with a size of 5-micron on the edge, and loaded at strain rate of $\dot{\varepsilon} = 20\ \mathrm{s}^{-1}$ in the [001] direction. Snapshots of the dislocation configuration are collected at different strain levels. For each dislocation configuration, the BVP is solved to obtain the internal stress within the crystal volume. The initial dislocation density was taken to be $1.5 \times 10^{12}\ \mathrm{m}^{-2}$, with an initial configuration of 12 rectangular dislocation loops, one on each of the 12 slip systems. To set up the BVP, snapshots of different dislocation configurations were extracted from the outputs of the discrete dislocation dynamics simulations and post-processed to determine segments intersecting the boundary. Those segments were then extended outside of the RVE box to generate the virtual dislocation segments while preserving the tangential continuity of the dislocations intersecting the boundary. An FEM solution to the BVP was then determined using tetrahedral elements with second order Lagrange shape functions. The closure of the virtual segments was achieved at a distance far away from the boundaries of the RVE (~$10000b$). It is worthwhile to note that stress contribution of the virtual segments was utilized only for determining the image stresses. It was also observed that these virtual segments do not change the statistics of the internal stress fluctuations. Hence, considering the arbitrariness in the different methodologies used for the generating virtual segments, such as pseudo-mirror generation (Weygand et al., 2002) and semi-infinite virtual segments (Deng et al., 2008), we neglected the long-range stress field contributions due to these virtual segments to the statistics within the RVE.

4.7 Results

With the internal stress field and dislocation arrangement in hand, we may now analyze the average stresses defined earlier. For an overview of the partition of the crystal into voxels $\Omega_{\boldsymbol{R}}^{(\boldsymbol{d})}$ of length d, and the definition of crystal and line points, see Fig. 4.1. The blue dots in the figure correspond to the crystal points which are the tetrahedral mesh points, and the red dots correspond to mid-points of the dislocation segments sampled during the calculations. A dislocation segment is considered to belong to a given voxel if the mid-point of the segment falls inside the voxel domain. Similarly, a crystal point is assumed to belong to a voxel if it lies inside that voxel.

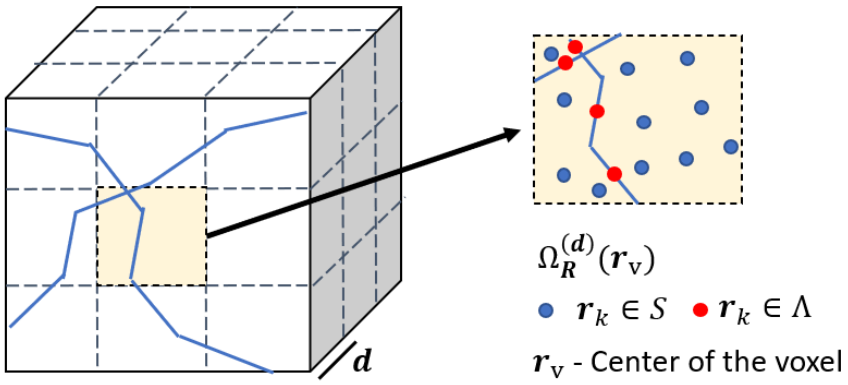

Fig. 4.1. Schematics showing the definition of voxels, crystal points (blue dots) and dislocation points (red dots).

To illustrate the importance of the current scheme, the Schmid stress statistics at the crystal points are analyzed first. Based on the definition in equation (4.16), the Schmid fluctuation stress on crystal points within every voxel volume $\Omega_{\boldsymbol{R}}^{(d)}$ for slip system α can be evaluated as follows:

$$\tilde{\sigma}^{\mathrm{c}[\alpha]}_{\mathrm{s}}(\boldsymbol{r}_k) = \sigma^{\mathrm{c}[\alpha]}_{\mathrm{s}}(\boldsymbol{r}_k) - \left[\sigma^{\mathrm{c}[\alpha]}_{\mathrm{s}}\right]_{\lfloor \boldsymbol{r}_k \rfloor} \text{ for } \boldsymbol{r}_k \in S \tag{4.20}$$

where $\left[\sigma^{\mathrm{c}[\alpha]}_{\mathrm{s}}\right]_{\lfloor \boldsymbol{r}_k \rfloor}$ denotes local mean Schmid stress for slip system α within the voxel, which is evaluated according to equation (4.15), and $\sigma_{\mathrm{s}}^{[\alpha]}(\boldsymbol{r}_k \in S)$ denotes the Schmid stress at a crystal point within the corresponding voxel.

The result of these calculations is shown spatially in Fig. 4.2(a); the Schmid stress fluctuation is shown for a partition of size $d = 300$ nm. The fluctuations in Schmid stress ranges from ± 10 MPa across the domain. The variation in the fluctuation statistics stems from the local

dislocation arrangement and the proximity of the crystal points to a dislocation segment. The closer the crystal point is to the dislocation the higher will be the stress and hence the fluctuation will be high. Fig. 4.2(b) shows the variation of Schmid stress fluctuation statistics at crystal points within a single voxel and 4.2(c) the dislocation arrangement within the corresponding voxel. The two figures illustrate clearly the dependence of fluctuation statistics on the proximity of the crystal points to the dislocation. The high positive stress fluctuation regions (red) lie close to the dislocation since the stress faced by these points from the dislocation is higher than the mean stress of the voxels. Similarly, the low negative stress fluctuation regions (blue) lie farther from the dislocation since the stress faced by these points from the dislocation is lower than the mean stress of the voxels.

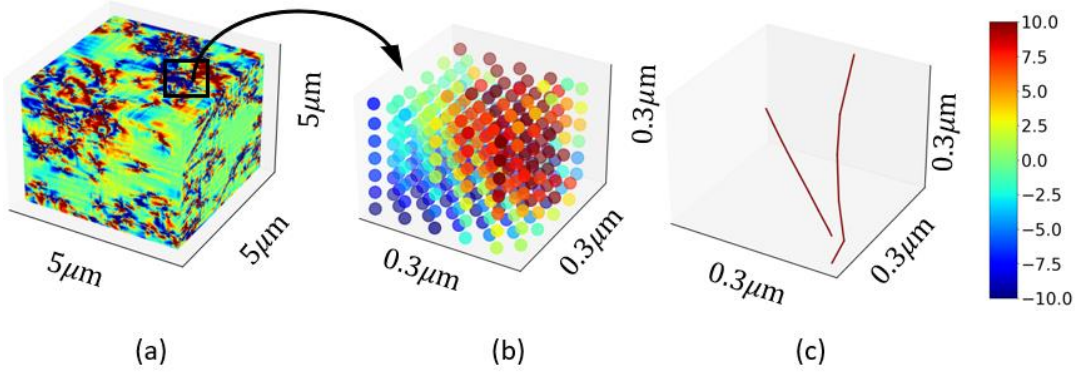

Fig. 4.2. Schmid stress fluctuations at crystal points in MPa. (a) the simulation domain, (b) crystal points within a single voxel and (c) dislocation arrangement within the same voxel. The figures demonstrate the variation of fluctuation stress within the voxel due to the local dislocation arrangement.

By the definition of the stress fluctuations, the statistics will vary vastly based on how the mean stress field is calculated. In this case, for a given dislocation configuration, the mean field statistics will vary based on the chosen voxel dimension. Hence, it becomes important to study the variation of the stress fluctuation statistics with respect to voxel size. Fig. 4.3 shows the Schmid stress fluctuation statistics at crystal points throughout the domain for different voxel dimensions for the same discrete configuration. It can be observed from the figure that the fluctuations in Schmid stress reduce as the voxel dimensions decreases. This behavior can be explained with the fact that the stress due to dislocations closer to the crystal points has a significantly strong effect

compared to dislocations away from it. Hence, averaging the stress over larger voxel sizes will result in larger fluctuations as can be seen in Fig. 4.3. This highlights the need for mean-field theories to incorporate information about the fluctuation statistics to get an accurate estimation of the local stress. For the remainder of the present work, we will utilize a voxel partition of d = 80 nm. Such voxel size is roughly twice the resolution used to solve the vector density continuum dislocation dynamics (Vivekanandan et al., 2021).

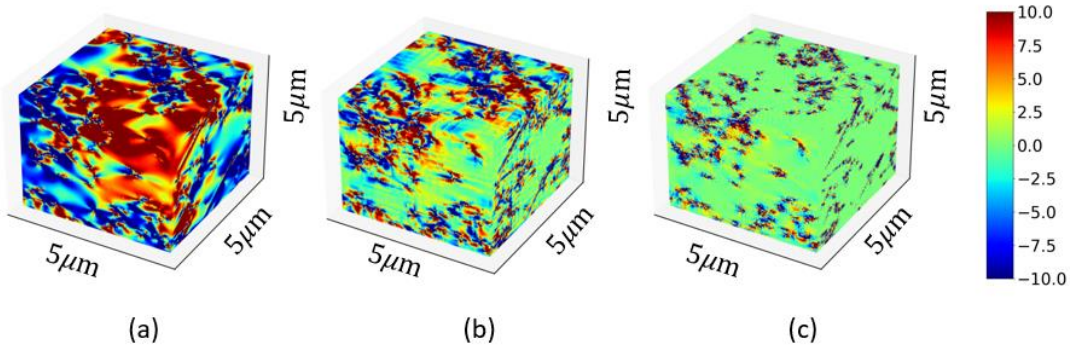

Fig. 4.3. Resolved shear stress fluctuations at crystal points in MPa for (a) d = 5 μm (the entire box), (b) d = 300 nm and (c) d = 80 nm. The three snapshots illustrate the dependence of fluctuation statistics on the voxel size.

As previously defined in equation (4.12), another way to characterize the fluctuations in stresses in mean field theories is casting the fluctuation statistics in the form of PDF. Fig. 4.4 shows the Schmid fluctuation stress and Escaig fluctuation stress on crystal points obtained from discrete dislocation dynamics casted as PDF for all 12 slip systems at 1% strain. It is observed that the fluctuation in Schmid stress and Escaig stress exhibit symmetric distributions with zero mean value for all slip systems, which is expected as the fluctuation is measured relatively to the mean of the points measured. Hence, the average of fluctuations throughout the domain can be expected to be zero. Fig. 4.5 shows the variation of the fluctuation statistics with strain on slip system 1 for both Schmid and Escaig stress. Although the distribution remains the same with a sharp peak at zero fluctuation stress, the amplitude of the peak reduces and width of the distribution at half maximum increases as the strain increases. This trend can be explained with the fact that more dislocation length is introduced in the system as the strain is increased, resulting in a higher probability for the crystal points to be closer to the dislocations resulting in large stresses.

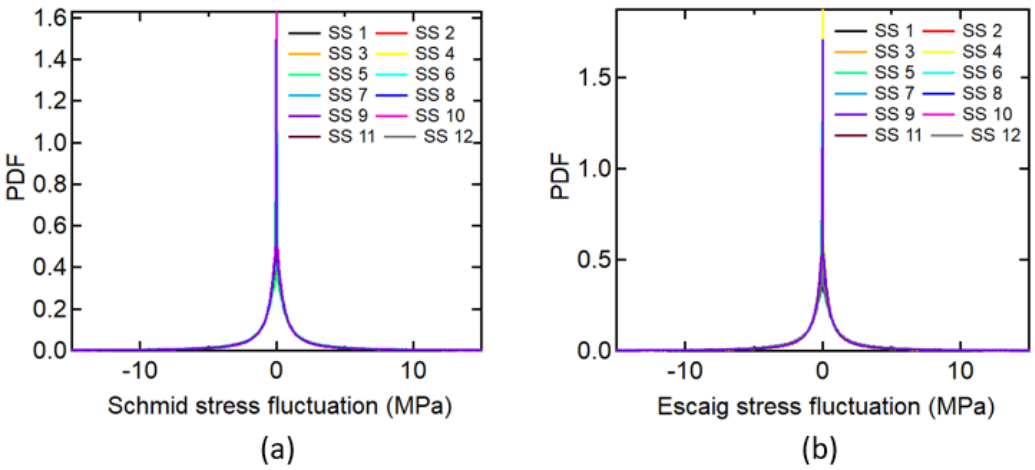

Fig. 4.4. Comparison of the PDF of (a) Schmid stress and (b) Escaig stress fluctuations on crystal points for all 12 slip systems at 1% strain.

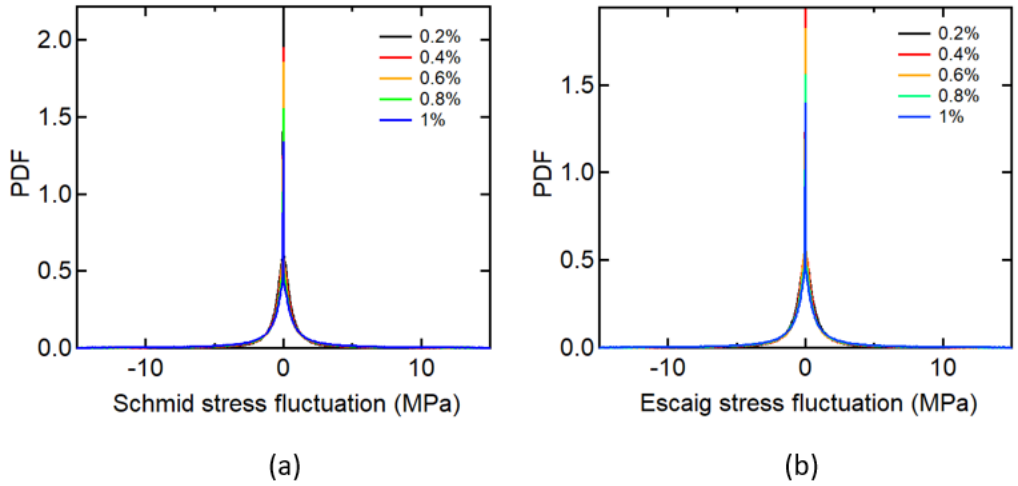

Fig. 4.5. Comparison of the PDF of (a) Schmid stress and (b) Escaig stress fluctuations on crystal points for slip system 1 at different strains.

In order to reveal the connection between the internal stress fluctuation and dislocation dynamics, we shift our focus to the fluctuation statistics on the dislocation segments rather on the crystal points since it is the stress on the dislocation segments themselves which influences the evolution of the dislocation system. This segment-based sampling is expected to yield distributions for the internal stress field that are different from those obtained for crystal points as the stress field is concentrated near the line segments. Such segment-based statistical sampling of internal stress fluctuation can be used to derive a density-based mobility law by connecting the segment-

based statistical properties of the Schmid stress fluctuation with the statistics of the segment velocity and as well as to characterize accurately the local stress on dislocations during cross-slip. In the context of developing a density-based approach for dislocation dynamics, the Schmid stress in the density-averaged mobility law must be compared to, and then connected with, the local average stress in the crystal, i.e., the mean stress field, as the latter is what can be computed from the eigenstress caused by a smoothly varying dislocation density field.

Thus, based on the definitions in the previous sections, the Schmid fluctuation stress and Escaig fluctuation stress within each voxel $\Omega_{\boldsymbol{R}}^{(d)}$ on dislocations belonging to slip system α can be calculated as follows

$$\tilde{\sigma}^{\mathrm{d}[\alpha]}_{\mathrm{s}}(\boldsymbol{r}'_k) = \sigma^{\mathrm{d}[\alpha]}_{\mathrm{s}}(\boldsymbol{r}'_k) - \left[\sigma^{\mathrm{c}[\alpha]}_{\mathrm{s}}\right]_{\lfloor \boldsymbol{r}_k \rfloor} \text{ for } \boldsymbol{r}'_k \in \Lambda \text{ and } \boldsymbol{r}_k \in S. \tag{4.21}$$

$$\tilde{\sigma}^{\mathrm{d}[\alpha]}_{\mathrm{e}}(\boldsymbol{r}'_k) = \sigma^{\mathrm{d}[\alpha]}_{\mathrm{e}}(\boldsymbol{r}'_k) - \left[\sigma^{\mathrm{c}[\alpha]}_{\mathrm{e}}\right]_{\lfloor \boldsymbol{r}_k \rfloor} \text{ for } \boldsymbol{r}'_k \in \Lambda \text{ and } \boldsymbol{r}_k \in S. \tag{4.22}$$

The PDF of the Escaig and Schmid stress fluctuations sampled over the dislocation-points across different voxels in the simulation domain is shown in Fig. 4.6. Note that the statistics of dislocations belonging to all slip systems are grouped together in this case. The fluctuation statistics obtained from discrete dislocation dynamics were then curve fitted using a Cauchy distribution function of the form $f(x: x_0, A, w) = \frac{2A}{\pi}\left(\frac{w}{4(x-x_0)^2+w^2}\right)$ where x_0 is the center of the distribution, A is a parameter related to the maximum amplitude and w is the full width at the half maximum. At similar strain level, the PDF of the fluctuation stress field calculated at dislocation points is wider and has lower peak in comparison to that calculated at crystal points. In addition to that, the peak at zero observed in the case of crystal points is not seen in the case of dislocation points. A careful investigation of the PDF in Fig. 4.6 also shows that the peak of the distribution is shifted from zero. This implies that the volume average of the internal stress fluctuations calculated on dislocation lines may have nonzero average value over the entire dislocation population. This can be better demonstrated by calculating the average values of the internal stress fluctuations for both sets of sampling points.

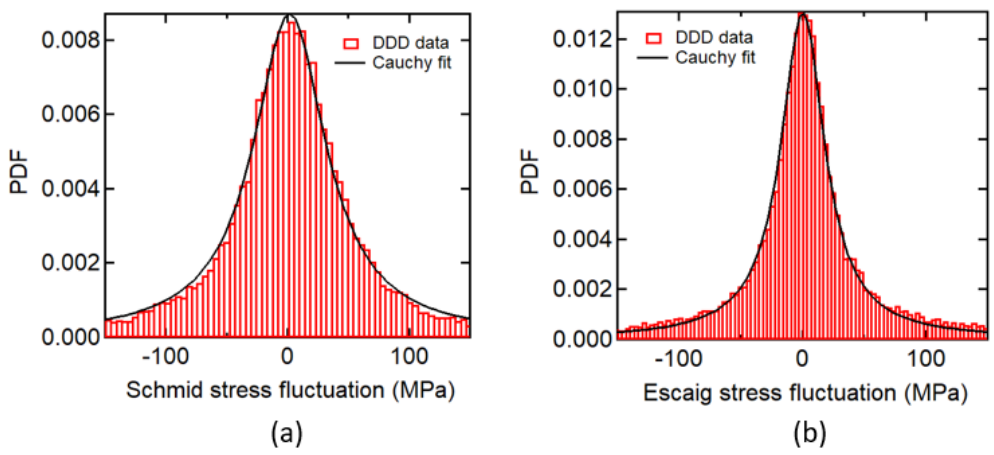

Fig. 4.6. PDF of (a) Schmid stress fluctuation and (b) Escaig stress fluctuation on dislocation points. The statistics of both Schmid and Escaig stress fluctuations follow Cauchy distribution.

Table 4.1 shows the Schmid fluctuation stress at dislocation points have non-zero mean value whereas the crystal points have zero mean value at different strain levels. During plastic deformation, dislocations tend to form patterns of dislocation-rich zones and dislocation-poor zones. In the case of crystal points, the sampled points fall randomly in both dislocation rich zones and dislocation poor zones. However, in the case of dislocation points, all sampled points are on the dislocation rich regions, resulting in higher stress levels at those points. Hence, having lower peak for the PDF of the internal stress field fluctuations calculated on dislocation-points can be attributed to local dislocation arrangements in the simulation domain.

Table 4.1. Mean of Schmid stress fluctuations over the simulation domain on the dislocations and in the crystal.

Strain (%)	Mean dislocation Schmid stress (MPa)	Mean crystal Schmid stress (MPa)
0.2	-6.65	1e-18
0.4	2.69	1e-17
0.6	-2.30	2e-18
0.8	-6.25	2e-18
1.0	-7.95	1e-17

Having shown that the stress fluctuations at segment points are indeed higher compared to crystal points, it is important to sample the stress fluctuations at segment points in accordance with the length of each dislocation segment to understand whether the length of the dislocation segment affects the statistics. Previously, the stress fluctuations were estimated only at the mid-point of the segment irrespective of the length of the dislocation segment based on equation (4.21) and (4.22). For comparison, the stress statistics are now sampled at multiple points along the dislocation segment such that the distance between two points is 0.1 times Burgers vector length, ensuring that statistics are representative of the dislocation length of individual segments. Fig. 4.7 shows the PDF of the fitted curves for Schmid stress and Escaig stress fluctuations at 1% strain for the single point and multiple points cases. It is evident from the figure that the fluctuation statistics do not vary significantly when a greater number of points are sampled along each segment compared to the case where the statistics are only sampled at midpoint. Hence, we can conclude that, for practical purposes, sampling the stress fluctuation statistics at the midpoint is adequate.

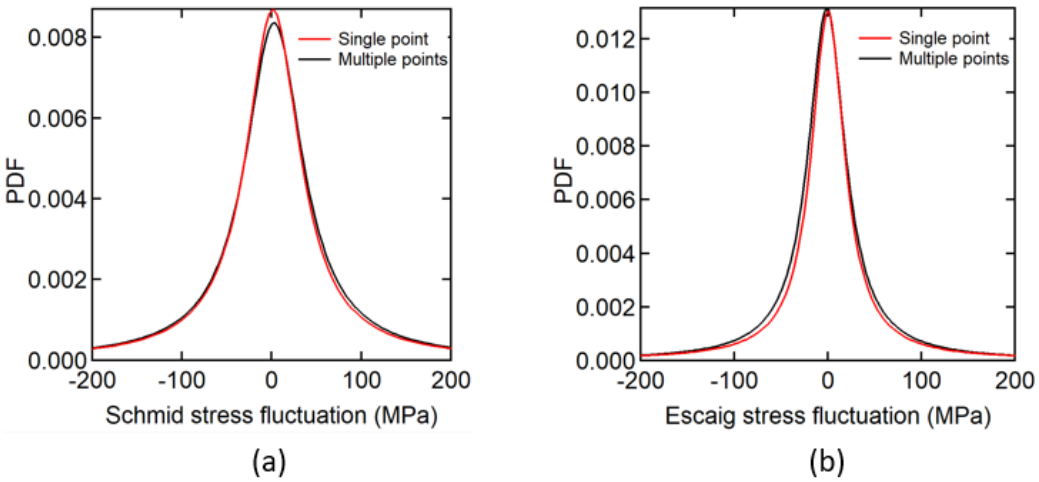

Fig. 4.7. Comparison of the PDF of (a) Schmid stress and (b) Escaig stress fluctuation statistics sampled at single point on a dislocation and multiple points in accordance with length of the dislocation segment. For practical purposes, the figure shows that sampling the stress fluctuation statistics at the midpoint is adequate.

It is important to understand whether the Schmid factor has an impact on the fluctuation statistics. As mentioned earlier, the discrete dislocation dynamics simulations leading to the current results were carried out under [001] loading. For this loading, 8 slip systems have equal Schmid factor, modulo a sign, and 4 slip systems have zero Schmid factors. These two groups of

slip systems are called here the active and inactive slip systems, respectively. The fluctuation statistics are thus decoupled into two subsets based on their Schmid factor within each voxel $\Omega_{\boldsymbol{R}}^{(d)}$ according to equation (4.21) and (4.22). The statistics on dislocation segments that lie on active slip systems and inactive slip systems are summed over the respective systems and the corresponding PDFs are displayed in Fig. 4.8. It is evident from the figure that the two subsets also follow a Cauchy distribution. Furthermore, the fluctuation statistics of the inactive slip systems are slightly different compared to that of the active slip systems, but this could be within the range of sampling error. Generally, the density of dislocations on the inactive slip systems is much lower that their active counterpart, and hence the sample size is smaller for the inactive slip systems.

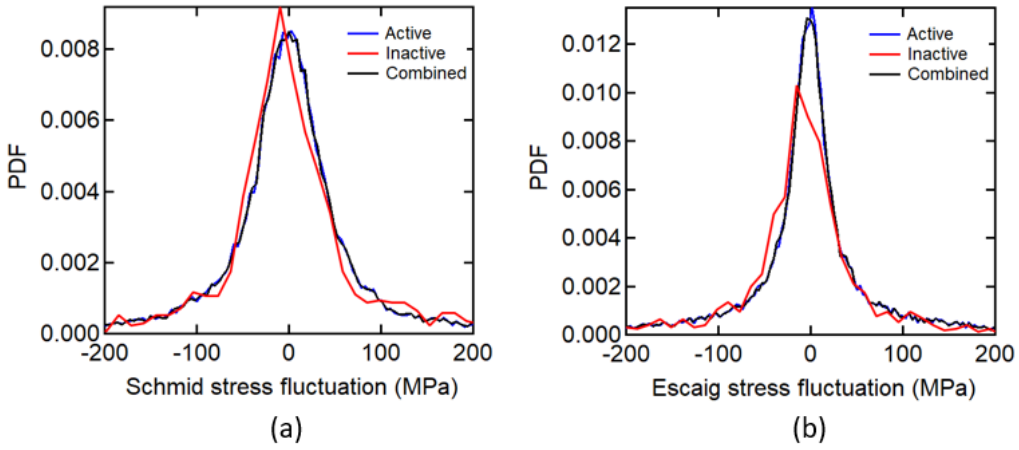

Fig. 4.8. Comparison of the PDF of (a) Schmid stress and (b) Escaig stress fluctuation statistics on active, inactive and all (combined) dislocation segments.

The impact of applied strain on the fluctuation statistics was studied by sampling dislocation configurations at different strain values. The stress fluctuation statistics for Escaig stress and Schmid stress at all strains were found to follow the Cauchy distribution. Fig. 4.9 shows the variation of the PDFs of fitted curves for Schmid stress and Escaig stress fluctuations with strain. It is evident from the figure that the peak of the distribution decreases as the strain increases. This trend can be explained with the fact that the more dislocation rich regions can be observed with increase in strain resulting in higher deviation from mean stress. Stated differently, the result is consistent with the fact that the fraction of points with high stress increases as more dislocation length is introduced during deformation.

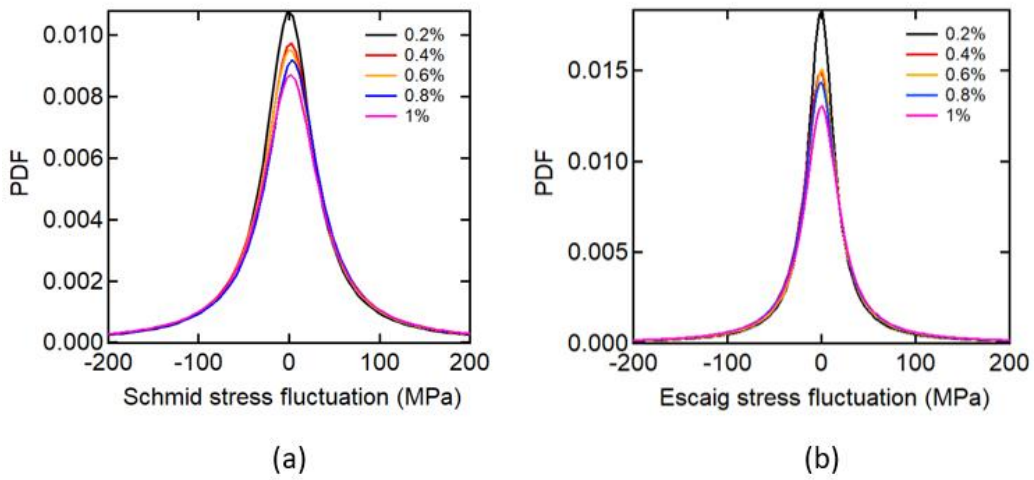

Fig. 4.9. PDF of (a) Schmid stress fluctuation and (b) Escaig stress fluctuation on dislocation points at different strain levels.

Alternatively, one can also characterize these stress fluctuations by scaling them with respect to the local mean stress of the voxel. The scaled Schmid and Escaig stress fluctuations within each voxel $\Omega_{\boldsymbol{R}}^{(d)}$ on a dislocation belonging to slip system α can then be defined as

$$\hat{\sigma}^{\mathrm{d}}{}_{\mathrm{s}}^{[\alpha]}(\boldsymbol{r}'_k) = \frac{\sigma^{\mathrm{d}}{}_{\mathrm{s}}^{[\alpha]}(\boldsymbol{r}'_k)}{\left[\sigma^{\mathrm{c}}{}_{\mathrm{s}}^{[\alpha]}\right]_{\lfloor \boldsymbol{r}_k \rfloor}} - 1 \text{ for } \boldsymbol{r}'_k \in \Lambda \text{ and } \boldsymbol{r}_k \in S. \tag{4.23}$$

$$\hat{\sigma}^{\mathrm{d}}{}_{\mathrm{e}}^{[\alpha]}(\boldsymbol{r}'_k) = \frac{\sigma^{\mathrm{d}}{}_{\mathrm{e}}^{[\alpha]}(\boldsymbol{r}'_k)}{\left[\sigma^{\mathrm{c}}{}_{\mathrm{e}}^{[\alpha]}\right]_{\lfloor \boldsymbol{r}_k \rfloor}} - 1 \text{ for } \boldsymbol{r}'_k \in \Lambda \text{ and } \boldsymbol{r}_k \in S. \tag{4.24}$$

Note that the scaling factor, which is the local mean voxel stress, is different at different voxel locations. Unlike non-scaled fluctuation statistics which are absolute values, the scaled statistics are expressed as fraction of the local mean voxel stress which varies based on the local dislocation arrangement at each voxel location. Thus, sampling values from the scaled statistics will enable us to make correction to the stress relative to the mean value. The PDF of the scaled Schmid stress and Escaig stress fluctuations are shown in Fig. 4.10. Interestingly, the scaled statistics also follows the Cauchy distribution. The functional form of the Cauchy curve used to fit the scaled statistics is same as the one used in Fig. 4.6. The PDF of the scaled stress fluctuations has its peak centered around -1 and the width of the distribution ranges from -5 to 5. This indicates that the actual stress faced by dislocation segment is markedly different from the local mean stress. Hence, it is vital for

mean field theories to incorporate this statistical information to characterize the local stress accurately.

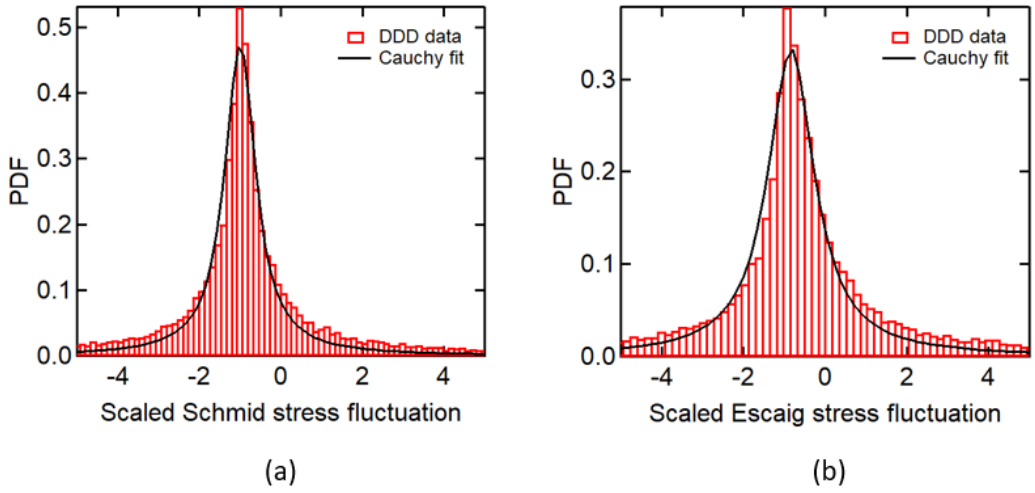

Fig. 4.10. PDF of scaled (a) Schmid and (b) Escaig stress on dislocation points fit to a Cauchy curve.

The above results are all that can be obtained regarding the Schmid and Escaig stress fluctuations in dislocation dynamics. It is important to note that the fluctuation statistics discussed in this work is applicable only for the [001] loading case. For the [001] loading case, the results seem to indicate that the PDFs are independent of the Schmid factor, but this remains to be verified for other loading conditions. Although the methodology discussed to obtain the fluctuation statistics is applicable for all loading orientations, the results for other loading orientations need not match the ones discussed in this work. DDD simulations along multiple orientations are required to understand the dependence of these fluctuation statistics on loading orientations.

4.8 Discussion

A short discussion of the significance and utility of the stress fluctuation statistics is in order. First, the results presented here highlight the importance of characterizing the fluctuations of the internal stress in dislocation systems for use in conjunction with the continuum dislocation dynamics simulations of mesoscale deformation of single crystals. In such a framework, the dislocations on a single slip system are modelled by a (vector) density field $\boldsymbol{\rho}^{[\alpha]}$ on a mesh of a

suitable resolution, d. By definition, this $\boldsymbol{\rho}^{[\alpha]}$ field is a coarse-grained or spatially averaged representation of the dislocation arrangement over local voxels of dimension d. As a corollary of the commutativity of the integral, the stress field caused by this smeared dislocation density is equivalent to smearing the stress field caused by the discrete lines. As a result, the local mean stress field in continuum models is closely analogous to what we have referred to as the mean crystal stress. As such, the stress fluctuations, defined here by the difference between the stress on dislocations and the local crystal stress, may also be thought of as the lost stress information in continuum dislocation dynamics. It is important to note that the stress fluctuation statistics discussed in this work are different from the stress statistics shown in the works of (Csikor and Groma, 2004; Groma and Bakó, 1998; Ispánovity and Groma, 2008). The difference between the two statistics and the trends followed by them are further discussed in appendix A.

Second, we have found in the current work strong discrepancies between the stress on dislocations and the local mean stress in the crystal. In a continuum dislocation dynamics model such as that in (Vivekanandan et al., 2021), it is latter that derives the dislocations motion. This difference can be noted, for example, in Fig. 4.5 and 4.6 by focusing on the tails of the distributions. While the local stress in the crystal reach values on the order of tens of MPa, that on the dislocation lines varies by as much as hundreds of MPa. It was also observed that for voxels with large size higher stress fluctuations were seen compared with the fluctuations for voxels of smaller size. The statistics of the stress fluctuations in dislocation dynamics are thus voxel size dependent. As such, it will be vital to incorporate the stress fluctuation statistics in mean field theories in accordance with the volume over which the coarse-grained density is defined, which is the spatial resolution of the solution of the continuum dislocation dynamics model being used.

Next, the motivation behind this work is to characterize the stress fluctuation statistics so that the corrections to the mean field stress in continuum models can be sampled from the distributions. Sampling the values from the non-scaled distributions directly into continuum dislocation dynamics can be misleading since the sampled values generally lack the information about the local dislocation arrangement. Ideally, the fluctuations in stress due to local dislocation arrangement should be partially represented in terms of dislocation-dislocation correlations which when incorporated in the mean field equations should bring out the fluctuation stress naturally. Since estimating fluctuation stresses in terms of dislocation correlations is beyond the scope of this work, an ad-hoc approach in which the local mean of the corresponding stress of interest,

Schmid or Escaig, is assumed to be a measure capable of representing the local dislocation arrangement in an approximate sense. Hence, the scaled fluctuation stress statistics may be used to estimate corrections to the local stress. It is also important to note that the fluctuation statistics discussed in this work is applicable only for the case of [001] loading. The dependence of these fluctuation statistics on loading orientation needs to be investigated further.

The advantage of sampling stress fluctuation values that is scaled by the local mean is that they can be used in continuum dislocation dynamics as fluctuation about the known local mean field. For instance, in the consideration of cross-slip (a thermally activated process that changes the glide plane of screw dislocation based on the local stress state), the probability that a screw segment will cross-slip is dependent on the stress state of that segment. This probability is given by an Arrhenius type equation which is of the form

$$p \propto e^{-\frac{E_{\mathrm{act}}(\boldsymbol{\sigma})}{KT}} \tag{4.25}$$

where $E_{\mathrm{act}}(\boldsymbol{\sigma})$ is the stress dependent activation energy for the cross-slip process. Based on the functional form chosen for the activation energy formulation, different stress components will be used to accurately capture the local stress state. For example, in the model by Kubin et al (Kubin et al., 1992) the activation energy ($E_{\mathrm{act}}^{\mathrm{k}}$) depends on Schmid stress in the cross slip plane ($\tau_{\mathrm{s}}^{\mathrm{cs}}$), whereas in the model by (Hussein et al., 2015) the activation energy ($E_{\mathrm{act}}^{\mathrm{h}}$) depends on the difference between the Escaig stress on the primary plane ($\tau_{\mathrm{e}}^{\mathrm{p}}$) and cross-slip plane ($\tau_{\mathrm{e}}^{\mathrm{cs}}$). The activation energy for these two models after accounting for stress fluctuation can, respectively, be written in the form

$$E_{\mathrm{act}}^{\mathrm{k}} = -V((\tau_{\mathrm{s}}^{\mathrm{cs}}) - \tau_{\mathrm{III}}) \text{ with } \tau_{\mathrm{s}}^{\mathrm{cs}} = [\sigma_{\mathrm{s}}^{\mathrm{cs}}] * \hat{\sigma}_{\mathrm{s}}^{\mathrm{cs}} + [\sigma_{\mathrm{s}}^{\mathrm{cs}}] \tag{4.26}$$

$$E_{\mathrm{act}}^{\mathrm{h}} = -\left(E_0 - V\left(\left(\tau_{\mathrm{e}}^{\mathrm{p}}\right) - \left(\tau_{\mathrm{e}}^{\mathrm{cs}}\right)\right)\right) \text{ with } \tau_{\mathrm{e}}^{\mathrm{cs}} = [\sigma_{\mathrm{e}}^{\mathrm{cs}}] * \hat{\sigma}_{\mathrm{e}}^{\mathrm{cs}} + [\sigma_{\mathrm{e}}^{\mathrm{cs}}] \tag{4.27}$$

where $[\sigma_{\mathrm{s}}^{\mathrm{cs}}]$, $\left[\sigma_{\mathrm{e}}^{\mathrm{p}}\right]$ and $[\sigma_{\mathrm{e}}^{\mathrm{cs}}]$ correspond to the mean Schmid stress on the cross-slip plane, mean Escaig stress on the primary plane and mean Escaig stress on the cross-slip plane respectively. $\hat{\sigma}_{\mathrm{s}}^{\mathrm{cs}}$ and $\hat{\sigma}_{\mathrm{e}}^{\mathrm{cs}}$ correspond to the scaled Schmid and Escaig stress fluctuation variables and the parameters V, τ_{III} and E_0 are stress independent parameters related to the cross-slip process. Thus, given the magnitude of the fluctuations in local line stress for both Schmid and Escaig stresses, it would be expected that sampling the local fluctuation stresses to evaluate the activation barrier for cross-slip events in continuum dislocation dynamics using the same model as in discrete dislocation

dynamics. This facilitates the implementation of cross slip as compared with that used in (Xia et al., 2016), for example.

As noted above, both Schmid and Escaig stress fluctuations are required for the implementation of cross slip in continuum dislocation dynamics. The Schmid stress fluctuations, however, can be used to capture the lost stress information in continuum dislocation dynamics as far as the dislocation glide is concerned. Implementing this work in 3D, say, the continuum dislocation dynamics model based on the *line bundle approximation* (Lin et al., 2021; Vivekanandan et al., 2021; Xia and El-Azab, 2015) would generalize the earlier piece of work in (Bakó and Groma, 1999), where 2D edge-on stochastic dislocation dynamics was considered. However, accounting for the lost stress information using the correlation would be more robust for that it ensures stress equilibrium. Further discussion of this topic is beyond the scope of the current work.

4.9 Concluding remarks

In this work, the internal stress distribution of 3D dislocation configuration was characterized relative to the local mean stress, a field used in coarse-grained dislocation dynamic models to represent the local stress state. The motivation behind this work was to quantify the discrepancies inherent in the calculation of the internal stress field from coarse-grained dislocation eigenstrains relative to the underlying discrete system. The difference between local stress on dislocation lines and the mean stress field, termed here the fluctuation stress, were investigated by Monte Carlo simulations and the relevant PDFs were collected. These PDFs were compared to the counterpart for the stress fluctuations in the crystals.

From the analysis of the stress distribution in the simulation domain for the case of [001] monotonic loading, it was found that the average Schmid and Escaig fluctuation stresses on dislocations were non-zero. The crystal average counterparts were found to be zero, as expected. It was also observed that the variation in the fluctuation stress fall in the range of ±5 times the local mean stress. This observation underscores the need for incorporating internal stress fluctuations in mean field theories of dislocation dynamics. An important observation made during the current investigation is that the PDF of the fluctuation statistics of both the Schmid stress and Escaig stress follows a Cauchy distribution. While we did not present a theoretical justification for this, we refer the reader to the works in (Csikor and Groma, 2004; Ispánovity and Groma, 2008), which studied

stress statistics at random points in the crystal for a theoretical insight gained in studying 2D dislocation systems. It was found that the distributions of these fluctuation statistics have smaller peaks and wider widths at larger strains, i.e., at larger dislocation densities. It was also demonstrated that the fluctuation statistics depends on the voxel size used in establishing the local mean stress field in the crystal. Hence, it is important to choose the voxel size in accordance with the resolution used in defining the mean field stress in continuum dislocation dynamics.

Sampling fluctuation statistics from these distributions is just the first step towards accurately characterizing the local stress state on dislocations in mean field models. Although an ad-hoc approach to model dislocation processes like cross-slip was discussed, further analysis is required to relate the fluctuation statistics to the local dislocation arrangement and thus establish connection with the dislocation density correlations. If successful, the same approach can also be used to capture the distribution of dislocation velocity and gain insight toward density-based mobility models, which is an essential closure of continuum dislocation dynamics models.

4.10 Appendix

The works in (Csikor and Groma, 2004; Groma and Bakó, 1998; Ispánovity and Groma, 2008) focuses on the stress statistics in the crystal in 2D for systems of straight edge dislocations. Those works showed that the PDF of the crystal stress follows a Cauchy distribution in the central part and decays as $1/|\sigma^3|$ at large stress values. To verify whether the same trend is observed for the 3D curved dislocation configurations, Schmid stress statistics sampled in the crystal for slip system 1 is shown in Fig. 4.A1. Fig. 4.A1(a) shows that indeed the central part of the distribution follows the Cauchy distribution and at higher stress it decays as $1/|\sigma^3|$ as shown in Fig. 4.A1(b). The deviation from the Cauchy fit can be observed at higher stress levels by comparing it with the inverse cubic fit in Fig. 4.A1(b).

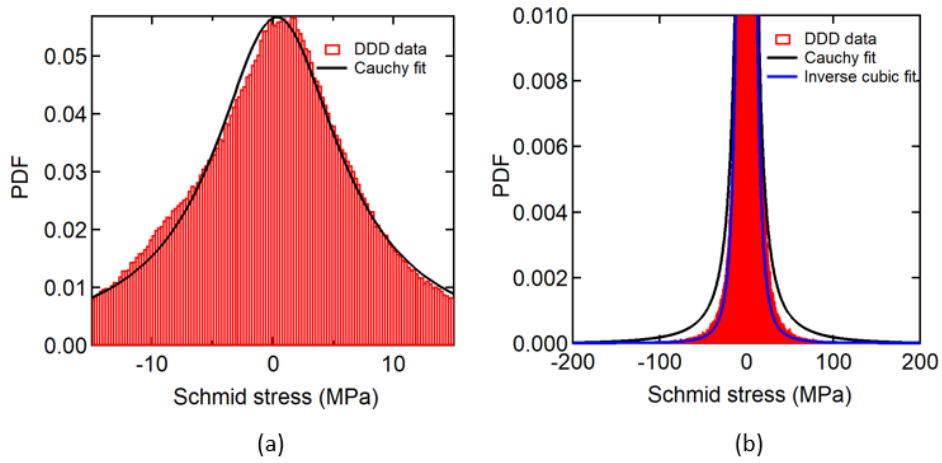

Fig. 4.11.(a) Central part and (b) tail part of PDF of Schmid stress at crystal points for slip system 1 fit to both Cauchy and inverse cubic function.

On the other hand, the PDF of stress fluctuations discussed in this work focuses on the difference between the stress on dislocations and the mean stress in its neighborhood. It is important to note that the mean stress surrounding the dislocation is also a variable which changes depending on the chosen voxel location and voxel size. Hence, establishing a direct relationship with the crystal stress statistics discussed in the works of (Csikor and Groma, 2004; Groma and Bakó, 1998; Ispánovity and Groma, 2008) is not straightforward. It is interesting to note, however, that the central part of stress fluctuation statistics follows the Cauchy distribution like the stress statistics, but the $1/|\tilde{\sigma}^3|$ decay is not observed at higher stress levels.

For the case of crystal stress statistics, it is known that the variance, which is given as $\langle\sigma^2\rangle = \int_{-\sigma_{max}}^{\sigma_{max}} \sigma^2 p(\sigma) d\sigma$, is proportional to energy of the system. In addition to that, it is also known that the energy of the system is proportional to the logarithm of the core radius of dislocation (Zaiser, 2015). For this to hold, the PDF of the stress statistics should decay as $1/|\sigma^3|$ since the maximum stress σ_{max} is proportional to $1/r_c$. The same cannot be expected to hold for statistics of stress fluctuations on dislocation lines since only a subset of the crystal points is considered and the fact that the mean stress varies in space.

5. CROSS-SLIP MODEL

A portion of this chapter has been published in the International Journal of Plasticity by Vignesh Vivekanandan, Ben Anglin and Anter El-Azab as "A data driven approach for cross-slip modelling in continuum dislocation dynamics", 164, 103597. https://doi.org/10.1016/j.ijplas.2023.103597

5.1 Abstract

Cross-slip is a thermally activated process by which screw dislocation changes its glide plane to another slip plane sharing the same Burgers vector. The rate at which this process happens is determined by a Boltzmann type expression that is a function of the screw segment length and the stress acting on the dislocation. In continuum dislocation dynamics (CDD), the information regarding the length of the screw dislocation segment and local stress state on dislocations are lost due to the coarse-grained representation of the density. In this work, a data driven approach to characterize the lost information by analyzing the discrete dislocation configurations is proposed to enable cross-slip modeling in the CDD framework in terms of the coarse-grained dislocation density and stress fields. The analysis showed that the screw segment length follows an exponential distribution, and the stress fluctuations, defined as the difference between the stress on the dislocations and the mean field stress in CDD, follows a Cauchy distribution. A novel approach for cross slip implementation in CDD employing the screw segment length and stress fluctuation statistics was proposed and rigorously tested by comparing the CDD cross-slip rates with discrete dislocation dynamics (DDD) rates. This approach has been applied in conjunction with three cross-slip models used in DDD simulations differing mainly in the functional form of cross slip activation energy. It was found that different cross-slip activation energy formulations yielded different cross-slip rates, yet the effect on mechanical stress-strain response and dislocation density evolution was minimal for the [001] type loading.

5.2 Introduction

In the seminal work of Taylor (Taylor, 1934), it was first proposed that dislocations are the carriers of plasticity in metals. From then on, many dislocation-based phenomenological theories (Argon, 2007) have been proposed to characterize plastic deformation in metals. These theories were unable to capture the size effects (Fleck et al., 1994) observed in the experiments due to the

lack of information required to describe the evolution of local dislocation microstructure. This prompted researchers to model plasticity by directly modeling dislocation dynamics, which was made possible by the recent improvements in computing capabilities (A Arsenlis et al., 2007; Devincre et al., 2011; Hussein et al., 2015; Po et al., 2014; Sills et al., 2018; Weygand et al., 2002). Due to computational limitations, however, direct numerical simulation of dislocation dynamics has bene found infeasible in all ranges of deformation encountered in experiments and, hence, the community turned attention to the development of continuum dislocation dynamics (CDD) to capture the spatial temporal evolution of dislocations using density-based approaches (Hochrainer, 2015; Kalaei et al., 2022; Leung and Ngan, 2016; Lin et al., 2021; Lin and El-Azab, 2020; Monavari and Zaiser, 2018; Sandfeld et al., 2015; Schulz et al., 2019; Starkey and El-Azab, 2022; Sudmanns et al., 2019; Vivekanandan et al., 2021; Xia and El-Azab, 2015). CDD is expected to play key roles in the field of metal plasticity in area such as the prediction and interpretation of the constitutive response of metals form first principles of dislocation dynamics, capturing the self-organization of dislocations into cell and other types of structures, which aids fundamental recrystallization investigations, and aiding the current use of Synchrotron X-ray to probe deformed metals. Completing the CDD framework requires modelling different dislocation mechanisms within the CDD framework. One such important mechanism is cross-slip, which is a thermally activated process in which the screw dislocations change their glide plane. It is well established that cross slip contributes to pattern formation (Kubin et al., 2009), dynamic recovery (Madec et al., 2002) and strain hardening (Devincre et al., 2007) in metals. Therefore, it is essential for continuum dislocation dynamics models to accurately incorporate the cross-slip phenomenon to aid the prediction of dislocation microstructure evolution.

Broadly, there exists two types of models that explain the mechanism of cross-slip in FCC materials, Friedel-Escaig mechanism (FE) (Bonneville and Escaig, 1979) and Fleischer mechanism (FL) (Fleischer, 1959). The FE mechanism postulates that cross-slip happens in, say, FCC crystals when the two dislocation partials form a constriction on the glide plane and dissociate onto the cross-slip plane whereas the FL mechanism predicts the leading partial splits into a partial dislocation on the cross-slip plane and a stair-rod dislocation which eventually reacts with the trailing partial and completes the cross-slip process. Capturing the rate at which this process happens depends upon the activation energy barrier of the critical configuration and the length of the screw segment. Hence, it is essential for continuum dislocation dynamics models to incorporate

these two parameters for accurately predicting the cross-slip behavior. It is worth mentioning that the above mechanisms are valid only for FCC materials where dislocations can split into partials. For the case of BCC materials, cross-slip occurs through much more complicated process (Rhee et al., 1998)

Continuum dislocation dynamics models represent dislocations as coarse-grained density fields which have information about the average line orientation and magnitude of the dislocation density. The advantage of using this spatially smooth variable in studying the dynamics is the evolution of the system can be encapsulated in terms of the average quantity, e.g., dislocation density, rather than tracking the motion of all discrete states (Bertin et al., 2015; Cui et al., 2015; Devincre et al., 2011; Hussein et al., 2015; Po et al., 2014; Sills et al., 2018; Stricker et al., 2018; Zhou and LeSar, 2012) that make the density. Conversely, coarse graining throws away the details corresponding to the discrete states like dislocation segment length distribution and dislocation-dislocation correlation which are important parameters required to model local processes like cross-slip. Hence, for the coarse-grained models to remain consistent with their lower-level counterparts, care must be taken to introduce the statistical information regarding the cross-slip process.

There exist different classes of continuum dislocation based models in the literature (Acharya and Roy, 2006; Hochrainer, 2015; Kalaei et al., 2022; Li et al., 2014; Lin et al., 2021; Lin and El-Azab, 2020; Monavari and Zaiser, 2018; Sandfeld et al., 2015; Schulz et al., 2019; Starkey and El-Azab, 2022; Sudmanns et al., 2019; Vivekanandan et al., 2021; Xia and El-Azab, 2015). Here, we focus upon the vector-based CDD models (Lin et al., 2021; Lin and El-Azab, 2020; Starkey and El-Azab, 2022; Vivekanandan et al., 2021; Xia and El-Azab, 2015) and higher order continuum models (Hochrainer, 2015; Sandfeld et al., 2015; Sudmanns et al., 2019) that explicitly capture the cross-slip process. The first attempt to characterize the density-based rates of cross-slip process by systematically studying it using DDD (Devincre et al., 2011) was done by (Deng and El-Azab, 2010), which was then improved by (Xia et al., 2016). In the latter work, attempts were made to characterize the cross-slip process for vector based CDD models by temporally coarse graining the time series data of cross-slip statistics obtained during every time step of the DDD simulations. The cross-slip statistics used in the time series were obtained by monitoring the fraction of screw segments that cross-slipped throughout the DDD simulation domain in each time step. These coarse-grained time series were then used to sample cross-slip

rates in CDD based on the strain levels. Another approach to modeling cross-slip was proposed by (Sudmanns et al., 2019) in which they used the DDD cross-slip probability expression (Kubin et al., 1992) to calculate the cross-slip rate. In their work, the length of screw segment allowed to cross-slip, which is an input to the cross-slip probability expression, was estimated as the minimum of the average loop radius, defined as the fraction of dislocation density and curvature density, and the mean dislocation spacing. Although both the models make use of information from DDD, there is still a scope for improvement. For instance, the model proposed by (Deng and El-Azab, 2010) and (Xia et al., 2016) does not consider the local stress effects to estimate the CDD cross-slip rate but rather uses the average cross-slip rate information obtained from DDD. Similarly, the model proposed by Sudmanns.et.al (Sudmanns et al., 2019) does not consider the distribution of screw segment length rather estimates the average length based on the coarse grained fields for cross-slip probability estimation. In addition to that, it was recently pointed out that the stress faced by a discrete dislocation is markedly different from the mean stress field (Vivekanandan et al., 2022), which is not accounted for in their cross-slip probability evaluation. Hence, there is a need for a different approach which relates the coarse-grained dislocation density and stress fields in CDD to the discrete screw segment length distribution and stress field on dislocations to obtain the cross-slip rates accurately.

Since cross-slip is a thermally activated process, the estimation of the activation energy barrier required for the screw segment to transition from glide plane to cross-slip plane is the crucial step. Predominantly, two different approaches have been considered in the literature to estimate the activation energy barrier; the line tension models (Kang et al., 2014; Malka-Markovitz and Mordehai, 2018) and atomistic simulation models (Kuykendall et al., 2020; Rao et al., 2013). Based on these two approaches, different activation energy expressions were derived and used in DDD simulations. Most commonly used activation energy expression was the one first proposed by (Kubin et al., 1992) and later modified by (Devincre et al., 2011) which states that activation energy of cross-slip barrier mainly depends on the Schmid stress along the primary plane (τ_s^p) for an immobile dislocation and Schmid stress along cross-slip plane (τ_s^{cs}) for a mobile dislocation. The parameters used in this model were calibrated based on the experimental observations at the initiation of stage III hardening resulting in activation energy of the form $E_{act} = -V\left(\left|\tau_s^p\right| - \tau_{III}\right)$ or $E_{act} = -V(|\tau_s^{cs}| - \tau_{III})$ depending on whether the dislocation is immobile or mobile, where V is the activation volume and τ_{III} is the resolved shear stress at the beginning of stage III hardening.

Contrary to the Kubin's model, some studies (Kang et al., 2014; Li et al., 2021) showed that the effect of Escaig stress on the activation barrier is much more significant than the Schmid stress. Based on atomistic studies conducted by Rao and co-workers (Rao et al., 2013, 2011, 2010), Hussein and co-workers (Hussein et al., 2015) proposed a new cross-slip model in which the activation energy of cross-slip barrier was assumed to be linearly dependent on the difference in Escaig stress in the primary plane $\left(\tau_{\mathrm{e}}^{\mathrm{p}}\right)$ and cross-slip plane $(\tau_{\mathrm{e}}^{\mathrm{cs}})$ as follows: $E_{\mathrm{act}} = E_{\mathrm{cons}} - V\left(\tau_{\mathrm{e}}^{\mathrm{p}} - \tau_{\mathrm{e}}^{\mathrm{cs}}\right)$ where E_{cons} is the constriction energy. Apart from these two models, Malka-Markovitz and Mordehai (Malka-Markovitz and Mordehai, 2019, 2018) derived a closed form expression for the stress dependent activation energy barrier based on the line tension model by employing harmonic approximation to obtain the interaction energy between partial dislocations. In this model, the contributions of both Schmid stress and Escaig stress in glide and cross-slip plane were considered in the activation energy expression.

In this work, a new cross-slip model for vector-based CDD model for single crystals is proposed. This model incorporates information about the screw segment statistics and internal stress fluctuations. Section 5.2 introduces the fundamental equations of the CDD model which is followed in section 5.3 by a discussion of the strategy for estimating the cross-slip rate using DDD statistics in terms of coarse-grained fields. In section 5.4, the validity of the proposed model is demonstrated by comparing the results with the cross-slip rates evaluated using the DDD. The effects of the different cross-slip activation energy formulations on the mechanical behavior and dislocation microstructure evolution in CDD is also discussed in this section. We conclude by discussing the results and summarizing the conclusions in Section 5.5 and 5.6.

5.3 Continuum dislocation dynamics model

Continuum dislocation dynamics models generally include two sets of equations describing the crystal mechanics and dislocation kinetics, which, together, capture the spatial-temporal evolution of dislocation system and the deformation and mechanical state of the crystal under mechanical boundary conditions. The crystal mechanics part is modelled as an eigen distortion problem and dislocation kinetics is captured in terms of a curl type dislocation transport reaction coupled with dislocation processes like cross-slip and junction reactions. The governing equations for the crystal mechanics include the stress equilibrium equation, Hooke's law and boundary conditions:

$$\boldsymbol{\nabla}\cdot\boldsymbol{\sigma} = \mathbf{0} \text{ in } \Omega, \tag{5.1}$$
$$\boldsymbol{\sigma} = \boldsymbol{C} : (\boldsymbol{\beta}^{\mathrm{e}})_{\mathrm{sym}} \text{ in } \Omega,$$
$$\boldsymbol{\beta}^{\mathrm{e}} = \boldsymbol{\nabla}\boldsymbol{u} - \boldsymbol{\beta}^{\mathrm{p}},$$
$$\boldsymbol{u} = \bar{\boldsymbol{u}} \text{ on } \partial\Omega_{\mathrm{u}},$$
$$\boldsymbol{n}\cdot\boldsymbol{\sigma} = \bar{\boldsymbol{t}} \text{ on } \partial\Omega_{\mathrm{t}}.$$

In the above equation, $\boldsymbol{\sigma}$ is Cauchy stress tensor, $\boldsymbol{C}$ is elastic tensor, $\boldsymbol{u}$ is the displacement, $\boldsymbol{\beta}^{\mathrm{e}}$ and $\boldsymbol{\beta}^{\mathrm{p}}$ are elastic and plastic distortions, respectively, Ω is the domain of solution, $\partial\Omega_{\mathrm{u}}$ and $\partial\Omega_{\mathrm{t}}$, are the parts of the boundary on which the displacement $\boldsymbol{u} = \bar{\boldsymbol{u}}$ and the traction $\bar{\boldsymbol{t}}$ are prescribed respectively. Solution of the above boundary value problem yields the stress which is then used to determine the dislocation velocity for each slip system, i, using a linearized mobility law commonly used in literature (Lin and El-Azab, 2020; Yefimov et al., 2004; Zaiser et al., 2001) as follows

$$v^i = \mathrm{sgn}\left(\tau^i\right)\frac{b}{B}\langle|\tau|^i - \left(\tau_0 + \tau_{\mathrm{p}}^i\right)\rangle, \tag{5.2}$$

where b and B are the magnitude of the Burgers vector and the drag coefficient, respectively. The $\langle\cdot\rangle$ corresponds to the Macauley bracket and sgn function corresponds to the sign of the argument. τ^i is the resolved shear stress along slip system i and τ_0 is the lattice friction. τ_{p}^i is the Taylor hardening stress that accounts for short range interactions due to sessile junctions on slip system i which is defined as

$$\tau_{\mathrm{p}}^i = \alpha\mu b\sqrt{\sum_j a_{ij}\rho^j}\; F\left(\rho^i, \rho^{\mathrm{f}}\right). \tag{5.3}$$

In the above, α is scaling factor, μ is the shear modulus, b is the magnitude of Burgers vector, a_{ij} is the average strength of an interaction between slip system i and j, ρ^j is the scalar dislocation density of the slip system j interacting with slip system i and ρ^{f} is the sum of the dislocation densities of the slip systems that react with slip system i and form Lomer or Hirth lock. $F\left(\rho^i, \rho^{\mathrm{f}}\right)$ corresponds to a function that accounts for the dislocation pile up effect (Vivekanandan et al., 2021; Zhu et al., 2016). In this work, $F\left(\rho^i, \rho^{\mathrm{f}}\right)$ is assumed to have the form $F\left(\rho^i, \rho^{\mathrm{f}}\right) =$

$\left(1 + p\mathrm{e}^{(q\rho^i/\rho^{\mathrm{f}} - 1)}\right)^{-1}$ based on the work of (Vivekanandan et al., 2021), where p and q are parameters that determine the shape and the rate at which the function decays.

The dislocation velocity obtained from equation (5.2) for every slip system i is used to solve the dislocation kinetics equations described below, following the approach used in (Vivekanandan et al., 2021),

$$\dot{\boldsymbol{\rho}}^i_{\mathrm{g}} = \boldsymbol{\nabla} \times \left(\boldsymbol{v}^i \times \dot{\boldsymbol{\rho}}^i_{\mathrm{g}}\right) + \dot{\boldsymbol{\rho}}^i_{\mathrm{cs}} + \dot{\boldsymbol{\rho}}^i_{\mathrm{jun}}, \tag{5.4}$$

$$\dot{\boldsymbol{\rho}}^i_{\mathrm{v}} = \dot{\boldsymbol{\rho}}^i_{\mathrm{v_{cs}}} + \dot{\boldsymbol{\rho}}^i_{\mathrm{v_{jun}}},$$

$$\boldsymbol{\nabla} \cdot \left(\boldsymbol{\rho}^i_{\mathrm{g}} + \boldsymbol{\rho}^i_{\mathrm{v}}\right) = 0.$$

It is worth mentioning that the above system of equations is valid only for the vector based CDD model, which operates at a fine resolution such that at every point the dislocation density field can be thought to have a single line orientation (Lin and El-Azab, 2020; Vivekanandan et al., 2021; Xia and El-Azab, 2015). In the above system of equations, the first equation corresponds to the change in glide dislocation density due to dislocation transport and dislocation reactions. The curl type term captures the change in glide dislocation density due to dislocation transport. $\dot{\boldsymbol{\rho}}^i_{\mathrm{cs}}$ captures the change in glide dislocation density due to cross-slip which accounts for both new dislocations added to the slip system i as well as dislocations that was removed from slip system i. $\dot{\boldsymbol{\rho}}^i_{\mathrm{jun}}$ corresponds to the change in glide dislocation density due to formation and destruction of dislocation junction reactions like glissile junction, Lomer locks and Hirth locks. The second equation corresponds to the rate of change of virtual dislocation density, which is defined as the non-physical dislocation density that quantifies the amount of physical dislocations that were involved in the dislocation processes like cross-slip and junction and are no longer available for dislocation glide in their original slip system. It is important to note that virtual density is a place holder used to keep track of dislocations involved in dislocation reactions and does not contribute to the distortion of the crystal. $\dot{\boldsymbol{\rho}}^i_{\mathrm{v_{cs}}}$ captures the change in virtual dislocation density due to cross-slip and $\dot{\boldsymbol{\rho}}^i_{\mathrm{v_{jun}}}$ corresponds to the change in virtual dislocation density due to formation and destruction of dislocation junction reactions like glissile junction. The third equation corresponds to the dislocation closure constraint that ensures dislocations do not end inside the crystal given that the initial dislocation configuration is divergence free.

Modelling the evolution of dislocations involved in dislocation processes like junctions and cross-slip requires information about the rate at which these processes occur. Since

dislocations in CDD are represented as coarse grained fields, they inherently lack the local information about the individual dislocations involved in these processes. In this paper, a new approach based on our recent work (Vivekanandan et al., 2022) is formulated to model cross-slip behavior in CDD.

5.4 Cross-slip rate estimation in CDD

Cross-slip is a thermally activated process by which a screw dislocation changes its original glide plane to another glide plane which shares the same Burgers vector. In CDD, the change in dislocation density due to this process for slip system i is denoted by $\dot{\boldsymbol{\rho}}^{i}_{\mathrm{cs}}$ in equation (5.4) which can be defined as

$$\dot{\boldsymbol{\rho}}^{i}_{\mathrm{cs}} = \dot{r}^{j\to i}_{\mathrm{cs}}\boldsymbol{\rho}^{j}_{\mathrm{s}} - \dot{r}^{i\to j}_{\mathrm{cs}}\boldsymbol{\rho}^{i}_{\mathrm{s}}, \tag{5.5}$$

where $\boldsymbol{\rho}^{i}_{\mathrm{s}}$ and $\boldsymbol{\rho}^{j}_{\mathrm{s}}$ denote screw dislocation densities in slip system i and j, $\dot{r}^{i\to j}_{\mathrm{cs}}$ and $\dot{r}^{j\to i}_{\mathrm{cs}}$ correspond to the cross-slip rates of screw segments that cross-slipped from $i \to j$ and $j \to i$ respectively. It is evident from equation (5.5) that the cross-slip rates $\dot{r}_{\mathrm{cs}}$ should be determined accurately to characterize the cross-slip process in CDD. In DDD models, the probability for a discrete screw segment of length L to cross-slip is estimated using an Arrhenius type equation (Hussein et al., 2015; Kubin et al., 1992; Malka-Markovitz et al., 2021) as follows

$$P(L,\boldsymbol{\sigma}) = cL\mathrm{e}^{-\frac{E_{\mathrm{act}}(\boldsymbol{\sigma})}{kT}}, \tag{5.6}$$

where c is normalization constant, $E_{\mathrm{act}}(\boldsymbol{\sigma})$ is the cross-slip activation energy barrier which depends on the local stress state of the dislocation segment, k is the Boltzmann constant and T is the temperature. Based on the cross-slip probability value, the cross-slip event is executed following the Metropolis algorithm. Then, the average cross-slip rate for a given time step over the entire simulation domain for the discrete case can be written as

$$\dot{r}^{i\to j}_{\mathrm{cs,DDD}} = \frac{\sum l^{i}_{\mathrm{cs,screw}}}{\sum l^{i}_{\mathrm{screw}}} \cdot \frac{1}{\Delta t}, \tag{5.7}$$

where $l_{\mathrm{cs,screw}}$ and l_{screw} correspond to the length of screw segments belonging to slip system i that cross-slipped to slip system j and length of screw segments belonging to slip system i respectively and Δt is the time step.

In CDD, the dislocation content is represented as density field which is a coarse-grained representation of the discrete dislocation. For the case of vector density based CDD model (Lin and

El-Azab, 2020; Vivekanandan et al., 2021; Xia and El-Azab, 2015), the resolution over which the coarse graining is performed is small enough such that the underlying discrete dislocations can be assumed to have the same line orientation as the density field. Therefore, if the coarse-grained dislocation density field in CDD is of screw character, then all the underlying discrete dislocations is of screw character as well. It is important to note that this might not be true for other continuum models (Hochrainer, 2015; Sudmanns et al., 2019) where at any given point, dislocations of different orientations can coexist. Since cross-slip is a local process that depends on the discrete length of the screw segment and the stress on the screw segment, a link must be established between the coarse grained state in CDD and the underlying discrete dislocation states to estimate the cross-slip rate, which will enable us to capture the behavior of the dislocation system based only on the coarse-grained description. The link is established by studying the relationship between the local state and the coarse grained state by analyzing the discrete dislocation configurations from DDD simulations. The local state is readily available from DDD simulation whereas the coarse grained state is evaluated by sequentially performing spatial window average over a small volume across the DDD domain. The link established through the analysis from DDD simulation can readily be used in CDD model if the simulation conditions, material parameters and dislocation mechanisms that enable topological rearrangement are modelled in the same fashion since they determine the dislocation network evolution.

In this work, a DDD simulation that is loaded monotonically along the [001] direction with a strain rate of 20 s^{-1} is performed to establish the link between coarse grained state in CDD and the underlying dislocation state. The first step in establishing such a link between the coarse-grained CDD dislocation state and the underlying discrete dislocation states is determining the length distribution of discrete dislocation segments. The length distribution of the screw segments is analyzed by taking snapshots of the DDD simulation at different strain levels. The initial dislocation configuration chosen for this simulation comprised of 24 edge dipolar loops (Motz et al., 2009), two per slip system that are randomly distributed in a simulation domain of size $4.4\mu\text{m} \times 4.9\mu\text{m} \times 5.84\mu\text{m}$ with periodic boundary conditions. The simulation domain size in DDD was chosen with the aim to capture the evolution of dislocations with adequate resolution such that the dislocation patterns can be captured. The initial dislocation configuration and the boundary conditions were chosen such that a realistic dislocation network topology is used to study

the behavior in the bulk of the crystal free from any boundary effects. The FCC material parameters used in the simulation are listed in Table 5.1.

Table 5.1. Material parameters used in the DDD and CDD simulations.

Material parameters	**Values**	**Material parameters**	**Values**
Shear modulus (μ)	75 GPa	Stacking fault energy (γ)	0.03 J/m^2
Poisson's ratio (ν)	0.26	Fitting parameter (ζ_{Ls})	0.6
Drag coefficient (B)	25×10^{-5} Pa s	Constriction energy (E_{cons})	1.55 eV
Burgers vector (b)	0.254 nm	Activation volume (V)	1800b^3 m^3
Stress at beginning of stage III hardening (τ_{III})	52 MPa	Temperature (T)	300 K

Fig. 5.1(a) shows the screw segment length distribution of a DDD configuration throughout the simulation domain. It is evident from the figure that screw segment length in DDD follows an exponential distribution whose functional form is given by $S(x;\phi) = \frac{1}{\phi}\mathrm{e}^{-\frac{x}{\phi}}$, where ϕ is the mean of the distribution. Similar type of distribution has been observed in (Sills et al., 2018), wherein they studied the link length distribution, which refers to length of dislocation between two pinning points in DDD. It is also important to note that the screw segments whose length is below 25nm are ignored in the distribution. The reason behind this exclusion is that the resolved shear stress required to bow out small straight dislocations is high due to its high line tension. Hence, in DDD cross-slip for small screw segments is not worth considering since they do not evolve on the cross-slip plane after cross-slipping; rather they cross-slip back again into the original glide plane after some short time. Fig. 5.1(b) shows the exponential fits of screw segment length distribution across different strain levels. From the curve fits, we can observe that the average screw segment length decreases with increase in strain. This trend is expected because the number of dislocations in the simulation domain increases as the strain increases and consequently chances of collisions between dislocations resulting in junctions also increases. This results in long screw segments splitting into two smaller segments, thereby reducing the mean length of the screw segments in the simulation

domain. Furthermore, it was found that Lambda defined as $\Lambda = \frac{1}{\bar{l}}$, where $\bar{l}$ is the mean screw segment length, increases linearly with strain as shown in Fig. 5.1(c). Based on the statistics of screw segment length, the average screw segment length $\bar{l}$ at every point in CDD can be estimated by sampling value from the exponential distribution for a given strain level. Therefore, for given screw dislocation density ρ_s, the number of underlying screw segments per unit volume with an average length $\bar{l}$ can then be defined as $N = \frac{\rho_s}{\bar{l}}$.

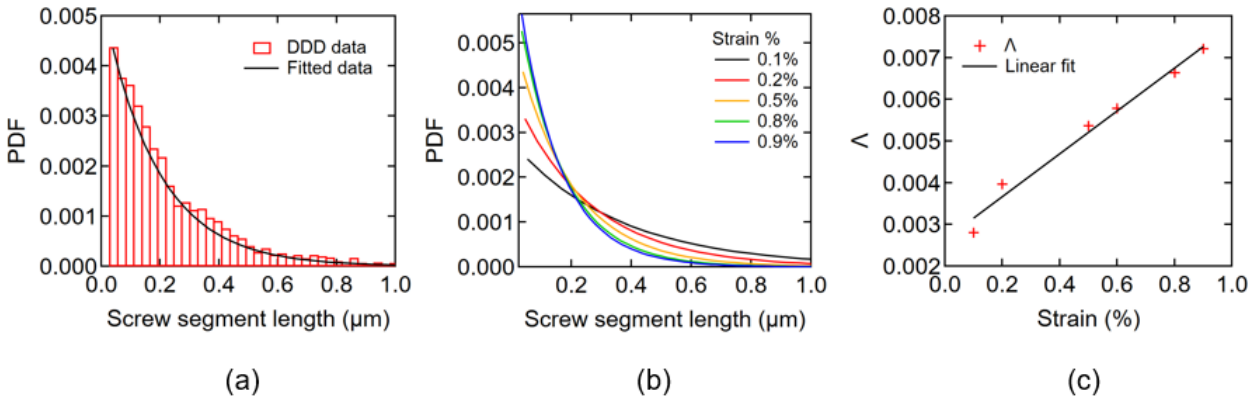

Fig. 5.1. (a) Length distribution of screw segments for a dislocation configuration sampled from a monotonic DDD simulation at 0.5% strain. (b) Exponential fits of screw segment length distribution at different strain levels. (c) Mean of the exponential fits in (b) fitted to a line.

The second step in establishing a mapping between the coarse-grained CDD dislocation state and the underlying discrete dislocation states is characterizing the local stress state of the underlying screw dislocation in terms of the coarse-grained stress field. Since dislocations are represented as coarse grained density in CDD, the local information regarding the stress state of individual underlying dislocations is lost. Hence, there is a need to formulate a method to estimate the local stress state in terms of coarse-grained stress. The earlier work of a subgroup of authors (Vivekanandan et al., 2022) studied the relationship between the two quantities by analyzing DDD configurations for segments of all orientations. Since cross-slip is relevant only for screw dislocations, the analysis must be performed again exclusively for screw segments. Therefore, a set of discrete dislocation configurations from the DDD simulation, which is also used to extract screw segment lengths, is analyzed to determine the relationship between the local stress and the coarse-grained stress for screw segments. The analysis involves performing coarse graining over

voxels for a discrete dislocation configuration, which are regions of small volumes commensurate with the CDD mesh size, thereby converting the discrete states to continuum fields. The details regarding the coarse graining process and stress calculation can be found in our earlier work (Vivekanandan et al., 2022). It is worth mentioning that the screw segment statistics and stress fluctuation statistics are specific for the conditions under which the simulation was performed. Targeted DDD simulations and analysis are required to generalize the statistics extracted from DDD such that it is suitable for use in CDD irrespective of loading condition, dislocation density and initial dislocation configuration used in the simulation. Conducting such investigations is out of scope of this manuscript since it is focused only on developing a framework that incorporates relevant statistics from DDD into CDD model. Hence, for different loading conditions and material parameters, the proposed framework can still be used by performing appropriate DDD simulations that are consistent with CDD simulation setup before extracting the relevant statistical information. Following the steps mentioned in (Vivekanandan et al., 2022), the relationship between the stress on the dislocation line and the coarse grained stress in the voxel is characterized in terms of the scaled stress fluctuation $\widehat{\boldsymbol{\sigma}}^{\mathrm{d}}$ which is given by the following equation

$$\widehat{\boldsymbol{\sigma}}^{\mathrm{d}}(\boldsymbol{r}'_k) = \frac{\boldsymbol{\sigma}^{\mathrm{d}}(\boldsymbol{r}'_k) - [\boldsymbol{\sigma}^{\mathrm{c}}]_{\lfloor \boldsymbol{r}_k \rfloor}}{[\boldsymbol{\sigma}^{\mathrm{c}}]_{\lfloor \boldsymbol{r}_k \rfloor}} \quad \text{for } \boldsymbol{r}'_k \in \Lambda \text{ and } \boldsymbol{r}_k \in \mathrm{S}, \tag{5.8}$$

where $\boldsymbol{\sigma}^{\mathrm{d}}(\boldsymbol{r}'_k)$ represents the stress on a dislocation line located at the point with position vector $\boldsymbol{r}'_k$ within the voxel**,** $[\boldsymbol{\sigma}^{\mathrm{c}}]_{\lfloor \boldsymbol{r}_k \rfloor}$ represents the average stress within a voxel which is estimated by taking the average stress value of all crystal points $\lfloor \boldsymbol{r}_k \rfloor$ located within the voxel. Λ and S corresponds to the set of points on the dislocation and set of points on the crystal respectively. For the case of cross-slip, the stress fluctuation statistics of two components of stress tensor $\boldsymbol{\sigma}$, namely Schmid and Escaig are relevant. Schmid stress τ_{s} is the resolved shear stress that drives the dislocation motion while Escaig stress τ_{e} is the stress component that widens or shrinks the stacking fault between partial dislocations. If the Burgers vector of a given slip system i is defined as $b\widehat{\boldsymbol{b}}^i$, with b being its magnitude, the slip plane normal be $\widehat{\boldsymbol{n}}^i$, and the direction of glide vector be $\widehat{\boldsymbol{d}}^i = \widehat{\boldsymbol{n}}^i \times \widehat{\boldsymbol{b}}^i$, then the Schmid and Escaig components along a slip system i can then be defined as

$$\tau_{\mathrm{s}}^i = \left(\left(\boldsymbol{\sigma} \cdot \widehat{\boldsymbol{b}}^i \right) \times \widehat{\boldsymbol{b}}^i \right) \cdot \widehat{\boldsymbol{d}}^i, \tag{5.9}$$

$$\tau_{\mathrm{e}}^{i} = -\left(\left(\boldsymbol{\sigma}\cdot\widehat{\boldsymbol{d}}^{i}\right)\times\widehat{\boldsymbol{b}}^{i}\right)\cdot\widehat{\boldsymbol{d}}^{i}. \tag{5.10}$$

The scaled fluctuation statistics of Schmid and Escaig component of the stress tensor estimated based on equation (8) on the screw dislocations throughout the simulation domain is cast in the form of probability distribution function (PDF) as shown in Fig. 5.2. The PDF in Fig. 5.2 can be captured to a reasonable extent using a Cauchy distribution whose functional form is $H(x: x_0, w) = \frac{1}{\pi}\left(\frac{w}{(x-x_0)^2+w^2}\right)$ where x_0 is the center of the distribution and w is the full width at the half maximum. Fig. 5.3 shows the variation of the scaled fluctuation statistics with respect to the strain level. It can be observed that the peak of the distribution decreases and width of the distribution increases as the strain level is increased. The results of fluctuation statistics for screw segments follows the similar trend with minor differences discussed in (Vivekanandan et al., 2022) which studied dislocations of all orientations.

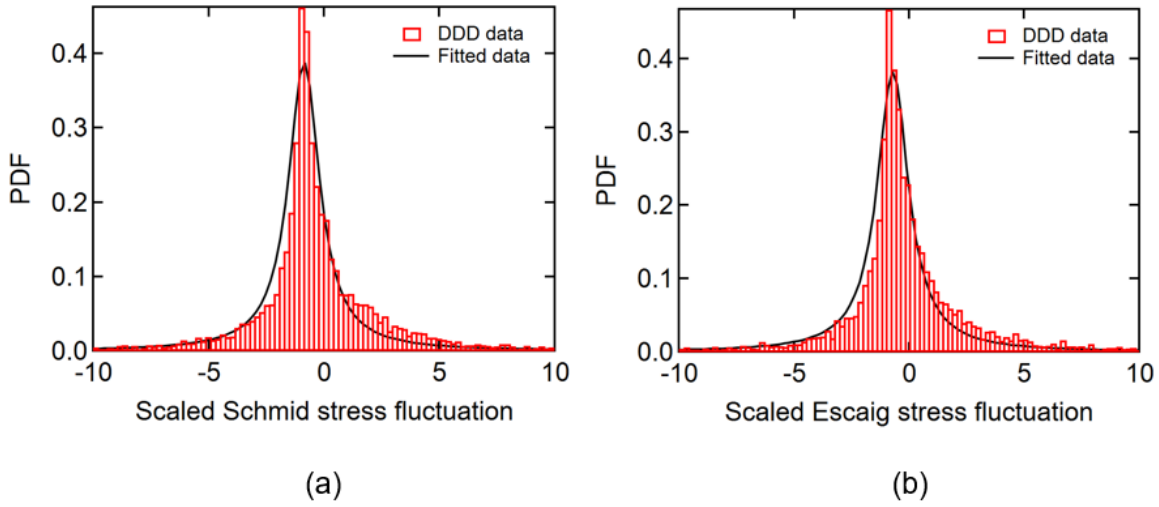

Fig. 5.2. PDF of (a) scaled Schmid stress fluctuation and (b) scaled Escaig stress fluctuation on dislocation points for screw dislocation segments at 0.5% strain. The statistics of both Schmid and Escaig stress fluctuations follow Cauchy distribution.

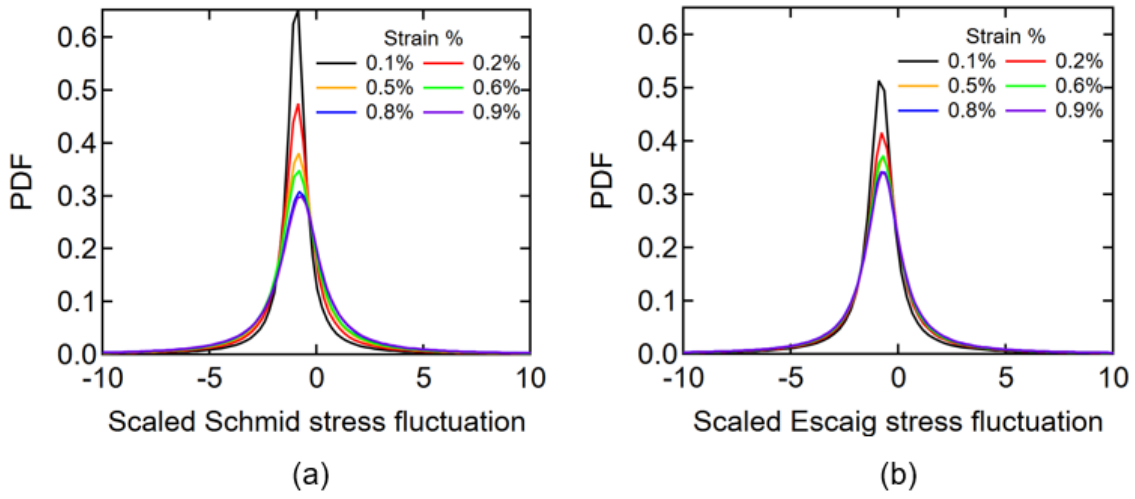

Fig. 5.3. PDF of (a) scaled Schmid stress fluctuation and (b) scaled Escaig stress fluctuation on dislocation points at different strain levels for screw dislocation segments.

Based on the statistics of the screw segment length distribution and scaled stress fluctuations, the cross-slip rate in CDD can then be defined following equation (7) as

$$\dot{r}_{\mathrm{cs}}^{i\to j} = \left\langle \frac{\sum_{m=1}^{N} I_{\mathrm{cs},m}\; l_m}{\sum_{m=1}^{N} l_m} \right\rangle \frac{1}{\Delta t}; \quad I_{\mathrm{cs},m} = \begin{cases} 1 \text{ if } P(l_m) = c l_m \mathrm{e}^{-\frac{E_{\mathrm{act}}}{kT}} > R, \\ 0 \end{cases} \tag{5.11}$$

where l_m corresponds to the length of the m^{th} sampled screw segment, Δt corresponds to the timestep, N corresponds to the number of screw segments in the unit volume, $I_{\mathrm{cs},m}$ is the cross-slip indicator function for the m^{th} screw segment, and R is a random number. The cross-slip indicator function is 1 for the m^{th} segment if the cross-slip probability based on equation (6) is greater than the generated random number else it is zero. The functional expression for the normalization constant and activation energy varies based on the model chosen to characterize the cross-slip process. The activation energy expression (E_{act}) for the three different cross-slip models: Kubin (Devincre et al., 2011; Kubin et al., 1992), Hussein (Hussein et al., 2015) and Malka (Malka-Markovitz et al., 2021) are given below.

$$E_{\mathrm{act}} = -V(|\tau_{\mathrm{s}}^{\mathrm{cs}}| - \tau_{\mathrm{III}}) \text{ (Kubin)}, \tag{5.12}$$

$$E_{\mathrm{act}} = E_{\mathrm{cons}} - V\left(\tau_{\mathrm{e}}^{\mathrm{p}} - \tau_{\mathrm{e}}^{\mathrm{cs}}\right) \text{ (Hussein)}, \tag{5.13}$$

$$E_{\text{act}} = E_{\text{cons}}\left[\frac{G(\tau_{\text{e}}^{\text{p}})}{2} + \frac{G(\tau_{\text{e}}^{\text{cs}})}{2}\left[\tanh(l_{\text{c}}) - \frac{2\zeta_{\text{Ls}} l_{\text{c}} E^*}{1.55} - \frac{\lambda}{1.55G(\tau_{\text{e}}^{\text{cs}})}(\zeta_{\text{Ls}} l_{\text{c}})^3\right]\right] \text{(Malka)}. \quad (5.14)$$

The definitions of the parameters in the above three model equations are given in Table 5.2 below.

Table 5.2. Definitions of symbols in equation (5.12)-(5.14).

Symbols	Definitions	Symbols	Definitions
E_{cons}	Constriction energy	l_{c}	Length of dislocation dissociated into CS plane
V	Activation volume	ζ_{Ls}	Fitting parameter
$G(\tau)$	$\left(1 + \frac{\sqrt{3}b}{6\gamma}\tau\right)^{-1}$	E^*	Offset of interaction energies in glide and cross-slip plane.$\left(\ln\left(\frac{G(\tau_{\text{e}}^{\text{cs}})}{G(\tau_{\text{e}}^{\text{p}})}\right)\right)$
γ	Stacking fault energy	λ	$\frac{1}{6}\left(\frac{b\tau_{\text{s}}^{\text{cs}}}{\gamma}\right)^2$

The Schmid stress and Escaig stress used in these activation energy formulations are the effective stress values on the screw segments after considering the fluctuation stress statistics. For example, in the model by Kubin, the activation energy depends on Schmid stress in the cross-slip plane ($\tau_{\text{s}}^{\text{cs}}$) , whereas in the model by Hussein the activation energy depends on the difference between the Escaig stress on the primary plane ($\tau_{\text{e}}^{\text{p}}$) and cross-slip plane ($\tau_{\text{e}}^{\text{cs}}$). The effective stress for these two models after accounting for stress fluctuation can then be written in the form

$$\tau_{\text{s}}^{\text{cs}} = \bar{\tau}_{\text{s}}^{\text{cs}} * \hat{\tau}_{\text{s}}^{\text{cs}} + \bar{\tau}_{\text{s}}^{\text{cs}}, \quad (5.15)$$

$$\tau_{\text{e}}^{\text{cs}} = \bar{\tau}_{\text{e}}^{\text{cs}} * \hat{\tau}_{\text{e}}^{\text{cs}} + \bar{\tau}_{\text{e}}^{\text{cs}}, \quad (5.16)$$

where $\bar{\tau}_{\text{s}}^{\text{cs}}$ and $\bar{\tau}_{\text{e}}^{\text{cs}}$ correspond to the mean Schmid stress on the cross-slip plane and mean Escaig stress on the cross-slip plane in CDD respectively. $\hat{\tau}_{\text{s}}^{\text{cs}}$ and $\hat{\tau}_{\text{e}}^{\text{cs}}$ correspond to the scaled Schmid and Escaig stress fluctuation variables which can be sampled from the estimated PDF based on equation (5.6).

5.5 Results

In this section, the numerical experiment used to validate the newly proposed cross-slip framework, referred to as CDD cross-slip framework hereafter, is discussed first. This involves comparing the average cross-slip rates obtained using the CDD cross-slip framework and DDD methodology for a given DDD configuration. Following that, the effect of different cross-slip models on the mechanical behavior and dislocation microstructure is studied by performing bulk CDD simulations using different cross-slip models of interest.

5.5.1 Cross-slip rate comparison

The main objective behind developing a new framework for cross-slip modelling in CDD is to capture the cross-slip rates accurately in CDD. Hence, to validate the CDD cross-slip framework a discrete configuration is first sampled from DDD simulation and coarse-grained to obtain a CDD configuration. Based on the CDD configuration, the cross-slip rate is then evaluated using the CDD framework and compared with DDD cross-slip rate. The comparison between the two methods is possible since the cross-slip rate is evaluated for the same dislocation configuration although they are represented differently in DDD and CDD models. The DDD simulation tool used to conduct this experiment is the DDD simulation code microMegas (Devincre et al., 2011). Although, the DDD simulation code uses a cross-slip model that was derived from (Kubin et al., 1992), the DDD cross-slip rate was also evaluated for Hussein and Malka's model for the chosen DDD configuration based on the data regarding screw segment length and stress on the dislocations, which are readily available.

The first step in the cross-slip rate comparison process is converting the chosen DDD configuration into a CDD configuration by performing a coarse graining process. The coarse graining process involves partitioning the domain into small volumes and smearing out the discrete dislocation within each volume to obtain a continuum representation of the discrete configuration. The details regarding the coarse graining procedure can be found in (Vivekanandan et al., 2022). Following the coarse graining procedure, the coarse-grained state variables like dislocation density and coarse grained stress can be estimated for the given DDD configuration which can then be used in the CDD framework to estimate cross-slip rate. The details regarding the slip system nomenclature used in microMegas is mentioned in Table 5.3. The glide plane normal defined in

Table 5.3 is used to define the right handed normal of the loop to which the dislocation segment belongs while estimating the Escaig stress.

Table 5.3. Slip system enumeration for FCC crystals in microMegas

Slip system	1	2	3	4	5	6	7	8	9	10	11	12
Plane	(111)	$(1\bar{1}1)$	$(1\bar{1}1)$	$(11\bar{1})$	$(11\bar{1})$	(111)	$(\bar{1}11)$	$(1\bar{1}1)$	(111)	$(\bar{1}11)$	$(11\bar{1})$	$(\bar{1}11)$
Direction	$[\bar{1}01]$	$[\bar{1}01]$	[011]	[011]	$[\bar{1}10]$	$[\bar{1}10]$	[110]	[110]	$[01\bar{1}]$	$[01\bar{1}]$	[101]	[101]

The average DDD cross-slip rate is estimated based on the equation (5.7) whereas the average CDD cross-slip rate based on the new framework is estimated by equation (5.11). In the case of the former, the length of the discrete screw segment and stress on dislocations from DDD data are used while estimating the cross-slip probability whereas in the case of the latter, the screw segment length is sampled from the exponential distribution based on the coarse grained dislocation density and the effective stress on the dislocations is estimated based on equation (5.15) by sampling values from the Cauchy distribution for scaled Schmid and Escaig stress fluctuations and coarse grained stress. The material parameters used in these simulations are given in Table 5.1.

Fig. 5.4 shows the average cross-slip rate computed for a DDD configuration at 0.5% strain using the CDD cross-slip framework and DDD method for the three cross-slip models. The cross-slip rates for the case of CDD framework are evaluated for 1000 different realizations which were sampled from the stress fluctuation distribution. The mean of those 1000 different instances is denoted by the black '◊' marker along with a bar that indicates the maximum and minimum values in Fig. 5.4. The cross-slip rate obtained using DDD method is represented by the red '○' circle. It is evident from the figure that the cross-slip rates predicted by the CDD framework can take a range of values fixed by the sampled statistics. In addition to that, it can also be observed that the spectrum of cross-slip values spans a wider range for the case of inactive slip systems, denoted by the blue color in Fig. 5.4, compared to the active ones. The reason for this is that the dependence of activation energy on sampled stress fluctuation statistics is more prominent due to the lack of resolved shear stress along the inactive slip systems. Consequently, any changes in the stress fluctuations affect the cross-slip rate more significantly in the case of inactive slip systems

compared to active slip systems. Furthermore, comparing the CDD cross-slip rates with DDD cross-slip rates for all three models, it can be observed that in most of the cases the DDD values lie within the spectrum of CDD values. This indicates that the CDD model is indeed able to capture the cross-slip behavior in DDD based on the mean field variables and DDD statistics. A better agreement between the two methods can be expected when an ensemble of DDD configuration at the same strain level is sampled from multiple DDD simulations so that different possible local states are explored, which can then be averaged to compare the results from CDD.

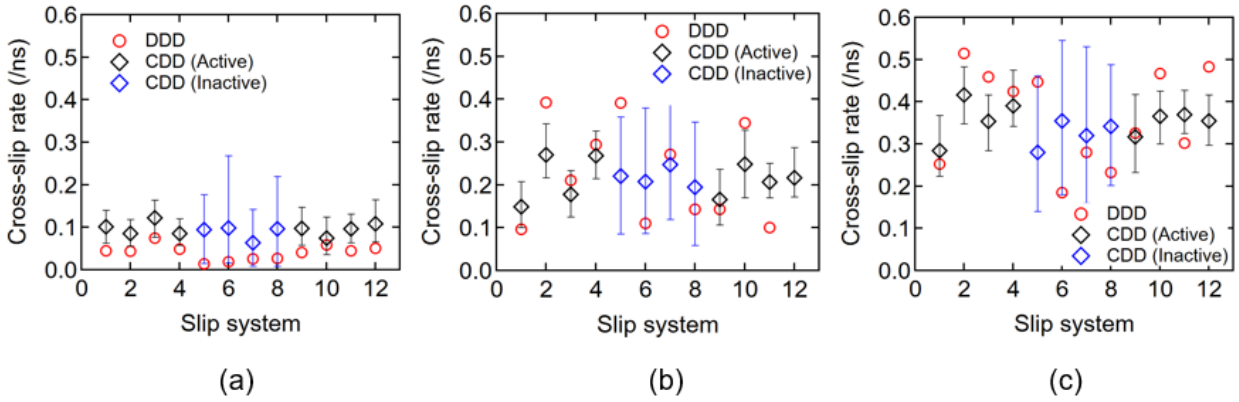

Fig. 5.4. Average cross-slip rate computed using (a) Kubin, (b) Hussein and (c) Malka's model based on DDD and CDD framework for a DDD configuration sampled at 0.5% strain.

Comparing the cross-slip rates given in Fig. 5.4 among the three different models shows that Malka's model yields the highest cross-slip rate whereas Kubin's model has the lowest cross-slip rate. The difference in the cross-slip rates between the three models can be attributed to the stress components considered in the activation energy expression as well as the parameters used to calibrate the model. For instance, the Kubin's model considers only the Schmid stress along the cross-slip plane to determine the cross-slip activation energy barrier, which was shown to have the least effect on reducing the cross-slip activation energy compared to other stress components (Kang et al., 2014). Consequently, one can expect it to have the lowest cross-slip rates amongst other models. Additionally, since Kubin's model was calibrated based on the cross-slip activity at the beginning of stage III hardening, high stress levels are required to initiate cross-slip compared to other models which does not have such limitations. Similarly, Hussein's model considers the cross-slip activation energy to be linearly dependent on the difference between the Escaig stresses on the primary and cross-slip plane. According to this model, cross-slip is never possible when Escaig

stress on the cross-slip plane is higher compared to that of the primary plane. However, the line tension model by (Malka-Markovitz and Mordehai, 2019) showed that when the effect of Schmid stress on the cross-slip plane is considered, cross-slip is possible even though the Escaig stress on the cross-slip plane is higher compared to that of the primary plane. Since Malka's model considers the effect of all stress components the chances for a dislocation to cross-slip is higher in their model compared to the other two models, which is evident from Fig. 5.4.

5.5.2 Effect of different cross-slip models on bulk CDD simulations

The aim of this section is to study the effect of different cross-slip activation energy formulations on the mechanical response of the dislocation system and the dislocation microstructure evolution. Hence, CDD simulations using Kubin's model (Kubin et al., 1992), Hussein's model (Hussein et al., 2015) and Malka's model (Malka-Markovitz et al., 2021) were performed based on the new framework for the monotonic loading case. All simulations were performed using the material properties listed in Table 5.1.

The simulation domain size in these simulations is 5μm × 5μm × 5.303μm and the applied strain rate is $20s^{-1}$ along [001] direction. The slip plane normal and Burgers vectors of all the slip systems for a FCC crystal in CDD is given in Table 5.4. The initial dislocation configuration was made up of 10 circular dislocation loops with radius ranging from 2μm and 5μm in each slip system. The initial total dislocation density used in these simulations is $1.5 \times 10^{12}\ m^{-2}$.

Table 5.4. Slip system enumeration for FCC crystals in CDD

Slip system	1	2	3	4	5	6	7	8	9	10	11	12
Plane	(111)	$(\bar{1}11)$	$(\bar{1}11)$	$(11\bar{1})$	$(11\bar{1})$	$(1\bar{1}1)$	$(1\bar{1}1)$	(111)	(111)	$(11\bar{1})$	$(\bar{1}11)$	$(1\bar{1}1)$
Direction	$[0\bar{1}1]$	$[0\bar{1}1]$	[101]	[101]	[011]	[011]	$[\bar{1}01]$	$[\bar{1}01]$	$[\bar{1}10]$	$[\bar{1}10]$	[110]	[110]

Fig. 5.5(a) shows the average cross-slip rate, $\dot{r}_{cs}^{1\to2}$, defined in equation (5.11) for slip system 1 for the three models obtained by averaging the cross-slip rate throughout the CDD simulation domain. The average cross-slip rate obtained from the Kubin's model is significantly less compared to that of Hussein and Malka's models. This can be attributed to the origins of

Kubin's model, which was discussed in the previous section. Fig. 5.5(b) shows the average cross-slip rate $\dot{r}_{cs}^{2\to1}$ for slip system 2, which is the collinear slip system of 1, for all three models. Comparing Figs. 5.5(a) and 5.5(b), it can be observed that the average cross-slip rates of collinear slip systems are similar for both Kubin and Malka's model, but the behavior is markedly different for the case of Hussein's model. The difference in behavior for the case of Hussein's model stems from the bias which the activation energy expression enforces on the cross-slip probability. Since the activation energy depends on the difference between Escaig stress in both the glide and cross-slip plane, as can be seen from equation (5.14), it is expected that if cross-slip is favorable from slip system 1 to slip system 2 at a point, then cross-slip from slip system 2 to 1 would be less favorable.

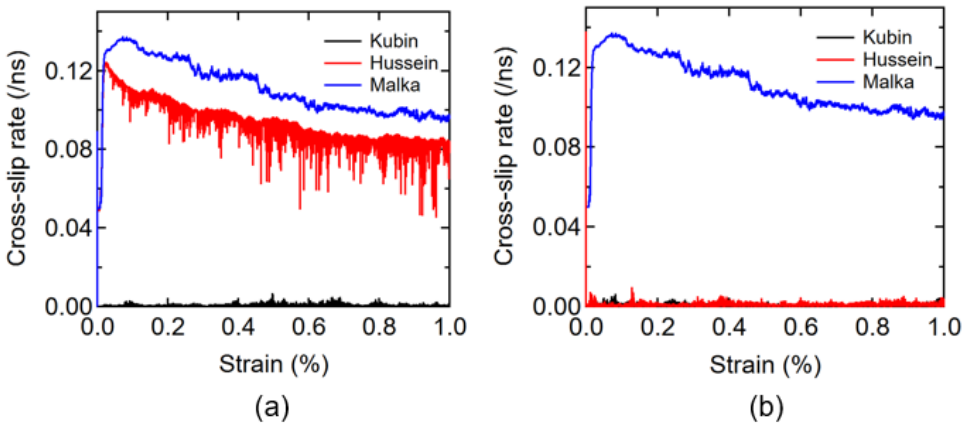

Fig. 5.5. Average cross-slip rates of (a) slip system 1 and (b) slip system 2 for three different models in CDD simulation.

Figs. 5.6(a) and (b) show the stress-strain curves and dislocation density evolution curves of all the three models, respectively. The results of the simulation in which cross-slip was not considered is also shown for reference to emphasize the impact of cross-slip on the stress-strain response and dislocation density evolution. The stress-strain response in Fig. 5.6(a) shows that there is a difference in the stress at which yielding occurs and the rate of hardening between different models, although it is minimal. Comparing Fig. 5.5 and 5.6 shows that the models with higher cross-slip rates have lower yield stress and higher rate of hardening. This can be explained by observing Fig. 5.6(b) which shows that for models with higher cross-slip rate dislocation density initially evolves slower and then starts to grow faster. Consequently, we observe for

models with higher cross-slip rate, the yield stress is lower due to fewer dislocations and the rate of hardening is higher due to faster increase in dislocation density. It is worth mentioning that the Kubin's model has negligible cross-slip throughout the simulation time except at the very early stage. Hence, the rate of hardening is similar for Kubin's model and the simulation where cross-slip was not considered but there is a difference in yield point between the two due to the cross-slip activity in Kubin's model in the early stages.

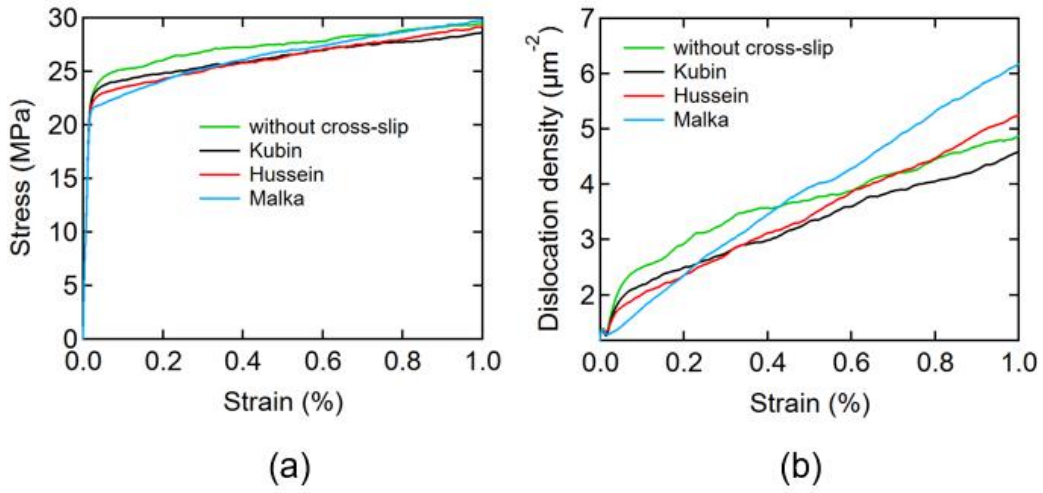

Fig. 5.6. (a) Stress-strain curves and (b) total dislocation density curves obtained from CDD simulation for the three different models.

Fig. 5.7 shows the slip system dislocation density evolution for all three models. As expected, the dislocation density for an active slip system (SS 1-8) evolves faster compared to the inactive slip system (SS 9-12) in all cases. But in the case of Hussein's model, a qualitative difference in the slip system density behavior is observed compared to other two models. The active slip systems evolve as two separate groups as can be seen in Fig. 5.7(b) as opposed to one in the other cases. This is due to the discrepancy in the cross-slip rates, which was shown in Fig. 5.5, because of which active slip systems with higher cross-slip rates evolved slower compared to their collinear counterparts since more dislocations were transferred to their collinear counterpart from them rather than to them. It is important to note that the same effect is not observed in the case of inactive slip systems since the dislocation density increase in these cases mainly comes from the glissile junction interaction between the active slip systems.

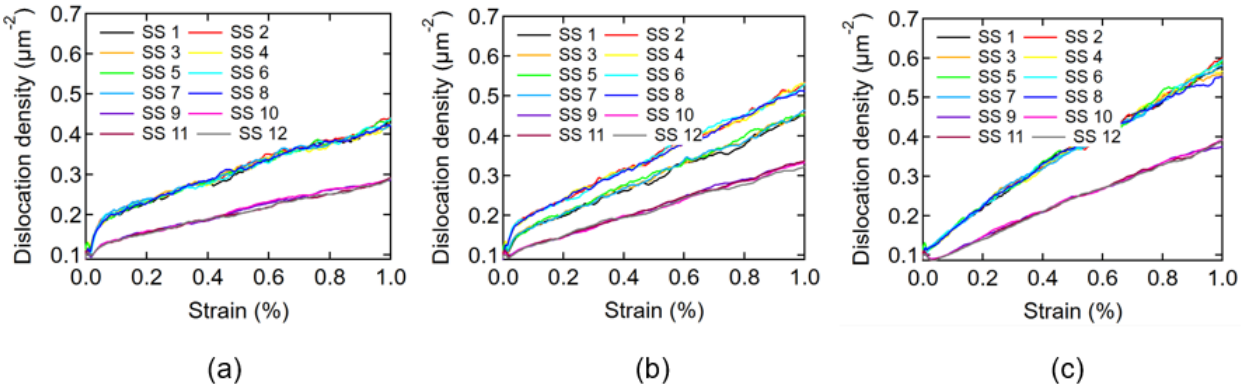

Fig. 5.7. Slip system dislocation density curves of simulations (a) based on Kubin's model (b) based on Hussein's model, (c) based on Malka's model.

5.5.3 A dislocation relaxation experiment

A relaxation experiment was performed wherein the dislocation configuration is loaded to a strain level of 0.25% in a single time step, at a strain rate of the order $10^6\ s^{-1}$ along [001] direction and then allowed to relax. Loading the simulation domain to 0.25% strain in a single time step results in high stress levels since the applied strain gets converted mostly to elastic strain as the dislocations do not have enough time to move. Once the high stress is induced in the domain, the system is then allowed to relax by maintaining the mean strain at 0.25% subjected to periodic boundary conditions. This approach was chosen to study the dislocation microstructure evolution at high stress levels because accessing such stress values through typical monotonic loading simulations is near impossible due to the computational constraints and strain levels required to reach such stresses.

The relaxation experiment described above was conducted for the three cross-slip models along [001] orientation. The simulation box size used in this simulation was $2.5\mu m \times 2.5\mu m \times 2.75\mu m$ and the initial dislocation density was chosen to be $3 \times 10^{14}\ \mu m^{-2}$. The initial dislocation configuration was made up of 10 circular dislocation loops with radii ranging from $2\mu m$ and $3\mu m$ in each slip system. The material parameters used in these simulations are listed in Table 5.1.

Fig. 5.8 shows the stress-time curve and dislocation density behavior over the course of the relaxation experiment. The initial steep increase in stress in Fig. 5.8(a) corresponds to the applied load stored as elastic strain in the simulation domain. With the progression of time, the stress in the simulation domain reduces due to the relaxation and then reaches a stable state eventually for all three models. Fig. 5.8(b) shows the dislocation density evolution with time for the three models.

The dislocation density decreases asymptotically due to the dislocation annihilation that happens during the relaxation tending towards a stable state for all three models.

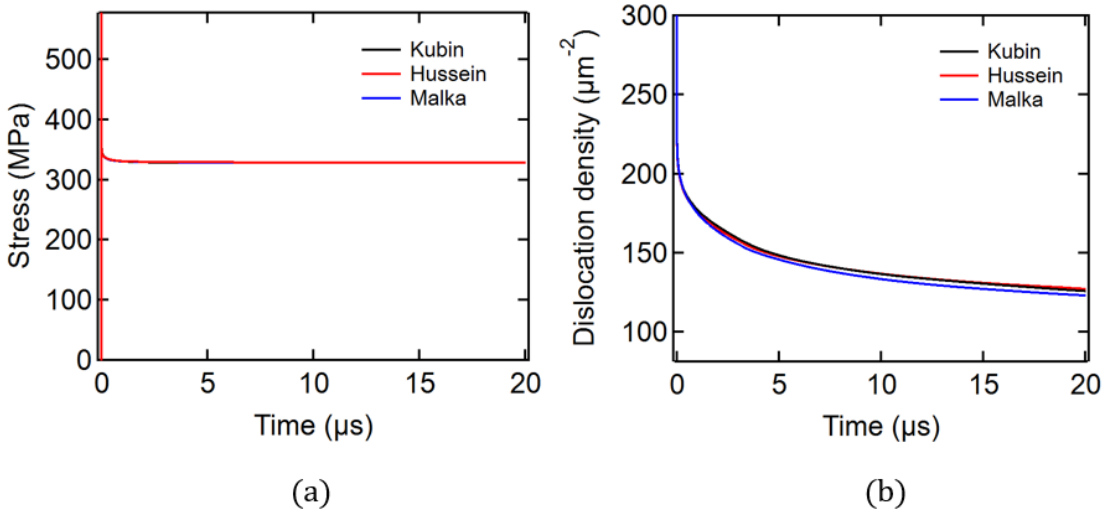

Fig. 5.8. (a) Stress-strain curve and (b) total dislocation density evolution curve of the relaxation experiment.

Fig. 5.9 and 5.10 shows the dislocation microstructure obtained from the relaxation experiment for all the three models by visualizing the scalar dislocation density after applying the threshold filter over the whole simulation domain and along (010) plane respectively. The threshold filter assigns a color, in this case black or white, based on the dislocation density value at a given point. For the Figs. 5.9 and 5.10, if the dislocation density value at a point is greater than 175 μm^{-2}, then the color black was assigned else the color white was assigned. After applying the threshold filter, the cell-type structures are observed along the planes (110) and (010), as observed in experiments (Ungar et al., 1984).

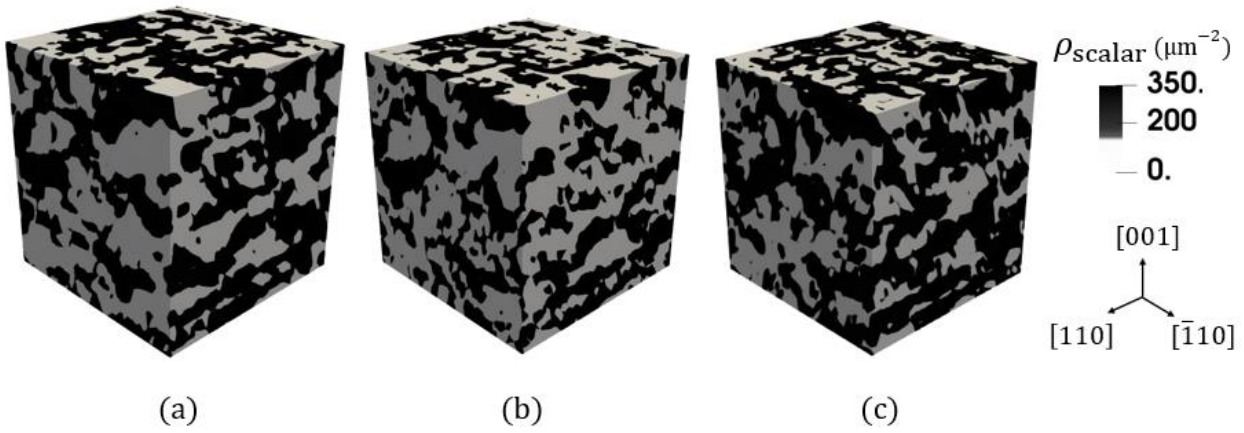

Fig. 5.9. Dislocation microstructure obtained from the CDD relaxation experiment by visualizing the scalar dislocation density after applying the threshold filter using (a) Kubin's model, (b) Hussein's model and (c) Malka's model for modeling cross-slip process. The threshold filter has been applied to accentuate the features present in the image.

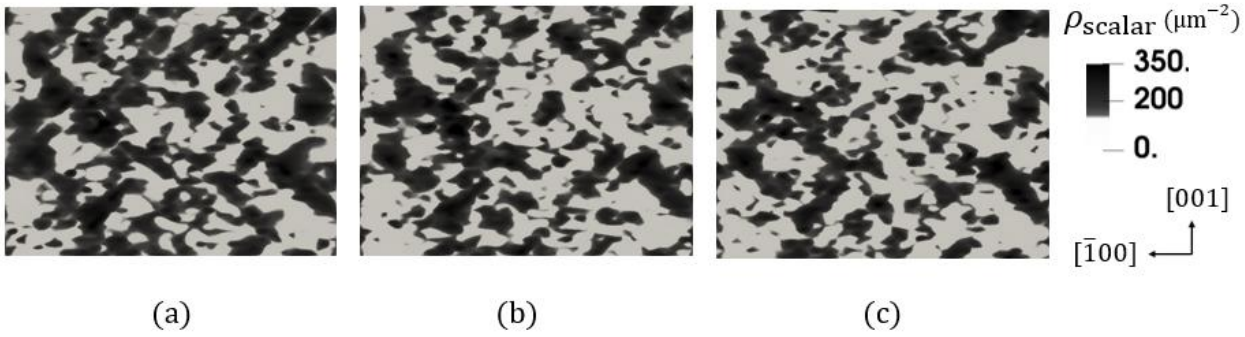

Fig. 5.10. Dislocation microstructure from the CDD relaxation experiment along (010) plane obtained by visualizing the scalar dislocation density after applying the threshold filter using (a) Kubin's model, (b) Hussein's model and (c) Malka's model for modelling cross-slip process. The threshold filter has been applied to accentuate the features present in the image.

To quantify the similarities and differences between dislocation microstructures predicted by CDD for the three cross-slip models of interest, autocorrelations of the 2D dislocation microstructure images in Fig. 5.10 were computed and compared. These autocorrelations were computed for single cross-sections of the simulation volume from the filtered data using FFT algorithm (Frigo, 1999). Fig. 5.11 (a), (b) and (c) shows the autocorrelation for the corresponding three images in Fig. 5.10. The autocorrelations of these images characterize the probability of finding dislocations at a prescribed distance and direction from a randomly placed point on the image. The X and Y axis in the images represent the distance in nm and the color bar captures the

probability. All the three images show a bright red spot with the highest probability at the center and the probability decreases uniformly along all directions approximately which is evident from the gradual change in the color as one goes away from the center. Fig. 5.11(d) shows the radial pair correlation function for all three dislocation microstructure images in Fig. 5.10 obtained using MATLAB (Gavagnin et al., 2018), which decreases with increase in radial distance till it reaches a minimum and then rises again before becoming a constant for all three models. It is evident from the figures that the dislocation microstructure morphology of all three models is very similar as all the models follow the same trend.

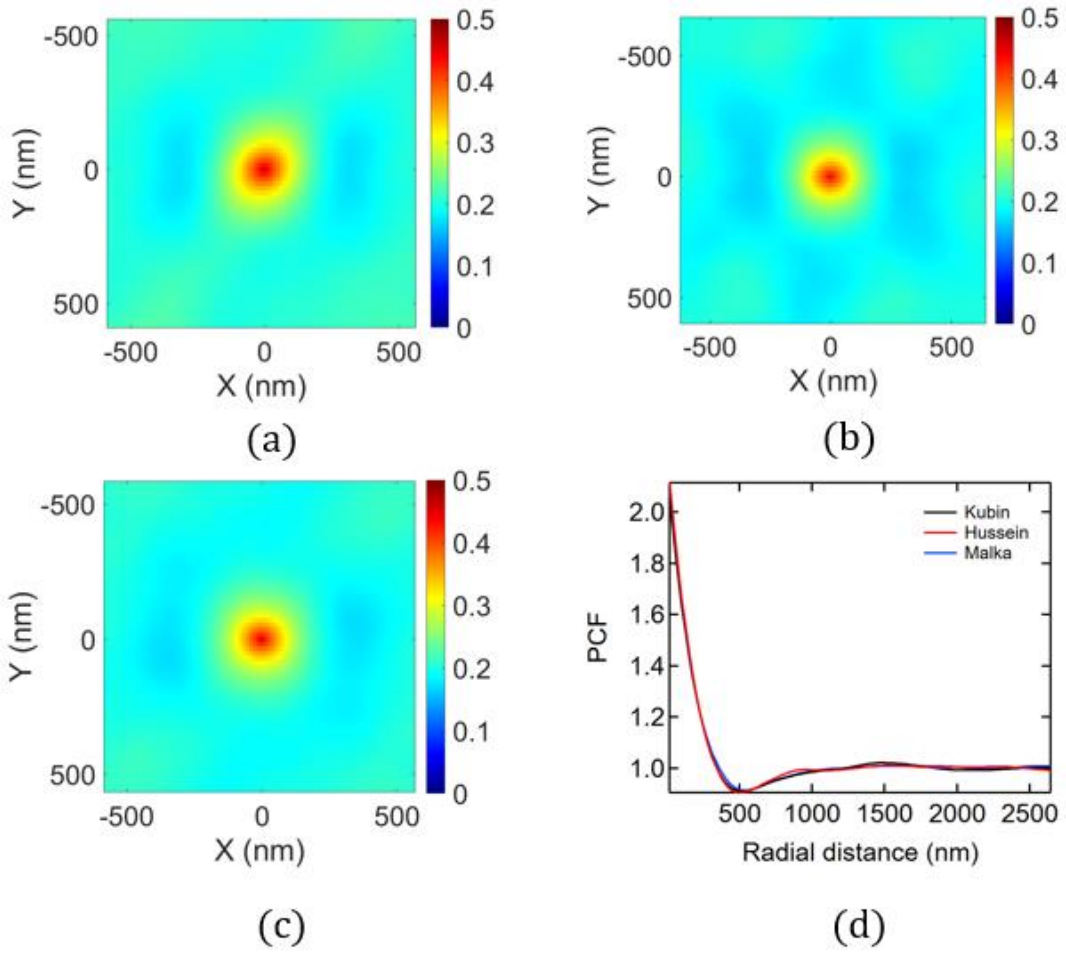

Fig. 5.11. Spatial autocorrelation of dislocation microstructure in Fig. 5.10 obtained using FFT algorithm (Frigo, 1999) for (a) Kubin's model, (b) Hussein's model and (c) Malka's model. (d) Radial pair correlation function for all three models.

5.6 Discussion

The results presented in the previous section highlight the capability of the new CDD cross-slip framework which represents an improvement over the other existing approaches used to model cross-slip in CDD. The cross slip modeling approach proposed here incorporates the information about local coarse grained stress, dislocation density, the screw segment length statistics, and stress fluctuation statistics, thus allowing to overcome the shortcomings of other approaches used to capture the cross-slip process in CDD (Deng and El-Azab, 2010; Sudmanns et al., 2019; Xia et al., 2016). For instance, in the works of (Deng and El-Azab, 2010; Xia et al., 2016), the cross-slip rate was estimated by sampling the averaged cross-slip rate time series data from DDD simulation after performing time coarse graining analysis. Although, this approach made use of the cross-slip statistics from DDD, it was averaged over the simulation domain thereby ignoring the effects of the local stress and its fluctuations. This issue was addressed in the proposed model by making use of the local stress and dislocation density information, which was used to sample DDD statistics like screw segment length and stress fluctuation statistics to estimate the cross-slip rate. Likewise, the work of (Sudmanns et al., 2019) estimated the cross-slip rate by using the local coarse grained stress directly in the DDD cross-slip probability expression (Kubin et al., 1992), without incorporating the effects of local dislocation arrangement which was shown to result in the markedly different local stress states (Vivekanandan et al., 2022). The new CDD cross-slip framework addressed this issue by making use of the screw segment length statistics and the stress fluctuation statistics from DDD which captures the different possible underlying local state for a given coarse grained description.

For most of the cases, these statistics can be readily extracted from DDD simulations. But in some cases, running DDD simulations to the required strain level or total dislocation density might not be feasible due to the computational limitations. In such cases, two different approaches can be adopted to resolve the issue. One possible option is to use a data science approach, where the statistics extracted from simulations at smaller strain levels or lower dislocation density can be used to determine the values at the required strain levels or dislocation density via extrapolation. Since the simulations would be performed at smaller strain levels and lower dislocation density, this approach would reduce the time required to collect data from multiple DDD simulations, which can then be used to ascertain a reasonably accurate trend for the statistics of interest. The other option is to estimate these statistics in terms of dislocation-dislocation correlation, which is

typically used to capture the information lost due to coarse graining process, from DDD simulations at smaller strain levels and domain size (Groma, 1997). The advantage of using spatial correlations to estimate these statistics is that it varies weakly with plastic strain and total dislocation density (Anderson and El-Azab, 2021), thereby allowing us to use the same information at all strain levels and total dislocation density. Preliminary work has been done in the above mentioned research paper to show how the spatial correlation information can be incorporated in CDD. Therefore, the proposed framework in CDD can be used as a tool to explore domains above and beyond the computational capabilities of DDD with minimal assumptions in the model.

The validity of the newly proposed cross-slip modeling approach was tested by comparing the cross-slip rate estimated using CDD and DDD methodology for a chosen DDD configuration. Cross-slip rate estimated using DDD methodology made use of the stress on the screw dislocations and screw segment length whereas the cross-slip rate obtained by using the CDD formalism used the coarse-grained stress and dislocation density in addition to the values sampled from DDD statistics like the screw segment length and stress fluctuation distribution. The sampled values correspond to one of the many possible configurations of the ensemble and hence it is indeed expected that the estimated cross-slip rate will vary along a spectrum and will not be an accurate match to the actual cross-slip rate. Nevertheless, Fig. 5.4 showed that CDD cross-slip rate estimated using the new framework is within reasonable limits of DDD cross-slip rate for all three models. For an accurate comparison between the two methods, a set of DDD configurations should be sampled from multiple DDD simulations such that different local configurations for a given strain level can be accounted for during cross-slip rate estimation. The average cross-slip rate of the ensemble can then be used to compare with the average of CDD cross-slip rates that were obtained by sampling statistics from the screw segment length and stress fluctuation distribution. Currently, results from a single DDD configuration was deemed sufficient to demonstrate the workings of the framework based on the assumption that the dislocation system is spatially ergodic (Deng and El-Azab, 2010, 2009), which implies the volume average of statistical quantities is same as the ensemble average. Therefore, in this work volume average statistical quantities from a single dislocation configuration were only used to make the comparison.

The effect of different cross-slip activation energy formulations on the mechanical behavior and dislocation microstructure was investigated in this work. It was shown that the different cross-

slip activation energy formulations indeed resulted in different average cross-slip rates, but the effect of the different cross-slip rates on the stress-strain response and dislocation density evolution was shown to be minimal in Fig. 5.6 and 5.7. A plausible explanation for this behavior is the nature of the loading orientation, which is [001] loading orientation and type of loading used in the simulations, which is monotonic loading and cross-slip rates of collinear slip systems. The [001] loading orientation activates 8 slip systems comprising 4 pairs of collinear slip systems sharing the same Burgers vector for FCC crystal such that they all have the same Schmid factor. Similarly, the remaining 4 inactive slip systems comprising of 2 pairs of inactive slip systems also have the same Schmid factor. Hence, for the case where the loading is monotonic and collinear slip systems having similar cross-slip rates, one can expect dislocations evolving in a similar manner despite different cross-slip rates due to the dominance of the applied component of the Schmid stress. Consequently, the difference in the stress-strain response can also be expected to follow similar trend for models with different cross-slip rates. The relaxation experiment which was devised to study how dislocations reorganize themselves at higher stress levels and dislocation density also yielded similar stress-strain and dislocation density evolution behavior for all three models. With regard to the collective behavior of dislocations, the difference between the three models in this case was almost non-existent compared to the monotonic case indicating that at higher stresses, the differences between the models become insignificant. Finally, despite subjecting the dislocation system to a high strain rate loading before relaxation, the dislocation microstructure showed cell-like type structure typically observed in monotonic simulation for all three models.

5.7 Conclusion

A data driven approach to model cross-slip behavior in CDD was proposed. The model made use of the screw segment length distribution and stress fluctuation statistics from DDD to inform CDD model about the essential information required for cross-slip modelling which was lost due to coarse graining. It was shown that the screw segment distribution in DDD follows the exponential distribution and the stress fluctuation statistics for screw segments follows the Cauchy distribution. Using these statistics from DDD, it was shown that the average cross-slip rate over the whole domain obtained using the new framework was able to match the DDD cross-slip rate. In addition, the effect of different activation energy formulations on the stress-strain response, dislocation density evolution and dislocation microstructure were studied. It was found that,

although the average cross-slip rates of the different cross-slip activation energies were different, the effect on stress-strain response and dislocation density evolution were minimal. Furthermore, it was shown that in the presence of high local stress and dislocation density, the new CDD framework was able to capture the dislocation self-organization in cell-like structure typically observed along the {100} and {110} type planes in experiments.

6. DISLOCATION MICROSTRUCTURE PREDICTION USING CDD DURING CYCLIC LOADING

6.1 Introduction

Fatigue-induced failure and crack initiation have been longstanding concerns in structural materials and engineering applications. The formation of unique dislocation microstructures during cyclic loading plays a crucial role in these failure mechanisms. Observations in the early 1900s by Ewing and Humfrey (1903) highlighted the emergence of fatigue-induced slip bands that eventually lead to crack initiation. Subsequent experimental studies (Gong et al., 1997a; Jin, 1989; Li et al., 2011; Mughrabi, 1983) have revealed various other dislocation patterns, including persistent slip bands (PSBs), labyrinth structures, cell structures, and vein-like structures. These dislocation microstructures significantly influence the mechanical response of the material, emphasizing the need to develop predictive methods to understand and prevent catastrophic failures.

To investigate the formation of dislocation microstructures during cyclic loading, numerous theories have been proposed in the literature (Gong et al., 1997a; Li et al., 2011; Mughrabi, 1983; Sauzay and Kubin, 2011). However, the complex dynamic multi-scale nature and time scale of these processes have hindered the development of a comprehensive and predictive computational framework for understanding dislocation microstructures. While experimental techniques such as transmission electron microscopy (TEM) and scanning electron microscopy (SEM) provide valuable insights into the spatial distribution and characteristics of dislocations, they have limitations in capturing the dynamic evolution of dislocation patterns over multiple loading cycles. Computational modeling approaches, including discrete dislocation dynamics (DDD) (Akhondzadeh et al., 2020; Po et al., 2014; Sills et al., 2018; Stricker et al., 2018) and crystal plasticity models (Grilli et al., 2018; Roters et al., 2019), have been employed to study dislocation behavior during fatigue loading. Although these models offer valuable insights, they often face scalability and computational efficiency challenges when simulating large-scale systems over multiple cycles.

In this study, we propose the use of vector based continuum dislocation dynamics (CDD) models (Vivekanandan et al., 2021) to enable the investigation of dislocation patterns and their evolution at the mesoscale. By considering the density and transport of dislocations within a

continuous framework, CDD models offer a promising approach to predict dislocation microstructures during cyclic loading. Theoretical frameworks based on CDD developed in the previous sections can capture essential features of dislocation dynamics, including dislocation transport, reactions, and their interaction with external stress fields. Therefore, this study aims to contribute to the understanding of dislocation microstructure formation during cyclic loading at small strains using our CDD model. By investigating the evolution of dislocation patterns over multiple cycles, we can gain valuable insights into the mechanisms governing the formation of specific microstructure features. These insights will lay a foundation for future predictive modeling of fatigue behavior and aid in the design of materials with enhanced fatigue resistance and durability.

6.2 Simulation results

In this section, the CDD framework described in (Vivekanandan et al., 2021) is used to simulate the cyclic loading behavior. An initial dislocation density of $1.5\times10^{12}\mu m^{-2}$ is distributed across all slip systems randomly and the crystal is loaded along [001] direction with a strain rate of $20s^{-1}$ and strain amplitude of 0.15%. The simulation domain size used is 5μm×5μm×5.303μm and the material parameters used in this simulation are listed in Table 6.1.

Table 6.1. Simulation parameters used for the cyclic loading simulation.

Parameter	Value
Strain rate	$20s^{-1}$
Youngs Modulus	112.5GPa
Poisson's ratio	0.34
Initial dislocation density	$1.5\times10^{12}m^{-2}$
Burgers Vector	0.25525nm
Drag coefficient	5.5×10^{-5}Pas

The stress-strain curve and stress-plastic strain curve, presented in Fig. 6.1, exhibit the characteristic hysteresis behavior commonly observed in cyclic loading experiments. The increase

in flow stress with an increasing number of cycles indicates a progressive hardening of the crystal during the simulation. This hardening effect can be attributed to the continuous increase in dislocation density, as shown in Fig. 6.2. Within a single cycle, the dislocation density initially increases during the tensile phase until reaching a strain of 0.15%, then decreases during the load reversal due to dislocation annihilation, and finally increases again during the compression phase until the total strain reaches 0.15% and the process repeats for the other half of the cycle. Although the dislocation density exhibits fluctuations throughout a single cycle, the average dislocation density at the end of the cycle is higher than at the start. This overall increase in dislocation density arises from the fact that dislocations do not follow the same paths during load reversal due to changes in the local stress state. Fig. 6.2(b) provides insight into the evolution of dislocation density on individual slip systems, revealing that the density increases more rapidly on the 8 active slip systems compared to the 4 inactive slip systems, owing to the external applied load. Furthermore, the figure demonstrates that dislocation density also increases on the inactive slip systems during cyclic loading, indicating the interaction of dislocations among the active slip systems leading to the formation of glissile junctions in the inactive slip systems.

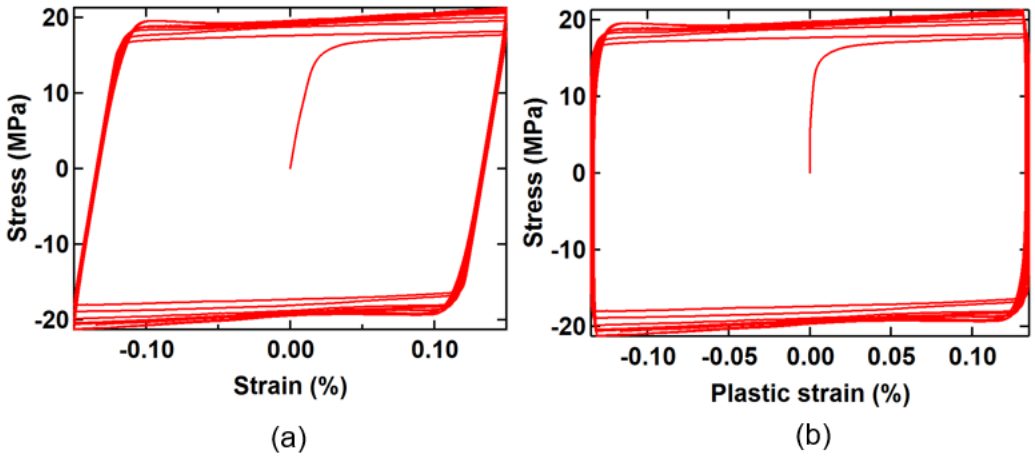

Fig. 6.1. (a) Stress vs total strain curve and (b) Stress vs plastic strain curve. The hysteresis behavior typically observed in cyclic loading experiments is demonstrated using CDD simulation results.

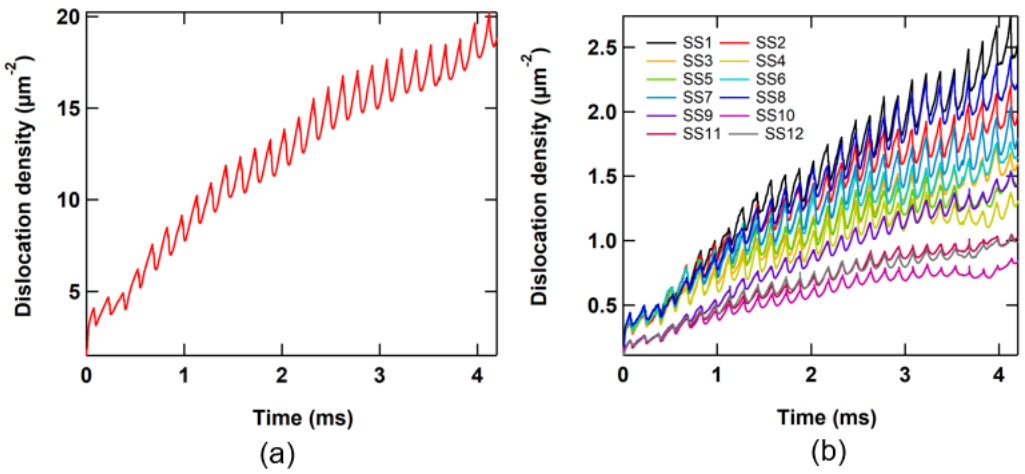

Fig. 6.2. (a) Total dislocation density evolution vs time and (b) Slip system dislocation density evolution vs time.

The evolution of dislocation morphology during a single cycle's early stages is visualized in Fig. 6.3 and Fig. 6.4, representing the scalar dislocation density across all slip systems on the (111) and (010) planes, respectively. These figures highlight the constant rearrangement of the dislocation microstructure from the tensile phase to the zero-stress phase and the compression phase.

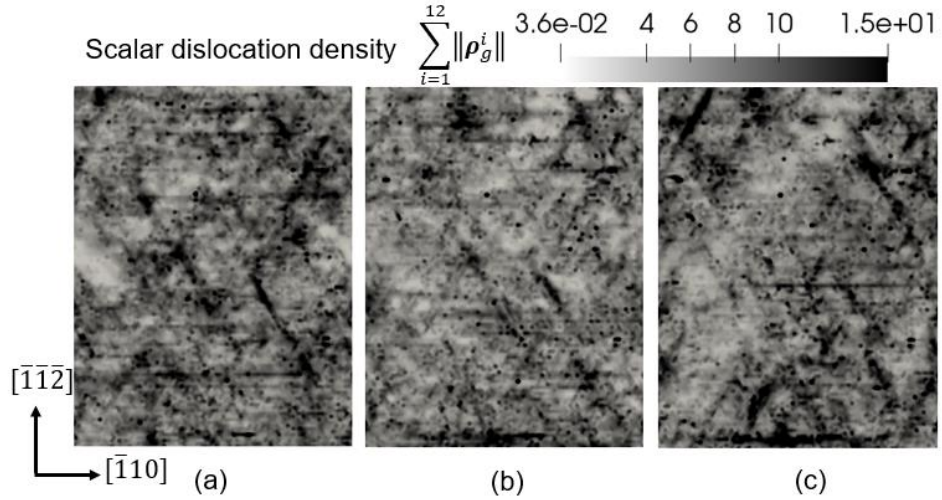

Fig. 6.3. Dislocation microstructure along (111) plane during various stages of a single cycle – (a) Tension, (b) Zero stress and (c) Compression.

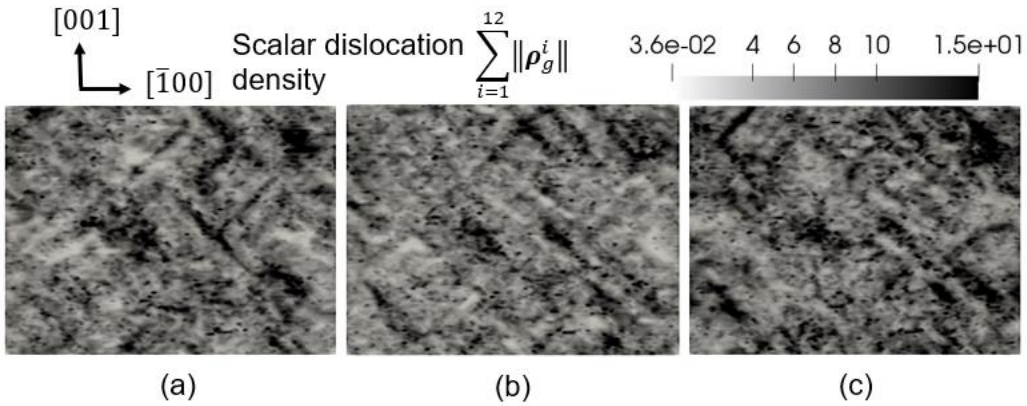

Fig. 6.4. Dislocation microstructure along (010) plane during various stages of a single cycle – (a) Tension, (b) Zero stress and (c) Compression.

Additionally, the dislocation character of the microstructure morphology is evaluated by visualizing the total dislocation density alongside the scalar screw dislocation density and edge dislocation density after 5 cycles, as shown in Fig. 6.5. The results indicate that the prominent features observed in Fig. 6.5(a) predominantly possess an edge character, as evidenced by the significant overlap between the dislocation-rich regions in Fig. 6.5(a) and (b). Therefore, it can be concluded that the dislocation-rich regions mainly comprise edge dislocations.

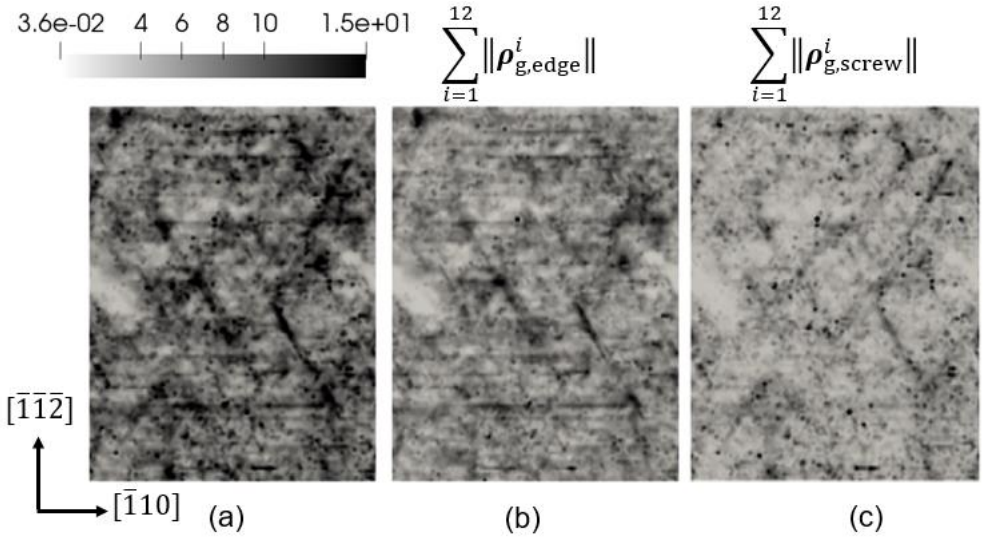

Fig. 6.5. Dislocation microstructure along (111) plane after 5 cycles visualized in terms of – (a) Total dislocation density, (b) Edge dislocation density and (c) Screw dislocation density.

During the initial stages of cyclic loading, prominent features in the dislocation microstructure morphology are not apparent due to the constant rearrangement of dislocations during load reversal. However, as the number of cycles progresses, the dislocation-rich regions become more stable due to forest hardening and grow as other dislocations interact with them. Consequently, more pronounced patterns in the dislocation morphology start to emerge, as observed in Fig. 6.6. This figure presents the dislocation morphology visualized in terms of the scalar dislocation density along the (111) and (010) planes after 20 cycles. Notably, prominent vein-like patterns along the (111) plane and labyrinth-like patterns along the (010) plane become apparent upon observation.

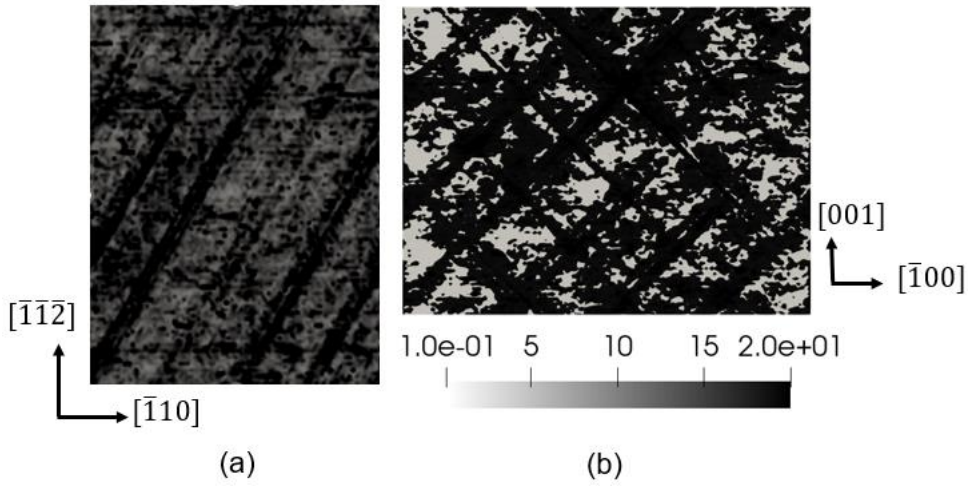

Fig. 6.6. Dislocation microstructure after 20 cycles visualized in terms of total dislocation density, along (a) (111) plane and (b) (010) plane.

6.3 Discussion

The results obtained from the CDD simulations shed light on the formation of dislocation microstructure patterns during cyclic loading at small strains. Within a single cycle, dislocations change their slip direction in response to the applied external load. This leads to interactions between dislocations that were formed during the tensile phase and those retracing their path during the compressive phase, resulting in dislocation annihilation. As a result, the microstructure features observed in the early stages of the cycle are not very pronounced, as shown in Fig. 6.3 and Fig. 6.4.

However, as the number of cycles increases, regions with high dislocation density begin to stabilize, becoming less susceptible to load reversal. These regions require a higher flow stress to move, rendering them immobile. Consequently, plastic slip occurs in the surrounding regions to accommodate the applied load. During this process, dislocations from the surrounding regions interact with the dislocation-rich regions and become embedded within them, further increasing their size.

Prominent features in the dislocation microstructure patterns start to emerge after approximately 20 cycles, as depicted in Fig. 6.6. The vein-like structure observed along the (111) plane is a common feature observed in experiments at smaller plastic strain amplitudes during the early stages of cyclic loading (Gong et al., 1997b). On the other hand, the labyrinth-type structure is typically observed in cyclic loading along the [001] direction, specifically during saturation regimes and at higher plastic strain amplitudes (Li et al., 2011).

A closer examination of Fig. 6.6(b) reveals some distinctions between the simulated pattern and the labyrinth-type structure observed in experiments. In our simulation, the pattern exhibits walls oriented along the <110> direction, whereas the walls of the labyrinth-type structure in experiments are oriented along the <100> direction (Li et al., 2011). Additionally, the ladders present between the walls of the labyrinth-type structure in experiments, which are a part of Persistent Slip Bands (PSBs), are not observed in our CDD simulation. The theories proposed by Li et al. (2011) suggest that the labyrinth-type structure results from the reaction between the ladders of PSBs along the <110> direction, leading to the formation of wall-type structures along the <100> direction. This is consistent with the observation of ladders between the walls of the labyrinth-type structure. Since our simulation was conducted for a low strain amplitude scenario upto 20 cycles, we cannot expect to observe the formation of PSBs, as they are typically observed in saturated regimes with higher strain amplitude cases. Therefore, the labyrinth-type structure observed in experiments is not observed in our CDD simulations. However, with enough cycles and higher strain amplitudes, it is expected that the dislocation microstructure from our simulation would eventually transform into PSBs, which would then interact to result in the formation of a labyrinth-type structure.

6.4 Conclusion

In this section, we utilized the CDD model to investigate the behavior of cyclic loading at small strains. The simulation results successfully captured the characteristic hysteresis behavior observed in experiments, as evidenced by the stress-strain curves. Moreover, the simulations provided insights into the evolution of dislocation density throughout the cyclic loading process.

The results demonstrated that the dislocation density exhibited fluctuations during each cycle but, on average, increased with the progression of cumulative strain. This phenomenon led to cyclic hardening behavior, wherein the flow stress progressively increased to overcome the resistance imposed by the growing dislocation density.

Furthermore, the simulation results shed light on the transient nature of dislocation microstructure features within a single cycle, particularly in the early stages. However, after 20 cycles, distinct dislocation patterns emerged. Specifically, a vein-like structure along the (111) plane and a labyrinth-like structure along the (010) plane was observed.

These findings highlight the capability of the CDD model to capture the cyclic loading behavior at small strains and the corresponding evolution of dislocation microstructures. The simulated results align well with experimental observations, further validating the utility of the CDD approach in studying the mechanical response of materials subjected to cyclic loading.

7. SUMMARY AND FUTURE WORK

In this thesis, we discussed the theoretical framework of vector-based continuum dislocation dynamics (CDD) to predict the formation of dislocation microstructure patterns at small strains, along with the corresponding numerical simulation results.

First, we proposed a new computational framework that decouples the transport-reaction equations and enforces the divergence constraint on individual slip systems in Section 3. This framework, which incorporates the concept of virtual density, addresses the accumulation of spurious dislocations, and improves computational efficiency while accurately capturing dislocation transport and reactions.

Furthermore, we conducted a statistical analysis of stress fluctuation, which represents the difference between the stress on the dislocation and the coarse-grained stress in Section 4. This analysis revealed the importance of accounting for the local stress state in coarse-grained theories, especially for accurately modeling dislocation processes like cross-slip. We demonstrated that the stress fluctuation can be described by a Cauchy distribution, and we highlighted the need to consider the appropriate volume for coarse graining in order to obtain reliable statistics for the continuum coarse-grained models.

Additionally, we analyzed the statistical properties of screw segment length and observed that they follow an exponential distribution with a mean that varies linearly with strain. By incorporating these statistical insights into the CDD model, we were able to accurately model the cross-slip process, as evidenced by comparable results to discrete dislocation dynamics (DDD) simulations in Section 5.

Through numerical simulations based on the new CDD frameworks, we investigated the formation of dislocation microstructure patterns under both monotonic and cyclic loading conditions at small strains in Sections 3, 5 and 6. Our results demonstrated the formation of dislocation-rich regions along specific crystallographic directions and planes, highlighting the influence of Taylor hardening mechanisms and dislocation reactions on microstructure evolution. Moreover, the CDD simulations successfully predicted the formation of cell like structures during relaxation experiments and vein-like structures in cyclic loading conditions that are typically observed in experiments.

In terms of future work, there are several areas for improvement. Incorporating dislocation-dislocation correlations and explicitly modeling the zipping and unzipping of sessile junctions can enhance the predictive capability of CDD. Additionally, further research is needed to predict junction formation and destruction rates in CDD, similar to cross-slip, by utilizing coarse-grained densities informed by DDD simulations. Moving forward, CDD can be employed to investigate dislocation microstructure pattern formation for different loading orientations, as well as other loading conditions such as ratchetting. Furthermore, the model can be extended to study other hardening mechanisms, including the interaction of dislocations with precipitates and the effects of factors like size, volume fraction, and transformation strains. Finally, CDD can provide valuable dislocation substructure information and plastic slip-related parameters to higher-level models such as crystal plasticity, facilitating the validation and refinement of assumptions used to characterize dislocation behavior.

PUBLICATIONS

The list of papers that were already published and soon to be published based on the work done during the whole of my PhD tenure is outlined below.

1. **V. Vivekanandan**, P. Lin, G. Winther, A. El-Azab, On the implementation of dislocation reactions in continuum dislocation dynamics modeling of mesoscale plasticity, Journal of the Mechanics and Physics of Solids. 149 (2021) 104327. https://doi.org/10.1016/j.jmps.2021.104327.

2. **V. Vivekanandan**, J. Anderson, Y. Pachaury, M. Mohamed, A. El-Azab, Statistics of internal stress fluctuations in dislocated crystals and relevance to density-based dislocation dynamics models, Modelling Simul. Mater. Sci. Eng. (2022). https://doi.org/10.1088/1361-651X/ac5dcf.

3. **V. Vivekanandan**, B. Anglin, A. El-Azab, A data driven approach for cross-slip modelling in continuum dislocation dynamics, International Journal of Plasticity. 164 (2023) 103597. https://doi.org/10.1016/j.ijplas.2023.103597.

4. J.P. Anderson, **V. Vivekanandan**, P. Lin, K. Starkey, Y. Pachaury, A. El-Azab, Situating the Vector Density Approach Among Contemporary Continuum Theories of Dislocation Dynamics, Journal of Engineering Materials and Technology. 144 (2022) 011014. https://doi.org/10.1115/1.4052066.

5. P. Lin, **V. Vivekanandan**, K. Starkey, B. Anglin, C. Geller, A. El-Azab, On the computational solution of vector-density based continuum dislocation dynamics models: A comparison of two plastic distortion and stress update algorithms, International Journal of Plasticity. 138 (2021) 102943. https://doi.org/10.1016/j.ijplas.2021.102943.

6. P. Lin, **V. Vivekanandan**, B. Anglin, C. Geller, A. El-Azab, Incorporating point defect generation due to jog formation into the vector density-based continuum dislocation dynamics approach, Journal of the Mechanics and Physics of Solids. 156 (2021) 104609. https://doi.org/10.1016/j.jmps.2021.104609.

7. Dislocation microstructure evolution during cyclic deformation: A continuum dislocation dynamics study (To be submitted).

8. A computational framework to upscale information from continuum dislocation dynamics models to crystal plasticity models (To be submitted).

9. Understanding dislocation interaction with impenetrable precipitates using continuum dislocation dynamics (To be submitted).

REFERENCES

Acharya, A., 2004. Constitutive analysis of finite deformation field dislocation mechanics. Journal of the Mechanics and Physics of Solids 52, 301–316. https://doi.org/10.1016/S0022-5096(03)00093-0

Acharya, A., Roy, A., 2006. Size effects and idealized dislocation microstructure at small scales: Predictions of a Phenomenological model of Mesoscopic Field Dislocation Mechanics: Part I. Journal of the Mechanics and Physics of Solids 54, 1687–1710. https://doi.org/10.1016/j.jmps.2006.01.009

Aifantis, E.C., 1986. On the dynamical origin of dislocation patterns. Materials Science and Engineering, Proceedings of the International Conference on Low Energy Dislocation Structures 81, 563–574. https://doi.org/10.1016/0025-5416(86)90293-4

Akhondzadeh, Sh., Sills, R.B., Bertin, N., Cai, W., 2020. Dislocation density-based plasticity model from massive discrete dislocation dynamics database. Journal of the Mechanics and Physics of Solids 145, 104152. https://doi.org/10.1016/j.jmps.2020.104152

Amodeo, R., Ghoniem, N.M., 1988. Dynamical computer simulation of the evolution of a one-dimensional dislocation pileup. International Journal of Engineering Science 26, 653–662. https://doi.org/10.1016/0020-7225(88)90085-7

Anderson, J.P., El-Azab, A., 2021. On the three-dimensional spatial correlations of curved dislocation systems. Materials Theory 5, 1. https://doi.org/10.1186/s41313-020-00026-w

Argaman, N., Levy, O., Makov, G., 2001. When do 2-D dislocations form cellular structures? Materials Science and Engineering: A, Dislocations 2000: An International Conference on the Fundamentals of Plastic Deformation 309–310, 386–392. https://doi.org/10.1016/S0921-5093(00)01732-9

Argon, A., 2007. Strengthening Mechanisms in Crystal Plasticity. OUP Oxford.

Arora, R., Acharya, A., 2020. Dislocation pattern formation in finite deformation crystal plasticity. International Journal of Solids and Structures 184, 114–135. https://doi.org/10.1016/j.ijsolstr.2019.02.013

Arsenlis, A., Cai, W., Tang, M., Rhee, M., Oppelstrup, T., Hommes, G., Pierce, T.G., Bulatov, V.V., 2007. Enabling strain hardening simulations with dislocation dynamics. Modelling Simul. Mater. Sci. Eng. 15, 553–595. https://doi.org/10.1088/0965-0393/15/6/001

Arsenlis, A, Cai, W., Tang, M., Rhee, M., Oppelstrup, T., Hommes, G., Pierce, T.G., Bulatov, V.V., 2007. Enabling strain hardening simulations with dislocation dynamics. Modelling and Simulation in Materials Science and Engineering 15, 553–595. https://doi.org/10.1088/0965-0393/15/6/001

Bakó, B., Groma, I., 1999. Stochastic O(N) algorithm for dislocation dynamics. Modelling Simul. Mater. Sci. Eng. 7, 181–188. https://doi.org/10.1088/0965-0393/7/2/004

Basinski, Z.S., Basinski, S.J., 1989. Temperature and rate dependence of saturation stress for low amplitude fatigue of Cu crystals between 4.2 and 350 K. Acta Metallurgica 37, 3255–3262. https://doi.org/10.1016/0001-6160(89)90198-3

Bertin, N., Upadhyay, M.V., Pradalier, C., Capolungo, L., 2015. A FFT-based formulation for efficient mechanical fields computation in isotropic and anisotropic periodic discrete dislocation dynamics. Modelling Simul. Mater. Sci. Eng. 23, 065009. https://doi.org/10.1088/0965-0393/23/6/065009

Bonneville, J., Escaig, B., 1979. Cross-slipping process and the stress-orientation dependence in pure copper. Acta Metallurgica 27, 1477–1486. https://doi.org/10.1016/0001-6160(79)90170-6

Bulatov, V., Cai, W., 2006. Computer Simulations of Dislocations. OUP Oxford.

Cai, W., Arsenlis, A., Weinberger, C.R., Bulatov, V.V., 2006. A non-singular continuum theory of dislocations. Journal of the Mechanics and Physics of Solids 54, 561–587. https://doi.org/10.1016/j.jmps.2005.09.005

Csikor, F.F., Groma, I., 2004. Probability distribution of internal stress in relaxed dislocation systems. Phys. Rev. B 70, 064106. https://doi.org/10.1103/PhysRevB.70.064106

Cui, Y., Liu, Z., Zhuang, Z., 2015. Quantitative investigations on dislocation based discrete-continuous model of crystal plasticity at submicron scale. International Journal of Plasticity 69, 54–72. https://doi.org/10.1016/j.ijplas.2015.02.002

Deng, J., El-Azab, A., 2010. Temporal statistics and coarse graining of dislocation ensembles. Philosophical Magazine 90, 3651–3678. https://doi.org/10.1080/14786435.2010.497472

Deng, J., El-Azab, A., 2009. Mathematical and computational modelling of correlations in dislocation dynamics. Modelling Simul. Mater. Sci. Eng. 17, 075010. https://doi.org/10.1088/0965-0393/17/7/075010

Deng, J., El-Azab, A., Larson, B.C., 2008. On the elastic boundary value problem of dislocations in bounded crystals. Philosophical Magazine 88, 3527–3548. https://doi.org/10.1080/14786430802558544

Déprés, C., Robertson *, C.F., Fivel, M.C., 2004. Low-strain fatigue in AISI 316L steel surface grains: a three-dimensional discrete dislocation dynamics modelling of the early cycles I. Dislocation microstructures and mechanical behaviour. Philosophical Magazine 84, 2257–2275. https://doi.org/10.1080/14786430410001690051

Déprés, C., Robertson, C.F., Fivel, M., Degallaix, S., 2005. A Three Dimensional Discrete Dislocation Dynamics Analysis of Cyclic Straining in 316L Stainless Steel. MSF 482, 163–166. https://doi.org/10.4028/www.scientific.net/MSF.482.163

Déprés, C., Robertson, C.F., Fivel, M.C., 2006. Low-strain fatigue in 316L steel surface grains: a three dimension discrete dislocation dynamics modelling of the early cycles. Part 2: Persistent slip markings and micro-crack nucleation. Philosophical Magazine 86, 79–97. https://doi.org/10.1080/14786430500341250

Devincre, B., Kubin, L., Hoc, T., 2007. Collinear superjogs and the low-stress response of fcc crystals. Scripta Materialia 57, 905–908. https://doi.org/10.1016/j.scriptamat.2007.07.026

Devincre, B., Kubin, L.P., Lemarchand, C., Madec, R., 2001. Mesoscopic simulations of plastic deformation. Materials Science and Engineering: A, Dislocations 2000: An International Conference on the Fundamentals of Plastic Deformation 309–310, 211–219. https://doi.org/10.1016/S0921-5093(00)01725-1

Devincre, B., Madec, R., Monnet, G., Queyreau, S., Gatti, R., Kubin, L., 2011. MODELING CRYSTAL PLASTICITY WITH DISLOCATION DYNAMICS SIMULATIONS: THE 'MICROMEGAS' CODE. Mechanics of Nano-objects 81–100.

El-Azab, A., 2006. Statistical mechanics of dislocation systems. Scripta Materialia, Viewpoint set no. 39: Statistical mechanics and coarse graining of dislocation behavior for continuum plasticity 54, 723–727. https://doi.org/10.1016/j.scriptamat.2005.11.031

El-Azab, A., 2000a. Statistical mechanics treatment of the evolution of dislocation distributions in single crystals. Physical Review B 61, 11956–11966. https://doi.org/10.1103/PhysRevB.61.11956

El-Azab, A., 2000b. The boundary value problem of dislocation dynamics. Modelling Simul. Mater. Sci. Eng. 8, 37–54. https://doi.org/10.1088/0965-0393/8/1/304

El-Azab, A., Po, G., 2020. Continuum Dislocation Dynamics: Classical Theory and Contemporary Models, in: Andreoni, W., Yip, S. (Eds.), Handbook of Materials Modeling. Springer International Publishing, Cham, pp. 1583–1607. https://doi.org/10.1007/978-3-319-44677-6_18

Fleck, N.A., Muller, G.M., Ashby, M.F., Hutchinson, J.W., 1994. Strain gradient plasticity: Theory and experiment. Acta Metallurgica et Materialia 42, 475–487. https://doi.org/10.1016/0956-7151(94)90502-9

Fleischer, R.L., 1959. Cross slip of extended dislocations. Acta Metallurgica 7, 134–135. https://doi.org/10.1016/0001-6160(59)90122-1

Frigo, M., 1999. A fast Fourier transform compiler, in: Proceedings of the ACM SIGPLAN 1999 Conference on Programming Language Design and Implementation, PLDI '99. Association for Computing Machinery, New York, NY, USA, pp. 169–180. https://doi.org/10.1145/301618.301661

Gavagnin, E., Owen, J.P., Yates, C.A., 2018. Pair correlation functions for identifying spatial correlation in discrete domains. Phys. Rev. E 97, 062104. https://doi.org/10.1103/PhysRevE.97.062104

Giessen, E.V. der, Needleman, A., 1995. Discrete dislocation plasticity: a simple planar model. Modelling Simul. Mater. Sci. Eng. 3, 689–735. https://doi.org/10.1088/0965-0393/3/5/008

Grilli, N., Janssens, K.G.F., Nellessen, J., Sandlöbes, S., Raabe, D., 2018. Multiple slip dislocation patterning in a dislocation-based crystal plasticity finite element method. International Journal of Plasticity 100, 104–121. https://doi.org/10.1016/j.ijplas.2017.09.015

Groma, I., 1997. Link between the microscopic and mesoscopic length-scale description of the collective behavior of dislocations. Phys. Rev. B 56, 5807–5813. https://doi.org/10.1103/PhysRevB.56.5807

Groma, I., Bakó, B., 1998. Probability distribution of internal stresses in parallel straight dislocation systems. Phys. Rev. B 58, 2969–2974. https://doi.org/10.1103/PhysRevB.58.2969

Hansen, N., Kuhlmann-Wilsdorf, D., 1986. Low energy dislocation structures due to unidirectional deformation at low temperatures. Materials Science and Engineering, Proceedings of the International Conference on Low Energy Dislocation Structures 81, 141–161. https://doi.org/10.1016/0025-5416(86)90258-2

Hochrainer, T., 2015. Multipole expansion of continuum dislocations dynamics in terms of alignment tensors. Philosophical Magazine 95, 1321–1367. https://doi.org/10.1080/14786435.2015.1026297

Hochrainer, T., Zaiser, M., Gumbsch, P., 2007. A three-dimensional continuum theory of dislocation systems: kinematics and mean-field formulation. Philosophical Magazine 87, 1261–1282. https://doi.org/10.1080/14786430600930218

Humphreys, F.J., Hatherly, M., 2012. Recrystallization and Related Annealing Phenomena. Elsevier.

Hussein, A.M., Rao, S.I., Uchic, M.D., Dimiduk, D.M., El-Awady, J.A., 2015. Microstructurally based cross-slip mechanisms and their effects on dislocation microstructure evolution in fcc crystals. Acta Materialia 85, 180–190. https://doi.org/10.1016/j.actamat.2014.10.067

Ispánovity, P.D., Groma, I., 2008. The probability distribution of internal stresses in externally loaded 2D dislocation systems. J. Stat. Mech. 2008, P12009. https://doi.org/10.1088/1742-5468/2008/12/P12009

Jin, N.Y., 1989. Formation of dislocation structures during cyclic deformation of F.C.C. crystals—I. Formation of PSBs in crystals oriented for single-slip. Acta Metallurgica 37, 2055–2066. https://doi.org/10.1016/0001-6160(89)90091-6

Kalaei, A., Xiang, Y., Ngan, A.H.W., 2022. An efficient and minimalist scheme for continuum dislocation dynamics. International Journal of Plasticity 103433. https://doi.org/10.1016/j.ijplas.2022.103433

Kang, K., Yin, J., Cai, W., 2014. Stress dependence of cross slip energy barrier for face-centered cubic nickel. Journal of the Mechanics and Physics of Solids, Sixtieth anniversary issue in honor of Professor Rodney Hill 62, 181–193. https://doi.org/10.1016/j.jmps.2013.09.023

Kosevich, A.M., 1965. DYNAMICAL THEORY OF DISLOCATIONS. Sov. Phys. Usp. 7, 837. https://doi.org/10.1070/PU1965v007n06ABEH003688

Kröner, E., 1959. Allgemeine Kontinuumstheorie der Versetzungen und Eigenspannungen. Arch. Rational Mech. Anal. 4, 273. https://doi.org/10.1007/BF00281393

Kubin, L., 2013. Dislocations, Mesoscale Simulations and Plastic Flow. OUP Oxford.

Kubin, L., Hoc, T., Devincre, B., 2009. Dynamic recovery and its orientation dependence in face-centered cubic crystals. Acta Materialia 57, 2567–2575. https://doi.org/10.1016/j.actamat.2009.02.013

Kubin, L.P., Canova, G., Condat, M., Devincre, B., Pontikis, V., Bréchet, Y., 1992. Dislocation Microstructures and Plastic Flow: A 3D Simulation. Solid State Phenomena 23–24, 455–472. https://doi.org/10.4028/www.scientific.net/SSP.23-24.455

Kuhlmann-Wilsdorf, D., 2002. Chapter 59 The LES theory of solid plasticity, in: Nabarro, F.R.N., Duesbery, M.S. (Eds.), Dislocations in Solids. Elsevier, pp. 211–342. https://doi.org/10.1016/S1572-4859(02)80010-9

Kuhlmann-Wilsdorf, D., Comins, N.R., 1983. Dislocation cell formation and work hardening in the unidirectional glide of f.c.c. metals I: Basic theoretical analysis of cell walls parallel to the primary glide plane in early stage II. Materials Science and Engineering 60, 7–24. https://doi.org/10.1016/0025-5416(83)90073-3

Kuykendall, W.P., Wang, Y., Cai, W., 2020. Stress effects on the energy barrier and mechanisms of cross-slip in FCC nickel. Journal of the Mechanics and Physics of Solids 144, 104105. https://doi.org/10.1016/j.jmps.2020.104105

Laurson, L., Miguel, M.-C., Alava, M.J., 2010. Dynamical Correlations near Dislocation Jamming. Phys. Rev. Lett. 105, 015501. https://doi.org/10.1103/PhysRevLett.105.015501

Leung, H.S., Ngan, A.H.W., 2016. Dislocation-density function dynamics – An all-dislocation, full-dynamics approach for modeling intensive dislocation structures. Journal of the Mechanics and Physics of Solids 91, 172–203. https://doi.org/10.1016/j.jmps.2016.03.008

Li, D., Zbib, H., Sun, X., Khaleel, M., 2014. Predicting plastic flow and irradiation hardening of iron single crystal with mechanism-based continuum dislocation dynamics. International Journal of Plasticity, In Honor of Hussein Zbib 52, 3–17. https://doi.org/10.1016/j.ijplas.2013.01.015

Li, P., Li, S.X., Wang, Z.G., Zhang, Z.F., 2011. Fundamental factors on formation mechanism of dislocation arrangements in cyclically deformed fcc single crystals. Progress in Materials Science 56, 328–377. https://doi.org/10.1016/j.pmatsci.2010.12.001

Li, Y., Chatterjee, S., Martinez, E., Ghoniem, N., Po, G., 2021. On the cross-slip of screw dislocations in zirconium. Acta Materialia 208, 116764. https://doi.org/10.1016/j.actamat.2021.116764

Lin, P., El-Azab, A., 2020. Implementation of annihilation and junction reactions in vector density-based continuum dislocation dynamics. Modelling Simul. Mater. Sci. Eng. 28, 045003. https://doi.org/10.1088/1361-651X/ab7d90

Lin, P., Vivekanandan, V., Starkey, K., Anglin, B., Geller, C., El-Azab, A., 2021. On the computational solution of vector-density based continuum dislocation dynamics models: A comparison of two plastic distortion and stress update algorithms. International Journal of Plasticity 138, 102943. https://doi.org/10.1016/j.ijplas.2021.102943

Madec, R., Devincre, B., Kubin, L.P., 2002. Simulation of dislocation patterns in multislip. Scripta Materialia 47, 689–695. https://doi.org/10.1016/S1359-6462(02)00185-9

Malka-Markovitz, A., Devincre, B., Mordehai, D., 2021. A molecular dynamics-informed probabilistic cross-slip model in discrete dislocation dynamics. Scripta Materialia 190, 7–11. https://doi.org/10.1016/j.scriptamat.2020.08.008

Malka-Markovitz, A., Mordehai, D., 2019. Cross-slip in face centred cubic metals: a general full stress-field dependent activation energy line-tension model. Philosophical Magazine 99, 1460–1480. https://doi.org/10.1080/14786435.2019.1584410

Malka-Markovitz, A., Mordehai, D., 2018. Cross-slip in face-centered cubic metals: a general Escaig stress-dependent activation energy line tension model. Philosophical Magazine 98, 347–370. https://doi.org/10.1080/14786435.2017.1406194

Miura, T., Maini, P.K., 2004. Periodic pattern formation in reaction—diffusion systems: An introduction for numerical simulation. Anato Sci Int 79, 112. https://doi.org/10.1111/j.1447-073x.2004.00079.x

Monavari, M., Zaiser, M., 2018. Annihilation and sources in continuum dislocation dynamics. Materials Theory 2. https://doi.org/10.1186/s41313-018-0010-z

Motz, C., Weygand, D., Senger, J., Gumbsch, P., 2009. Initial dislocation structures in 3-D discrete dislocation dynamics and their influence on microscale plasticity. Acta Materialia 57, 1744–1754. https://doi.org/10.1016/j.actamat.2008.12.020

Mughrabi, H., 1983. Dislocation wall and cell structures and long-range internal stresses in deformed metal crystals. Acta Metallurgica 31, 1367–1379. https://doi.org/10.1016/0001-6160(83)90007-X

Mura, T., 1963. Continuous distribution of moving dislocations. The Philosophical Magazine: A Journal of Theoretical Experimental and Applied Physics 8, 843–857. https://doi.org/10.1080/14786436308213841

Nye, J.F., 1953. Some geometrical relations in dislocated crystals. Acta Metallurgica 1, 153–162. https://doi.org/10.1016/0001-6160(53)90054-6

Orowan, E., 1934. Zur Kristallplastizität. I. Zeitschrift für Physik 89, 605–613.

Po, G., Mohamed, M.S., Crosby, T., Erel, C., El-Azab, A., Ghoniem, N., 2014. Recent Progress in Discrete Dislocation Dynamics and Its Applications to Micro Plasticity. JOM 66, 2108–2120. https://doi.org/10.1007/s11837-014-1153-2

Polanyi, M., 1934. Über eine Art Gitterstörung, die einen Kristall plastisch machen könnte. Z. Physik 89, 660–664. https://doi.org/10.1007/BF01341481

Pontes, J., Walgraef, D., Aifantis, E.C., 2006. On dislocation patterning: Multiple slip effects in the rate equation approach. International Journal of Plasticity, Special issue in honour of Dr. Kirk Valanis 22, 1486–1505. https://doi.org/10.1016/j.ijplas.2005.07.011

Rao, S.I., Dimiduk, D.M., El-Awady, J.A., Parthasarathy, T.A., Uchic, M.D., Woodward, C., 2010. Activated states for cross-slip at screw dislocation intersections in face-centered cubic nickel and copper via atomistic simulation. Acta Materialia 58, 5547–5557. https://doi.org/10.1016/j.actamat.2010.06.005

Rao, S.I., Dimiduk, D.M., Parthasarathy, T.A., El-Awady, J., Woodward, C., Uchic, M.D., 2011. Calculations of intersection cross-slip activation energies in fcc metals using nudged elastic band method. Acta Materialia 59, 7135–7144. https://doi.org/10.1016/j.actamat.2011.08.029

Rao, S.I., Dimiduk, D.M., Parthasarathy, T.A., Uchic, M.D., Woodward, C., 2013. Atomistic simulations of surface cross-slip nucleation in face-centered cubic nickel and copper. Acta Materialia 61, 2500–2508. https://doi.org/10.1016/j.actamat.2013.01.026

Rhee, M., Zbib, H.M., Hirth, J.P., Huang, H., Rubia, T. de la, 1998. Models for long-/short-range interactions and cross slip in 3D dislocation simulation of BCC single crystals. Modelling Simul. Mater. Sci. Eng. 6, 467. https://doi.org/10.1088/0965-0393/6/4/012

Roters, F., Diehl, M., Shanthraj, P., Eisenlohr, P., Reuber, C., Wong, S.L., Maiti, T., Ebrahimi, A., Hochrainer, T., Fabritius, H.-O., Nikolov, S., Friák, M., Fujita, N., Grilli, N., Janssens, K.G.F., Jia, N., Kok, P.J.J., Ma, D., Meier, F., Werner, E., Stricker, M., Weygand, D., Raabe, D., 2019. DAMASK – The Düsseldorf Advanced Material Simulation Kit for modeling multi-physics crystal plasticity, thermal, and damage phenomena from the single crystal up to the component scale. Computational Materials Science 158, 420–478. https://doi.org/10.1016/j.commatsci.2018.04.030

Roy, A., Acharya, A., 2006. Size effects and idealized dislocation microstructure at small scales: Predictions of a Phenomenological model of Mesoscopic Field Dislocation Mechanics: Part II. Journal of the Mechanics and Physics of Solids 54, 1711–1743. https://doi.org/10.1016/j.jmps.2006.01.012

Sandfeld, S., Hochrainer, T., Gumbsch, P., Zaiser, M., 2010. Numerical implementation of a 3D continuum theory of dislocation dynamics and application to micro-bending. Philosophical Magazine 90, 3697–3728. https://doi.org/10.1080/14786430903236073

Sandfeld, S., Thawinan, E., Wieners, C., 2015. A link between microstructure evolution and macroscopic response in elasto-plasticity: Formulation and numerical approximation of the higher-dimensional continuum dislocation dynamics theory. International Journal of Plasticity 72, 1–20. https://doi.org/10.1016/j.ijplas.2015.05.001

Sandfeld, S., Zaiser, M., 2015. Pattern formation in a minimal model of continuum dislocation plasticity. Modelling Simul. Mater. Sci. Eng. 23, 065005. https://doi.org/10.1088/0965-0393/23/6/065005

Schulz, K., Wagner, L., Wieners, C., 2019. A mesoscale continuum approach of dislocation dynamics and the approximation by a Runge-Kutta discontinuous Galerkin method. International Journal of Plasticity 120, 248–261. https://doi.org/10.1016/j.ijplas.2019.05.003

Sills, R.B., Bertin, N., Aghaei, A., Cai, W., 2018. Dislocation Networks and the Microstructural Origin of Strain Hardening. Phys. Rev. Lett. 121, 085501. https://doi.org/10.1103/PhysRevLett.121.085501

Starkey, K., El-Azab, A., 2022. Total Lagrange implementation of a finite-deformation continuum dislocation dynamics model of mesoscale plasticity. International Journal of Plasticity 155, 103332. https://doi.org/10.1016/j.ijplas.2022.103332

Stricker, M., Sudmanns, M., Schulz, K., Hochrainer, T., Weygand, D., 2018. Dislocation multiplication in stage II deformation of fcc multi-slip single crystals. Journal of the Mechanics and Physics of Solids 119, 319–333. https://doi.org/10.1016/j.jmps.2018.07.003

Sudmanns, M., Stricker, M., Weygand, D., Hochrainer, T., Schulz, K., 2019. Dislocation multiplication by cross-slip and glissile reaction in a dislocation based continuum formulation of crystal plasticity. Journal of the Mechanics and Physics of Solids 132, 103695. https://doi.org/10.1016/j.jmps.2019.103695

Taylor, G.I., 1934. The Mechanism of Plastic Deformation of Crystals. Part I. Theoretical. Proceedings of the Royal Society A: Mathematical, Physical and Engineering Sciences 145, 362–387. https://doi.org/10.1098/rspa.1934.0106

Ungar, T., Mughrabi, H., Rönnpagel, D., Wilkens, M., 1984. X-ray line-broadening study of the dislocation cell structure in deformed [001]-orientated copper single crystals. Acta Metallurgica 32, 333–342. https://doi.org/10.1016/0001-6160(84)90106-8

Vivekanandan, V., Anderson, J., Pachaury, Y., Mohamed, M., El-Azab, A., 2022. Statistics of internal stress fluctuations in dislocated crystals and relevance to density-based dislocation dynamics models. Modelling Simul. Mater. Sci. Eng. https://doi.org/10.1088/1361-651X/ac5dcf

Vivekanandan, V., Lin, P., Winther, G., El-Azab, A., 2021. On the implementation of dislocation reactions in continuum dislocation dynamics modeling of mesoscale plasticity. Journal of the Mechanics and Physics of Solids 149, 104327. https://doi.org/10.1016/j.jmps.2021.104327

Walgraef, D., Aifantis, E.C., 1985. Dislocation patterning in fatigued metals as a result of dynamical instabilities. Journal of Applied Physics 58, 688–691. https://doi.org/10.1063/1.336183

Wang, Z.Q., Beyerlein, I.J., LeSar, R., 2007. The importance of cross-slip in high-rate deformation. Modelling Simul. Mater. Sci. Eng. 15, 675. https://doi.org/10.1088/0965-0393/15/6/006

Weygand, D., Friedman, L.H., Giessen, E.V. der, Needleman, A., 2002. Aspects of boundary-value problem solutions with three-dimensional dislocation dynamics. Modelling Simul. Mater. Sci. Eng. 10, 437–468. https://doi.org/10.1088/0965-0393/10/4/306

Xia, S., Belak, J., El-Azab, A., 2016. The discrete-continuum connection in dislocation dynamics: I. Time coarse graining of cross slip. Modelling Simul. Mater. Sci. Eng. 24, 075007. https://doi.org/10.1088/0965-0393/24/7/075007

Xia, S., El-Azab, A., 2015. Computational modelling of mesoscale dislocation patterning and plastic deformation of single crystals. Modelling Simul. Mater. Sci. Eng. 23, 055009. https://doi.org/10.1088/0965-0393/23/5/055009

Yefimov, S., Groma, I., van der Giessen, E., 2004. A comparison of a statistical-mechanics based plasticity model with discrete dislocation plasticity calculations. Journal of the Mechanics and Physics of Solids 52, 279–300. https://doi.org/10.1016/S0022-5096(03)00094-2

Zacharopoulos, N., Srolovitz, D.J., LeSar, R., 2003. Discrete dislocation simulations of the development of a continuum plastic zone ahead of a stationary Mode III crack. Journal of the Mechanics and Physics of Solids 51, 695–713. https://doi.org/10.1016/S0022-5096(02)00099-6

Zaiser, M., 2015. Local density approximation for the energy functional of three-dimensional dislocation systems. Phys. Rev. B 92, 174120. https://doi.org/10.1103/PhysRevB.92.174120

Zaiser, M., Miguel, M.-C., Groma, I., 2001. Statistical dynamics of dislocation systems: The influence of dislocation-dislocation correlations. Physical Review B 64. https://doi.org/10.1103/PhysRevB.64.224102

Zhou, C., LeSar, R., 2012. Dislocation dynamics simulations of plasticity in polycrystalline thin films. International Journal of Plasticity 30–31, 185–201. https://doi.org/10.1016/j.ijplas.2011.10.001

Zhu, Y., Xiang, Y., Schulz, K., 2016. The role of dislocation pile-up in flow stress determination and strain hardening. Scripta Materialia 116, 53–56. https://doi.org/10.1016/j.scriptamat.2016.01.025

Zienkiewicz, O.C., Taylor, R.L., Zhu, J.Z., 2005. The Finite Element Method: Its Basis and Fundamentals. Elsevier.